# Lunar Orbiter I
# Preliminary Results

## LUNAR TERRAIN ASSESSMENT AND
## SELENODESY, MICROMETEOROID, AND
## RADIATION MEASUREMENTS

NATIONAL AERONAUTICS AND SPACE ADMINISTRATION
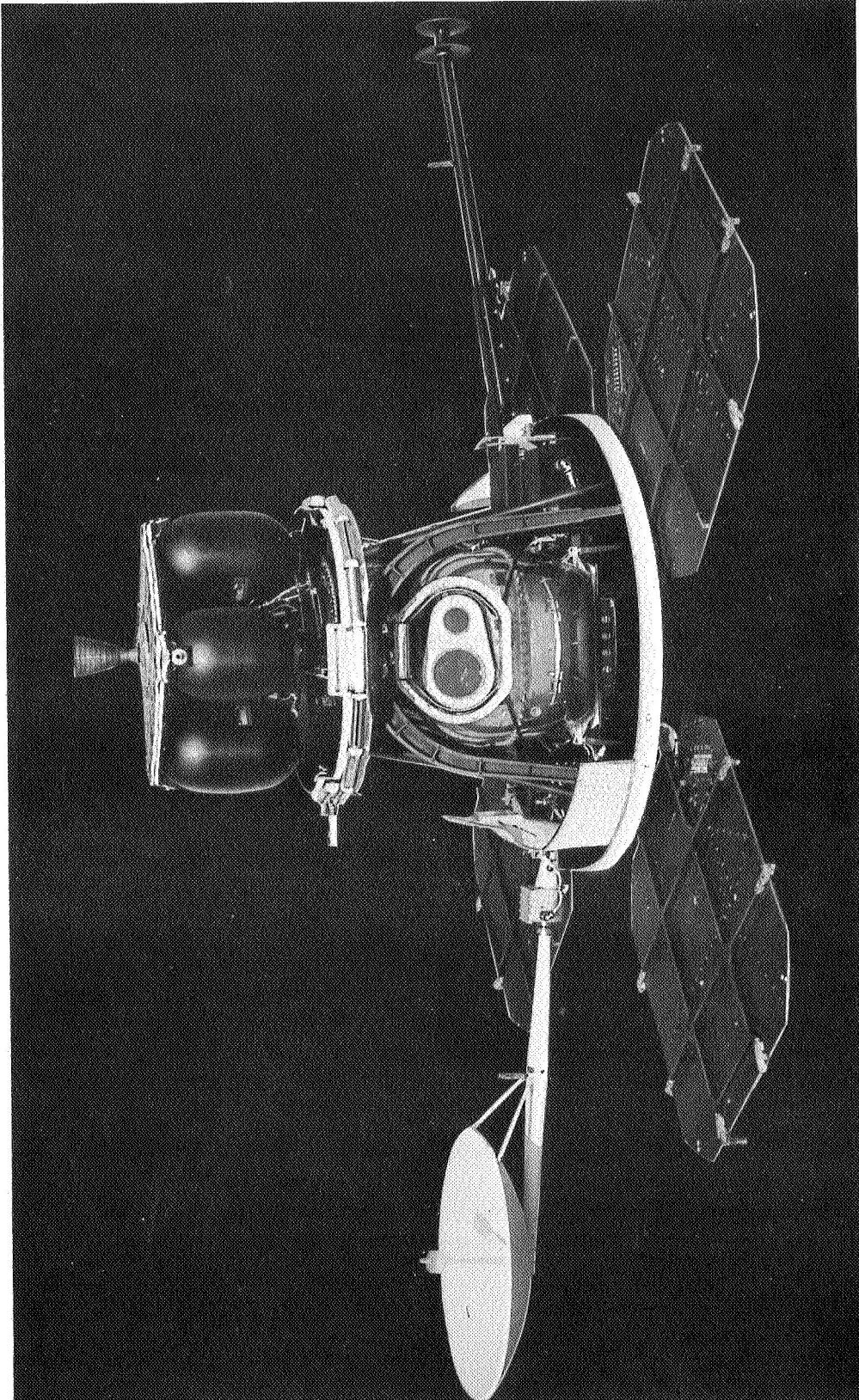
L-69-1204



LUNAR ORBITER

# Lunar Orbiter I Preliminary Results

## LUNAR TERRAIN ASSESSMENT AND SELENODESY, MICROMETEOROID, AND RADIATION MEASUREMENTS

Compiled by

J. KENRICK HUGHES and GERALD W. BREWER
*NASA Langley Research Center*
*Langley Station, Hampton, Virginia*

# PREFACE

In March 1964, the National Aeronautics and Space Administration initiated the Lunar Orbiter Program, a program which involved the design, development, and utilization of a complex spacecraft to acquire detailed photographs of the lunar surface from low-altitude orbits about the moon. Five missions with launch intervals of 3 months were planned, the overall objectives being to obtain, primarily, information on the nature of the lunar surface and, secondarily, information on the gravitational, micrometeoroid, and radiation fields of the moon.

The first of these spacecraft, Lunar Orbiter I, was launched August 10, 1966, only 28 months after contract go-ahead. It achieved the distinction of being the first United States spacecraft to orbit the moon, to obtain detailed photographic coverage of extended areas of the near and far sides of the moon, and to photograph the earth from the vicinity of the moon.

The Lunar Orbiter I photographic mission was designed to examine selected areas near the equator on the moon's visible face. These areas, on the basis of what could be seen by telescopic observation from earth, appeared to be suitable as manned landing sites in the Apollo Program.

These sites, as well as others of scientific interest, were photographed during August 1966. The mission was not an unqualified success. A malfunction in the high-resolution camera resulted in smeared and unusable high-resolution photographs. However, of the 413 frames exposed and transmitted to earth, 220 were perfectly usable.

It is the purpose of this report to present the preliminary scientific information obtained by Lunar Orbiter I. This covers an assessment of lunar terrain, and the results of the secondary experiments in selenodesy, micrometeoroids, and radiation. For further information concerning Lunar Orbiter photographs, the reader should contact the National Space Science Data Center, Goddard Space Flight Center, Greenbelt, Maryland 20771.

CONTENTS

# SUMMARY

The primary objective of the Lunar Orbiter Program is to secure, by high-resolution photography, topographic and geologic data of the lunar surface. Such information, which is necessary for the selection and confirmation of landing sites for Project Apollo, will also extend man's scientific knowledge of the moon. Secondary objectives of the program are an improvement in the definition of the lunar gravitational field and the determination of meteoroid and radiation flux in the lunar environment.

It is the purpose of this report to present the preliminary results of the flight of Lunar Orbiter I, the first of five flight spacecraft, which was launched from Cape Kennedy, Florida, August 10, 1966, and which subsequently became the first U.S. satellite to orbit the moon. The spacecraft remained in orbit until October 29, 1966, at which time, to avoid interference with Lunar Orbiter II, it was deliberately destroyed by slowing its velocity and allowing it to crash into the moon.

Due to a problem with the operation of the camera shutter mechanism, the high-resolution exposures (1-meter resolution at 46-km altitude) showed a varying degree of smear and thus did not meet mission requirements. The medium-resolution exposures (8-meter resolution at 46-km altitude) showed sufficient new terrain features of engineering and scientific interest to warrant inclusion in this report.

Analysis of the reassembled photographs shows a lunar crust that is fractured and faulted. Mass-wasting is seen where large boulders and debris have tumbled into craters. The moon appears to have been highly dynamic and affected by volcanic activity. However, despite the overall roughness characteristics of the lunar surface, some photographs show local regions of relative smoothness, particularly in the darker mare. Photographs of the far side of the moon show a surface that, in general, is much rougher than the near side as a result of a higher terra-to-mare ratio on the far side.

The results of the secondary experiments were also valuable. Having registered no impacts throughout the mission, the meteoroid sensors helped to refine the estimates of the meteor activity in the vicinity of the moon by several orders of magnitude and thus to indicate that it was no worse than that found in the earth environment. The radiation dose rate (0.5 to 1 mrad/hr) during transit to the moon corresponded to that produced by galactic cosmic rays; but during the solar flares of August 28 and September 2, 1966, dose rates as high as 70 mrad/hr and 7 rad/hr, respectively, were experienced. The initial objective of the selenodesy experiment is to determine the coefficients in the expansion of the lunar gravitational field equation in spherical harmonics and to establish the number of coefficients required in the solution. Much has been learned in this respect. Although insufficient tracking data have been received and analyzed for long-term prediction of the

behavior of a satellite in orbit about the moon, short-term prediction (the duration of the photographic mission) can be made with a high degree of confidence.

## INTRODUCTION

A major goal of several unmanned space programs of the National Aeronautics and Space Administration has been to obtain detailed information of the lunar surface as well as other lunar environmental information to support the planning and operations of future Apollo manned lunar landings. This report presents the preliminary results of photography of the lunar terrain from an orbiting spacecraft (Lunar Orbiter I) and of some experiments conducted during the period of photography as well as an additional 2 months of flight. At the end of this period the spacecraft was deliberately destroyed by lunar impact.

Prior to the time of lunar probes, landers, and orbiters, the study of the lunar terrain was made from many telescopic observations from earth. The best photographic resolution that has been achieved is of the order of 250 meters. Two NASA flight programs have contributed to the overall knowledge of the moon and to the needs of the Apollo manned lunar-landing program. Each Ranger spacecraft obtained photographs of local regions of the moon which were progressively more detailed as the spacecraft closed upon its impact point. Its final photograph of several hundred square feet of area resolved local terrain features to less than a meter in dimension. The Surveyor I soft-landing spacecraft successfully photographed terrain details in June 1966 to a few centimeters locally near the landing point. On its flight in August 1966, the Lunar Orbiter, designed for photography of large areas of the moon with two cameras having 1- and 8-meter resolution capability, achieved extensive coverage with the wide-angle camera (8-meter resolution). In fact, the wide-angle camera photographed about 41 500 $km^2$ of selected areas for Apollo landing-site study, 360 000 $km^2$ of other areas on the front side of the moon, and 5 200 000 $km^2$ of the far side of the moon from altitudes of about 1500 km (250-meter resolution). In addition, Lunar Orbiter I obtained information of scientific interest regarding the lunar environment and physical properties of the moon.

The Lunar Orbiter Project is managed by the Langley Research Center under the overall direction of the Office of Space Sciences and Application. The Lunar Orbiter mission includes a plan for five flights of a Lunar Orbiter space vehicle which consists of the Atlas-Agena launch vehicle and the spacecraft. The Lewis Research Center has systems-management responsibility for the launch-vehicle system and integration of the spacecraft with the launch vehicle as well as flight-operation functions up to Agena-spacecraft separation. The Jet Propulsion Laboratory has the systems-management responsibility for the DSIF (Deep Space Instrumentation Facility) and SFOF (Space Flight Operations Facility) operations in support of space flight. Responsibility for design and production of the spacecraft and mission support during flight operations rests with the

2

prime contractor, The Boeing Company. Major subcontractors are Eastman Kodak Company for the photographic subsystem and Radio Corporation of America for electrical power and communications equipment.

This report includes a preliminary assessment of the lunar terrain in the selected potential Apollo sites photographed as well as the preliminary results of the meteoroid, radiation, lunar radius, and selenodesy experiments. The material for the report was collected from the scientists and specialists of the Langley Research Center, U.S. Geological Survey, Aeronautical Chart and Information Service, and the Army Map Service. The contributors are acknowledged in the appropriate sections.

# MISSION OBJECTIVES

## PRIMARY OBJECTIVES

(1) To place the three-axis stabilized Lunar Orbiter spacecraft into lunar orbit.

(2) To obtain, by high-resolution photography, detailed lunar topographic and geological information about various terrain types to assess their suitability for use as landing sites by Apollo and Surveyor spacecraft and to improve man's knowledge of the moon.

## SECONDARY OBJECTIVES

(1) To photograph the Surveyor I landing site to permit the extrapolation of the Surveyor I data to other photographed areas.

(2) To provide precision trajectory information for use in improving the definition of the lunar gravitational field.

(3) To provide measurements of micrometeoroid and radiation flux in the lunar environment, primarily for spacecraft performance analysis.

# MISSION DESIGN

The following terrain-sampling ground rules were established:

(1) To obtain several samples of each of the significant terrain types.

(2) To insure that similar terrain types be reasonably distributed because of Apollo launch-window considerations.

(3) To concentrate on the most promising areas within the Apollo zone of ±45° longitude and ±5° latitude.

(4) To examine the Surveyor I site.

(5) To examine the promising future Surveyor sites.

The map in figure 1 was drawn as a guide for first-order site selection. This figure shows the approximate distribution of promising Surveyor sites, the significant mare and highland areas within the Apollo zone, and the Surveyor I site.
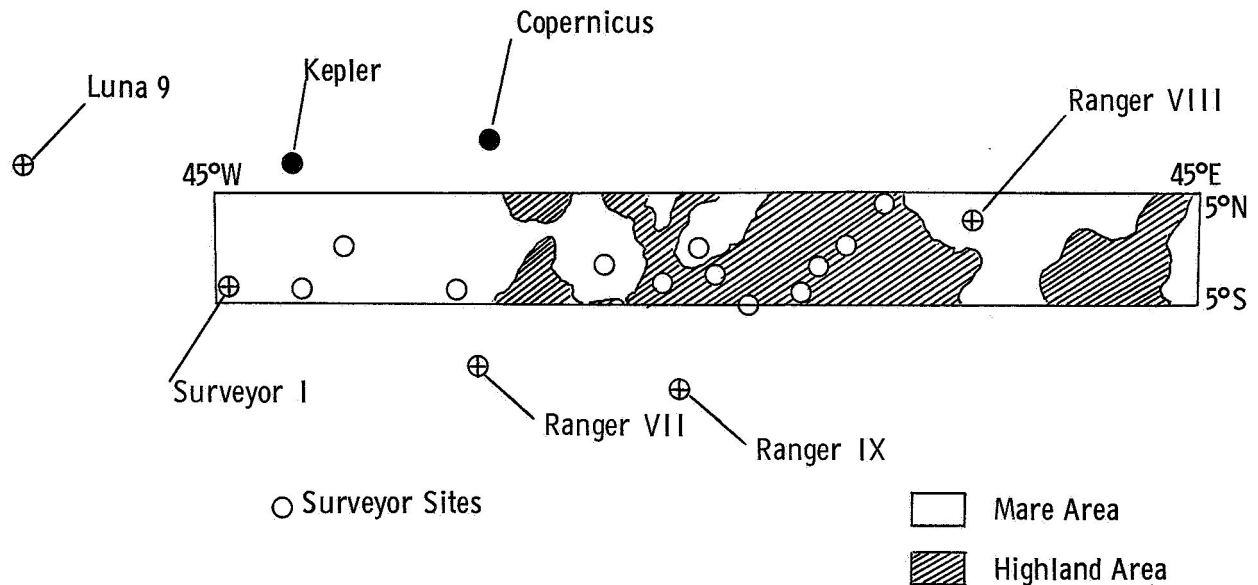


Figure 1.- Approximate distribution of Surveyor sites and significant mare and highland areas in Apollo zone.

## DESIGN CRITERIA

Apart from the inherent engineering difficulty of placing a complex spacecraft in orbit around the moon for the purpose of photographing selected sites, the mission is complicated by having to operate within the following constraints.

### PHOTOGRAPHIC-SYSTEM CONSTRAINTS

Film development in the photographic system is accomplished by the bimat process. In this process the exposed film is laminated to bimat film which contains the developer-fixer. The method has certain limitations which make it necessary to keep the film moving through the system. If the film remains in one position too long, it can assume the curvature of the looper rollers, the film and bimat can stick together, or the moist bimat can dry out. These limitations are referred to as "film set," "bimat stick," and "bimat dryout," respectively.

4

# OTHER MISSION CONSTRAINTS

Although the objective was to photograph nine selected equatorial sites, obtaining maximum coverage with only one pass per site (except for the Surveyor site where two passes were to be made), an additional requirement was to be able to cover any point in the Apollo zone. This objective fixed the orbit inclination to approximately $12^O$. Another limitation was that lighting conditions and altitude be adequate for the detection of cones with a base diameter of 2 meters and a height of 1/2 meter, and the detection of areas 7 meters square and with slopes not greater than $7^O$.

## ORBIT DESIGN

The earth-moon transit time for Lunar Orbiter is approximately 90 hours. Upon reaching the moon, a first deboost maneuver places the spacecraft into an elliptical orbit whose perilune altitude is about 200 km. The spacecraft remains in this orbit for several days during which time the orbit is more closely defined, after which a second deboost reduces the perilune to 46 km nominal. It is from this orbit that the primary photographic
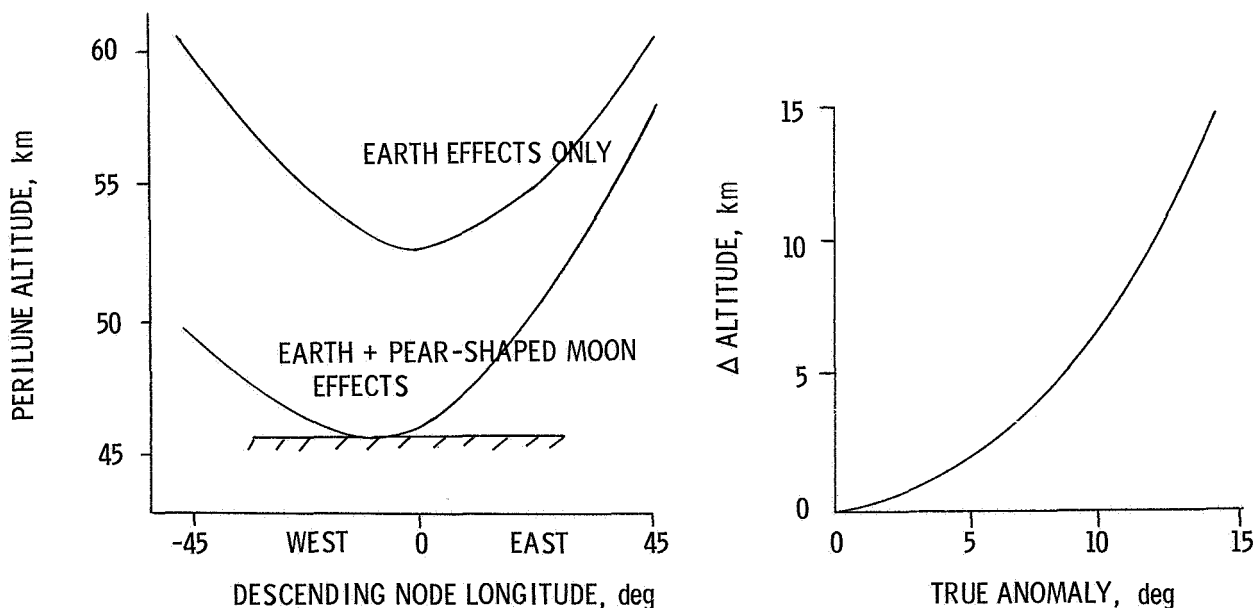


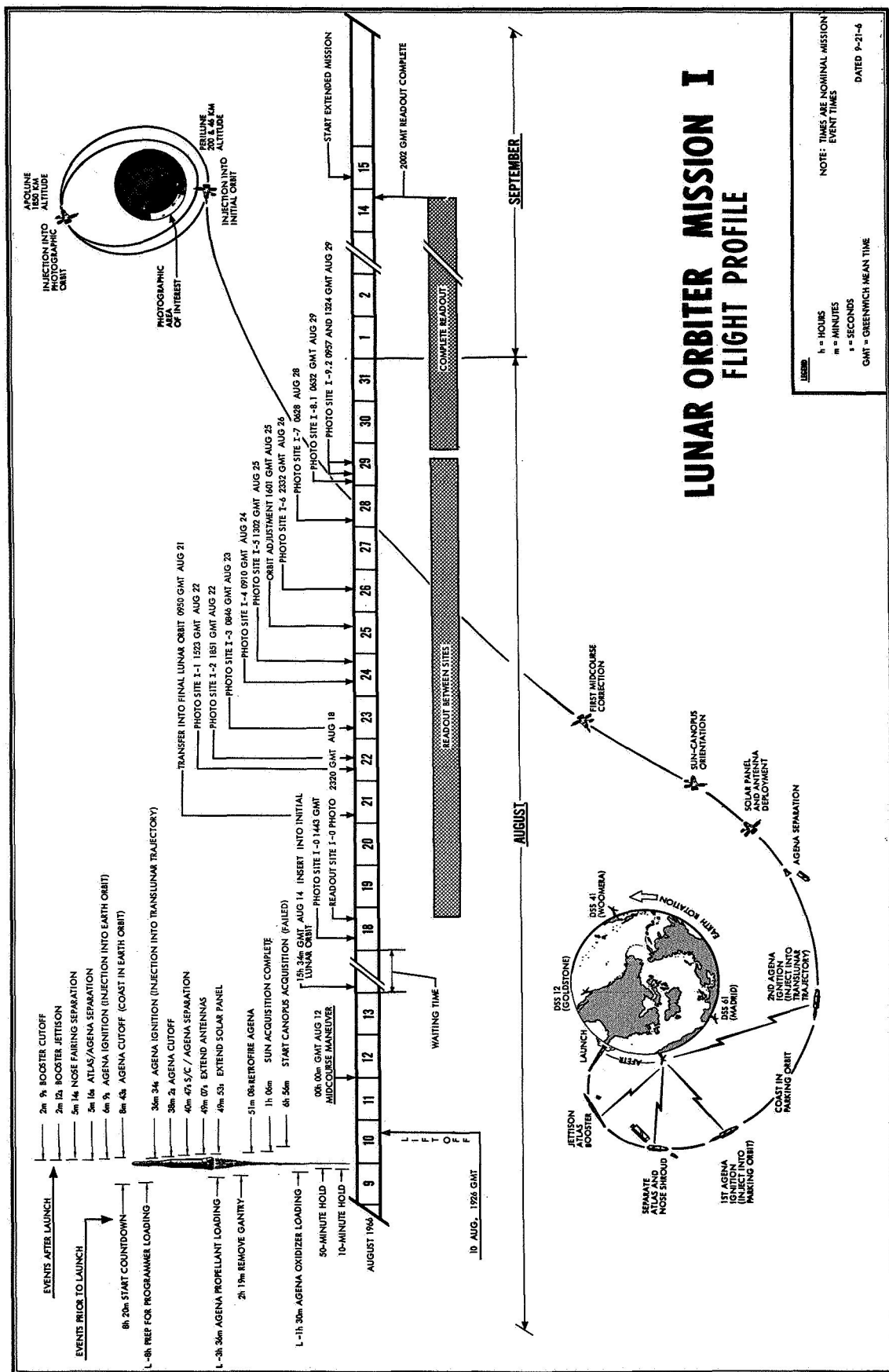Figure 2.- Photographic altitude constraints.

Figure 3.- Flight profile and mission sequence of events.

mission is performed. Some of the significant orbital parameters and the reasons for their selection are as follows:

1. Posigrade injection to provide visibility of deboost from earth

2. Photography close to the descending node to secure proper lighting on the selected sites

3. An inclination of $12^O$ to provide picture overlap on successive orbits

4. An orbit period of $3\frac{1}{2}$ hours to satisfy power-system constraints

5. An orbit perilune altitude of 46 to 60 km to avoid impacting the lunar surface and to satisfy photographic resolution requirements

The fact that the perilune altitude varies between 46 and 60 km is of considerable interest. This variation, which is caused by earth effects and lunar gravitational anomalies, linearly affects the photographic resolution obtainable. The left-hand plot in figure 2 shows the perilune-altitude variation due to earth and to earth-plus-moon effects. In addition, photographic resolution is degraded when photographing sites which are located off perilune as a direct result of an increase in photographic altitude. This is illustrated in the right-hand plot in figure 2, where the altitude change is plotted as a function of true anomaly (angle off perilune).

The launch profile and mission sequence of events are shown in figure 3.

## SITE SELECTION

In the early planning stages, 10 sites were chosen within the Apollo zone. However, prior to Lunar Orbiter I, the Surveyor I mission was successfully performed. A decision to photograph the Surveyor I site resulted in some site changes. The original sites A-8, A-9, and A-10 were deleted, and sites A-8.1 and A-9.1 were substituted. Site A-9.1 is the Surveyor I site, and site A-8.1 is a relocation of A-8 to prevent interference with photography of the Surveyor I site. The approved site locations for Lunar Orbiter Mission I are indicated in figure 4 and are identified in the following list:

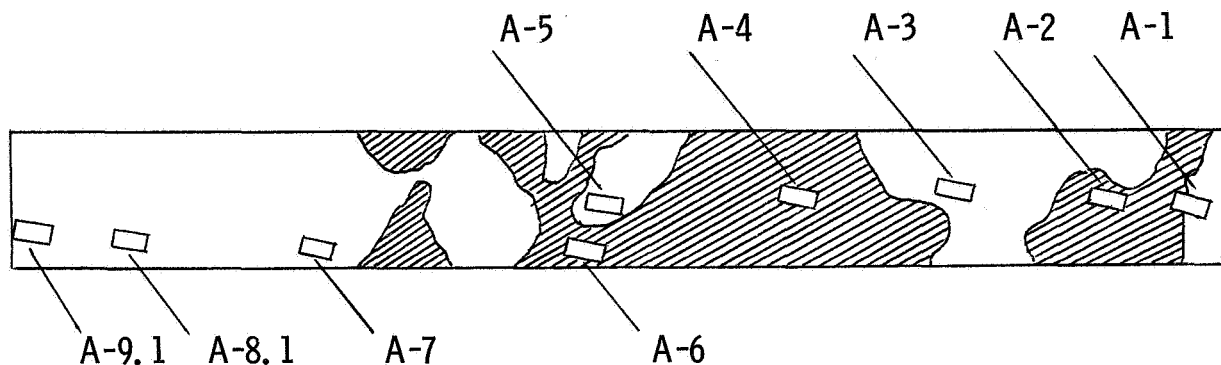| Site | Latitude | Longitude |
|------|----------|-----------|
| A-1 | $0^O50'$ S | $42^O20'$ E |
| A-2 | $0^O10'$ S | $36^O00'$ E |
| A-3 | $0^O20'$ N | $24^O50'$ E |
| A-4 . | $0^O00'$ | $12^O50'$ E |
| A-5 | $0^O25'$ S | $1^O\ 20'$ W |
| A-6 | $4^O00'$ S | $2^O\ 50'$ W |
| A-7 | $3^O45'$ S | $22^O45'$ W |
| A-8.1 | $3^O00'$ S | $36^O30'$ W |
| A-9.1 | $2^O21'$ S | $43^O22'$ W |

Figure 4.- Sites selected for Lunar Orbiter I.

## LUNAR ORBITER SPACECRAFT

The Lunar Orbiter spacecraft is launched and inserted into translunar flight by a two-stage launch vehicle consisting of the Atlas SLV-3/Agena D. Two isometric views of the spacecraft with components identified are given in figure 5. The spacecraft weighs 386 kg, is 1.67 meters high, and 1.52 meters in diameter with antennas and solar panels folded. With antennas and solar panels deployed, the span is increased to 5.64 meters along the antenna booms and 3.7 meters across the solar panels. The spacecraft incorporates seven major subsystems, but only the photographic subsystem is described in this report. Apparatus used in the meteoroid and radiation measurements is covered in the sections describing these experiments.

The major elements of the photographic subsystem (fig. 6) are a dual-lens camera, a film processor, and a readout system. From the nominal altitude of 46 km a lens with a focal length of 610 mm allows high-resolution exposures of an area on the lunar surface of 16.6 by 4.2 km, whereas an 80-mm wide-angle lens provides medium-resolution coverage of 37.4 by 31.6 km. The lenses are oriented so that the high-resolution (1 meter) photograph records the same area as found in the center of the companion medium-resolution (8 meter) photograph. The photographs, taken simultaneously, are interlaced on a single strip of Kodak high definition film SO-243, 70 mm wide and 80 meters long, as shown in figure 7. The photographic modes are illustrated in figure 8. The SO-243 film was selected because it is relatively insensitive to radiation, and although its aerial exposure index of 1.6 is slow compared to more common emulsions, it has an extremely fine grain and thus an exceptionally high resolving power of 250 lines/mm. Prior to use, the edges of the film are preexposed with framelet numbers, 9-level gray scale, and resolving power charts.

Both lenses open simultaneously at a fixed aperture of f/5.6. A between-the-lens shutter is used with the 80-mm lens, a double-curtain focal-plane shutter with the

8

VELOCITY
CONTROL ENGINE
ATTITUDE
CONTROL
THRUSTERS
FUEL
TANK
HIGH-GAIN
ANTENNA
CAMERA THERMAL DOOR
SOLAR
PANEL
CAMERA LENSES
EQUIPMENT MOUNTING DECK
PHOTOGRAPHIC
SUBSYSTEM
RADIATION
DETECTOR

UPPER STRUCTURAL
MODULE
HEAT SHIELD
COARSE
SUN SENSOR
OXIDIZER
TANK
MICROMETEOROID
DETECTOR
FLIGHT
PROGRAMMER
LOW-GAIN
ANTENNA
CANOPUS
STAR
TRACKER
INERTIAL
REFERENCE
UNIT

VELOCITY
CONTROL ENGINE
HEAT SHIELD
COARSE SUN
SENSOR
ATTITUDE CONTROL THRUSTERS
FUEL
TANK
OXIDIZER TANK
LOW-GAIN
ANTENNA
MICROMETEOROID
DETECTOR
FLIGHT
PROGRAMMER
SOLAR PANEL
BATTERY
ANTENNA
DRIVE
CHARGE
CONTROLLER
BATTERY
TWTA
COMMAND
DECODER
TRANSPONDER
MULTIPLEXER
ENCODER
RADIATION
DETECTOR
HIGH-GAIN
ANTENNA

NOTE: SHOWN WITH THERMAL BARRIER REMOVED

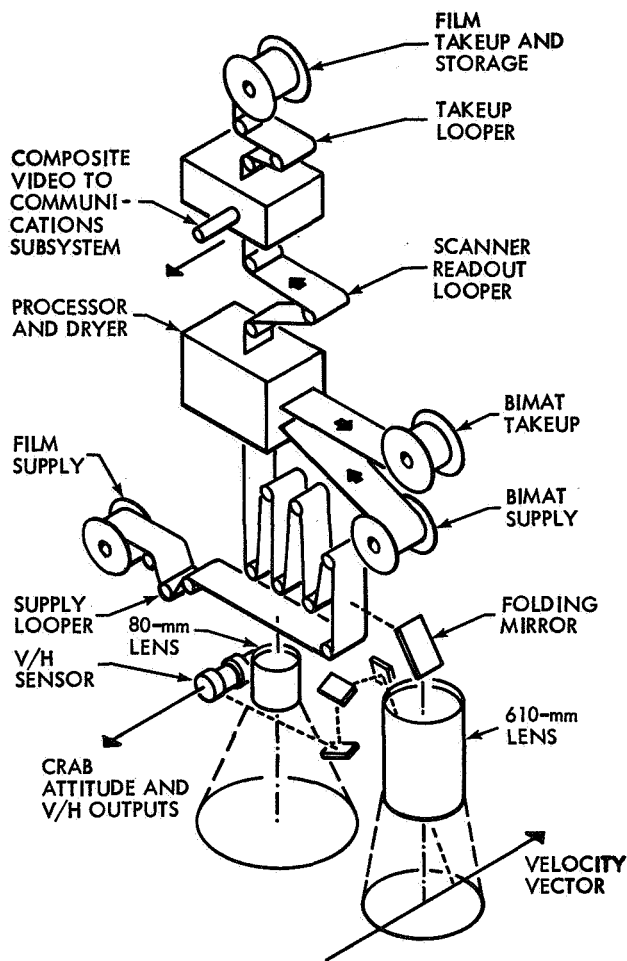Figure 5.- Lunar Orbiter Spacecraft.

9

Figure 6.- Photographic-subsystem functional diagram.

610-mm lens. Shutter speeds of 1/25, 1/50, or 1/100 sec are selectable by transmitted commands. The number of frames per sequence (1, 4, 8, or 16) and time interval between exposures are also selectable.

The film is held in the focal plane by platens which clamp it under vacuum and hold it flat during exposure. These platens move during exposure to reduce image smear caused by the rapid movement of the spacecraft over the lunar surface. This platen movement is referred to as image-motion compensation (IMC) and is provided through a mechanical linkage by an electro-mechanical device called a velocity over height (V/H) sensor. The V/H sensor determines the ratio of spacecraft velocity V to spacecraft altitude H by optically locking onto the image of the lunar surface in the high-resolution camera and causing the platens of each camera to move at the velocity of its image. The sensor also provides a measurement of yaw of the spacecraft (crab angle) which can be employed to correct spacecraft attitude.

In a normal photographic sequence, the spacecraft is oriented for photography, the lenses are uncovered by the opening of a thermal door in the spacecraft, the V/H sensor is activated, and the camera is turned on. After the "camera on" command, the cameras operate in an automatic sequence to (1) clamp film to the platen and draw it flat by differential pressure, (2) start moving the platens in synchronism with the image motion, (3) open the shutters for simultaneous exposures, (4) return the platens to the rest position, and (5) advance film for the next exposure. This sequence is repeated until all photographs commanded are taken.

After exposure, the film is stored in the camera storage looper. The camera storage looper consists of a series of fixed rollers in a stationary carriage and a series of rollers in a movable carriage which rides on a track. As film enters the looper, a spring causes the movable carriage to move away from the fixed carriage and thus to provide a storage capacity for up to 6 meters (20 ft) of film. This camera storage looper stores the film until it can be processed.

10

(A) GROUND FORMAT

(C) EDGE DATA STRIP – Includes 9-Level Gray Scale and Resolving Power Charts

Figure 7.- Film-format diagram.



a. SINGLE EXPOSURE AT THE 46 KILOMETER ALTITUDE; HIGH RESOLUTION COVERAGE IS 16.6 KM X 4.15 KM, MEDIUM RESOLUTION COVERAGE IS 37.4 KM X 31.6 KM.

b. DESIGN MISSION TARGET SITE COVERAGE, 16 CONSECUTIVE EXPOSURES DURING ONE ORBITAL PASS OVER THE TARGET SITE. THE INTERVAL BETWEEN EXPOSURES (APPROXIMATELY 2.2 SECONDS) IS TIMED TO PROVIDE OVERLAP OF THE HIGH RESOLUTION FRAMES.

c. EIGHT TYPICAL FRAMES FROM A SITE EXAMINATION TYPE MISSION - CONTIGUOUS HIGH RESOLUTION COVERAGE IS PROVIDED BY RAPID EXPOSURE RATE AS IN (b) TO GIVE HIGH RESOLUTION FORWARD OVERLAP AND BY PHOTOGRAPHING ON CONSECUTIVE ORBITS (9 & 10) TO GIVE HIGH RESOLUTION SIDE OVERLAP.

d. EIGHT TYPICAL EXPOSURES FROM A SITE SEARCH TYPE MISSION - STEREO MEDIUM RESOLUTION COVERAGE IS PROVIDED BY IN- CREASING THE TIME INTERVAL BETWEEN EXPOSURES (APPROX- IMATELY 8.8 SECONDS) TO OBTAIN 50% MEDIUM RESOLUTION FORWARD OVERLAP AND BY PHOTOGRAPHING ON ALTERNATE ORBITS (7 & 9) TO OBTAIN MEDIUM RESOLUTION SIDE OVERLAP.
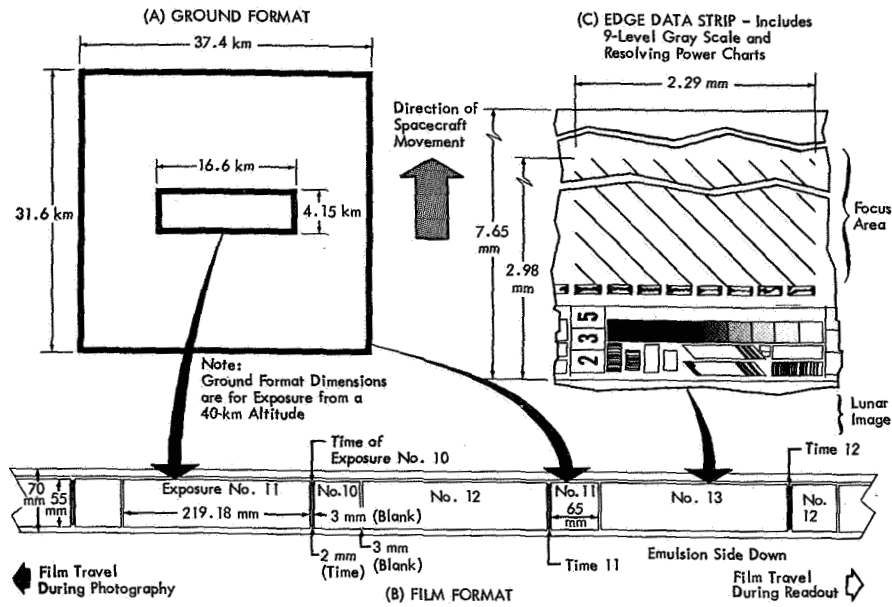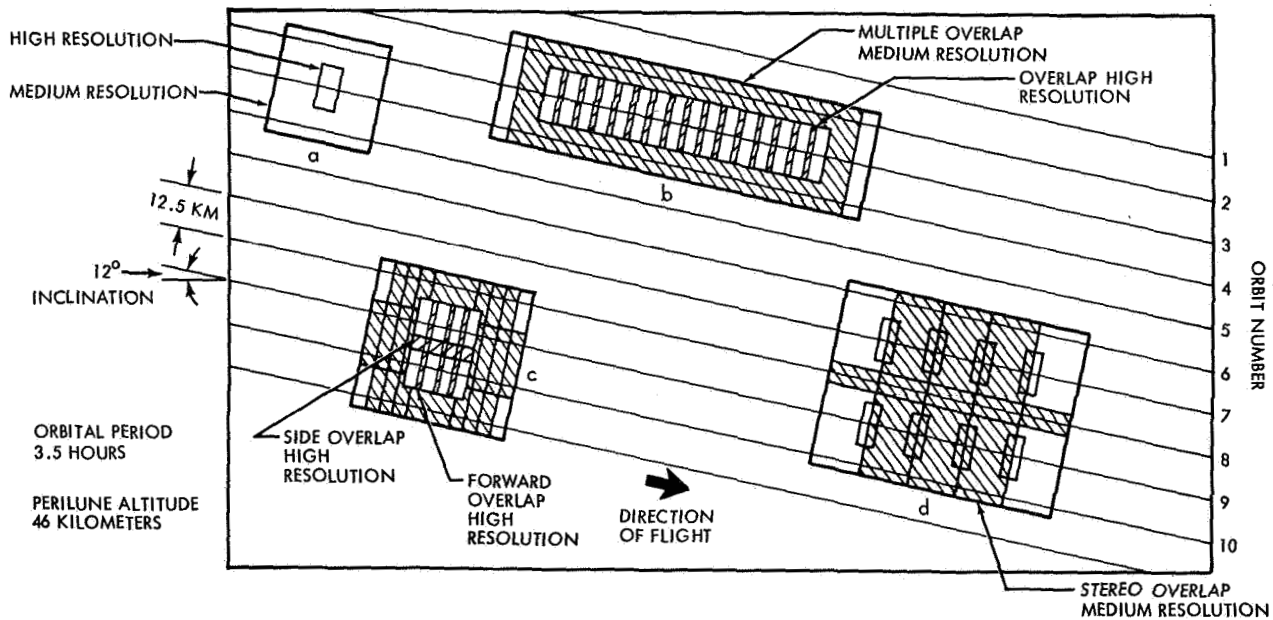
Figure 8.- Photographic modes.

11

After a photographic sequence, the photographic-subsystem processor-dryer, on command, processes film from the camera storage looper at a rate of 6.09 cm/min (2.4 in./min). The film is pressed into contact with Kodak bimat film, type SO-111, which accomplishes the processing. Kodak bimat film is a product consisting of a normal film base coated with a gelatin layer. This gelatin layer is presoaked with a special monobath processing solution. The solution both develops and fixes the photographic image during the 3.4 min the bimat and film are in contact on the processing drum. Processing temperature is closely controlled to 29.5° C.

After processing, the bimat and film are separated. The bimat moves to a takeup spool and the film passes onto a dryer drum. The film is in contact for a period of 11.5 min with the dryer drum which is controlled to a temperature of 35° C. Moisture driven from the film by the heat of the dryer drum is absorbed by special chemical salts in pads around the dryer, and thus a controlled humidity environment is maintained within the photographic subsystem.

After leaving the dryer drum, the film is transported through the readout storage looper and readout mechanism and is stored on a takeup spool. The film is now ready for readout.

At the completion of all photography, the procedure is to cut the bimat and read out the pictures by running the film in reverse and taking it up on the film supply reel. Because of limitations on the number of frames that can be scanned per orbit, this procedure takes about 2 weeks. However, throughout the mission, the readout looper provides the capability of reading out up to four frames at a time for priority return of important data and to provide monitoring of system performance.

The readout section (fig. 9) consists of a line-scan tube, a photomultiplier tube, and associated optics and electronics. In the line-scan t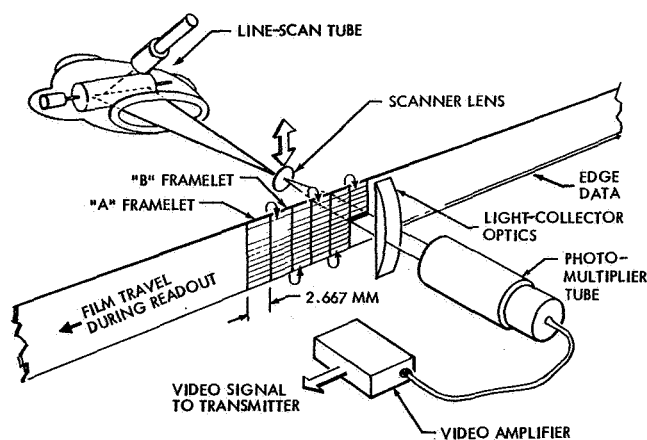ube, a spot of light (112 microns in diameter) from the electron gun moves linearly across the face of a revolving phosphor drum. Although the drum rotates so that on subsequent scans a different area is bombarded, the line produced remains fixed in space. The spot is focused by the scanner lens and projected as a reduced image (6.5 microns) onto the film. The lens is moved at right angles to the film after each scan. The result is a framelet consisting of 18 000 scan lines, each 2.67 mm long, across the width of the



Figure 9.- Film-scanning functional diagram.

12

70-mm film. At the completion of a framelet the film is advanced 2.54 mm prior to the next scan which is in the reverse direction across the film. A complete dual-exposure frame, 298 mm long, requires about 117 framelets.

The light passing through the film is modulated by image density and sensed by the photomultiplier tube through the associated light-collector optics. An electrical signal proportional to the intensity of the transmitted light is generated and amplified. Timing and synchronizing pulses are added. The video data, occupying a frequency spectrum from 0 to 230 kHz is then sent to the spacecraft communications equipment where it is modulated on a 310-kHz subcarrier (single-sideband, suppressed-carrier). The 310-kHz subcarrier oscillator also provides a 38.75-kHz pilot tone for transmission and subsequent subcarrier reinsertion by the ground equipment demodulator. The 50-bits-per-second pulse-code-modulation (PCM) telemetry data are diphased modulated ($0^o$ or $180^o$) onto a 30-kHz subcarrier. The video, pilot tone, and telemetry signals are summed, and the resulting composite signal phase modulates the S-band carrier.

The transmitted signals are received at one of the Deep Space Stations (DSS) located at Goldstone, California; Madrid, Spain; or Woomera, Australia. The 10-MHz intermediate frequency of the DSS receiver, containing the composite signal, is recorded on
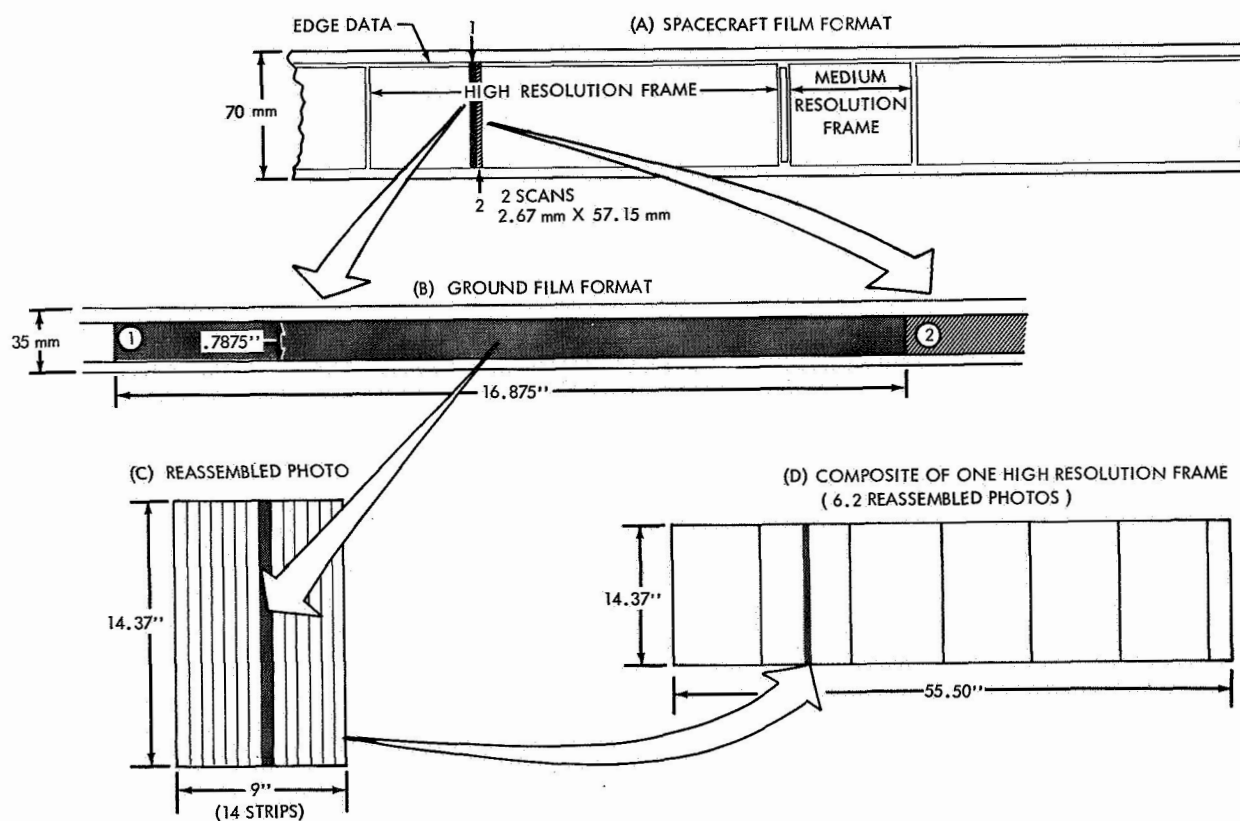


Figure 10.- Photograph reassembly.

magnetic tape for permanent storage. At the same time, it is passed to the ground communications equipment which recovers the telemetry and video. The video is sent to ground reconstruction electronics where it is converted to a line scan on a cathode-ray tube. The variations in light intensity on this cathode-ray tube correspond to the variations in image density on the spacecraft film.

The line on the cathode-ray tube is recorded on a moving roll of 35-mm television recording film SO-349. The image on the 35-mm film is more than seven times the size of the image on the spacecraft film. After processing, the film is reassembled by a reassembly printer. This equipment prints, on Kodak 24.2-cm aerographic duplicating film (type 5427), 14 trimmed 35-mm framelets, side by side, to make up a subframe. At least two subframes are required to constitute a medium-resolution photograph, and at least seven subframes for a high-resolution photograph. Photographic reassembly is illustrated in figure 10.

A summary of the photographic-subsystem component specifications is as follows:

Photographic package:

Dimensions, cm . . . . . . . . . . . . . . . . . . . . . . . . . . . . . 66 by 58.8 by 81.3

Weight, kg . . . . . . . . . . . . . . . . . . . . . . . . . . . . . . . . 65.8

Temperature, °C . . . . . . . . . . . . . . . . . . . . . . . . . . . . 10 to 21

Pressurization, kg/m$^2$ abs . . . . . . . . . . . . . . . . . . . . . 703.1 to 1336

Relative humidity, percent . . . . . . . . . . . . . . . . . . . . . . . 50 ± 20

Lenses:

|  | High resolution | Medium resolution |
|---|---|---|
| Type. . . . . . . . . . . . . . . . . . . . . . . . . | Paxoramic | Xenotar |
| Elements . . . . . . . . . . . . . . . . . . . . | 6 | 5 |
| Focal length, mm . . . . . . . . . . . . . . | 610 | 80 |
| Diameter, cm . . . . . . . . . . . . . . . . . | 13.83 | 3.627 |
| Length, cm . . . . . . . . . . . . . . . . . . | 23.132 | 3.772 |
| Maximum relative aperture . . . . . . | f/5.6 | f/2.8 |
|  |  | (stopped at f/5.6) |
| Shutter . . . . . . . . . . . . . . . . . . . . | focal plane | between lens |
| Exposure, sec. . . . . . . . . . . . . . . . . | 1/25, 1/50, 1/100 | 1/25, 1/50, 1/100 |
| Half-field angle, deg . . . . . . . . . . | 10.5 | 28.0 |
| Film image, cm . . . . . . . . . . . . . | 5.51 by 22.29 | 5.51 by 6.5 |
| Resolution (on axis), lines/mm . . . . | 115 | 115 |

Film (EK-SO-243):

Width, mm . . . . . . . . . . . . . . . . . . . . . . . . . . . . . . . . . . . . . . . . . 70

Length, m . . . . . . . . . . . . . . . . . . . . . . . . . . . . . . . . . . . . . . . . . 80

Thickness, mm . . . . . . . . . . . . . . . . . . . . . . . . . . . . . 1.473

Weight, kg . . . . . . . . . . . . . . . . . . . . . . . . . . . . . . . 1

Exposure index . . . . . . . . . . . . . . . . . . . . . . . . . . . . 1.6

Resolution, lines/mm . . . . . . . . . . . . . . . . . . . . . . . . . 250

Processing (lamination with EK-SO-111):

Processing speed, cm/min . . . . . . . . . . . . . . . . . . . . . . . 6.1

Processing time, min/frame . . . . . . . . . . . . . . . . . . . . . . 3.22

Processing temperature, °C . . . . . . . . . . . . . . . . . . . . . 29 ± 0.5

Drying speed, cm/min . . . . . . . . . . . . . . . . . . . . . . . . 6.1

Drying time, min/frame . . . . . . . . . . . . . . . . . . . . . . . 11.7

Drying temperature, °C . . . . . . . . . . . . . . . . . . . . . . 35 ± 1.0

Readout:

Line-scan tube:

Drum speed, rpm . . . . . . . . . . . . . . . . . . . . . . . . . . 1000

Line length, cm . . . . . . . . . . . . . . . . . . . . . . . . . . 6.03

Spot diameter, microns . . . . . . . . . . . . . . . . . . . . . . 112

Scanner lens:

Focal length, mm . . . . . . . . . . . . . . . . . . . . . . . . . 13.3

Aperture . . . . . . . . . . . . . . . . . . . . . . . . . . . . f/2.4

Half-field angle, deg . . . . . . . . . . . . . . . . . . . . . . . 7.7

Film scan:

Scan line interval, lines/mm . . . . . . . . . . . . . . . . . . . . 286

Scan line length, mm . . . . . . . . . . . . . . . . . . . . . . . 2.67

Spot diameter, microns . . . . . . . . . . . . . . . . . . . . . . 6.5

Readout rate, sec/framelet . . . . . . . . . . . . . . . . . . . . . . 22

Framelet size, mm . . . . . . . . . . . . . . . . . . . . . . . . 2.67 by 57.58

## PHOTOGRAPHIC COVERAGE

During the period of photography, 211 exposures were made, each exposure consisting of a high-resolution frame and a medium-resolution frame. Because of difficulties with the high-resolution shutter, only 13 of the high-resolution frames were of good quality. The distribution of the photographs taken was as follows:

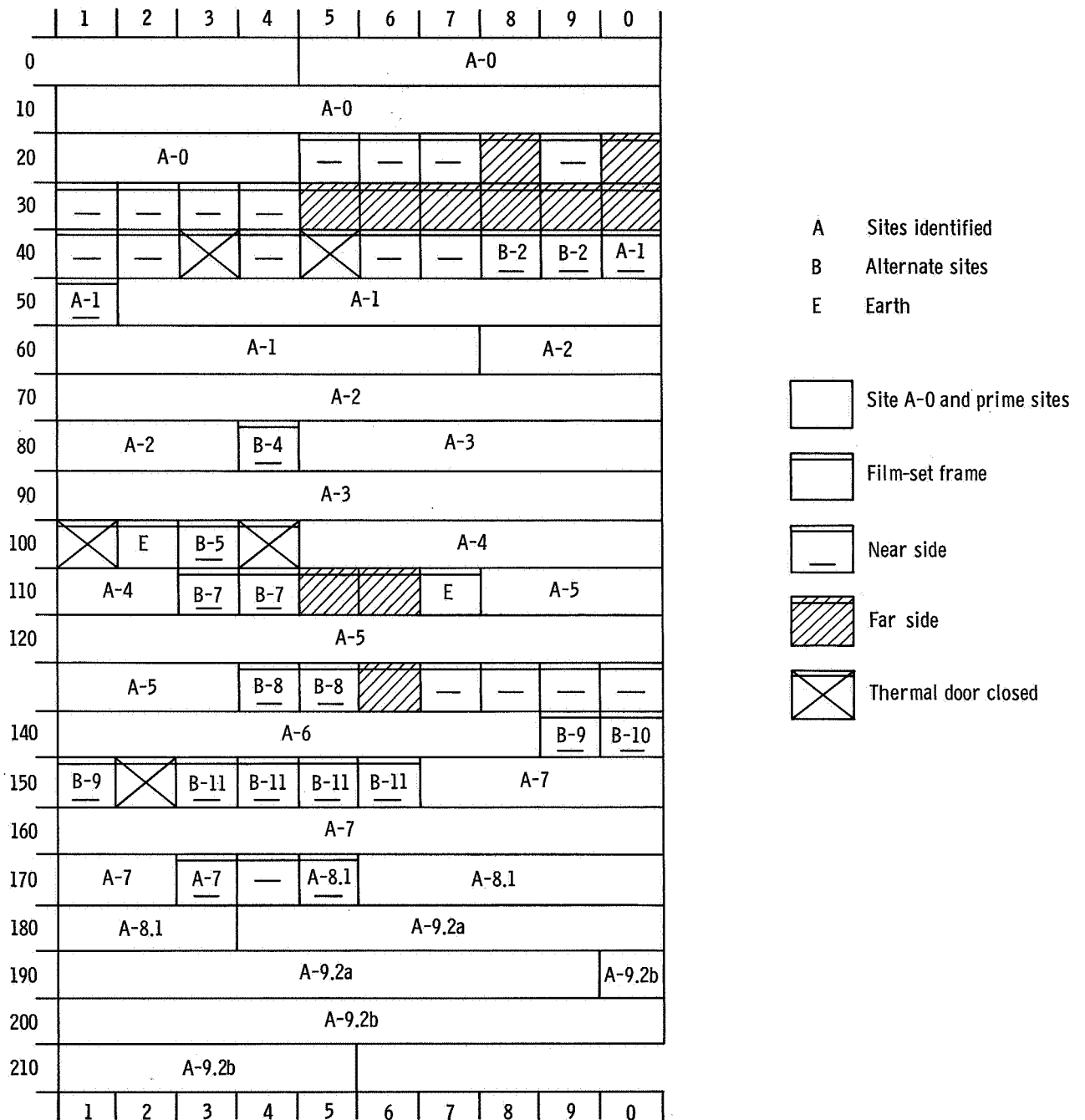| | |
|---|---|
| Site A-0 (high orbit) | 20 |
| Prime sites (A-1 to A-9.2) | 136 |
| Film set frames: | |
| Alternate sites (B sites) | 15 |
| Far side | 11 |
| Near side | 22 |
| Earth | 2 |
| Thermal door closed | 5 |
| | 211 |

Figure 11.- Distribution of Lunar Orbiter I photographs.

16

This distribution is illustrated in figure 11, which shows the sequential order of all photographs taken of prime and other sites. The location of each of the photographs with respect to the lunar surface is shown in the appendix in maps 1 and 2 which were prepared by the Aeronautical Chart and Information Center (ACIC).

# SCIENTIFIC RESULTS

# LUNAR SURFACE CHARACTERISTICS

## TERRAIN ASSESSMENT APPROACH

### Selection of Terrain Units

In view of the methods employed by the group analyzing the Lunar Orbiter I photography for rapid data screening for potential Apollo sites, much of the information gathered for this section of the report is keyed directly to the specific target sites photographed and treated as individual study areas. Major terrain units were selected on the basis of earth-based observations at an average resolution of about 1 km, and geologic terrain mapping was employed as the basic means of evaluating and comparing the roughness of the sites. This type of mapping delineates units with different morphologic characteristics. These units are listed as follows in order of increasing relative roughness as determined from earth-based observations:

> Dark mare
> Average regional mare
> Mare ridges
> Upland plains
> Ray-covered mare
> Floor of deformed craters
> Subdued uplands
> Crater rim
> Sculptured uplands

Once delineated, the terrain units were described and characterized by crater size-frequency and slope-measurement data. The derivation of these data and their implications as to relative roughness are briefly discussed for parts of all the sites except two (A-2 and A-6) where resolution was reduced because of lighting and exposure conditions. Brief explanations are presented in the appendix with the map for each site. The mapping was done on preliminary photographs prepared at an approximate scale of 1:90,000. Some stereoscopic examination was made, but monoscopic examination was more usual.

Crater-density data have been used as an index of the comparative roughness of the smoothest terrain units. Crater counts were made in sample areas of 50 $km^2$ with crater-diameter intervals of 50 meters. Crater density is not, however, a precise index of total roughness. Variations in crater morphology are also important but have not been considered here.

Some slope and topographic-profile information has been obtained for specific areas by photogrammetric and photoclinometric techniques. These data are included herein.

## Effect of Conditions of Photography

Variations in crater resolution, within a site and between sites, are caused by differences in sun angle, albedo, large-scale relative roughness, and photographic quality. The Lunar Orbiter I photographic subsystem appears to have had greater latitude at low sun angles and less latitude at high sun angles (angle above horizon > 25°) than anticipated. Identification of craters is seriously hampered by high sun angles, because the contrast is lowered and shadows are generally absent. Albedo variations and relative roughness are additional complicating factors. Shutter settings were based on the average albedo for the terrain units of primary interest. Areas which deviate markedly from this value are, consequently, not photographed at the optimum exposure. Large-scale relative roughness has a similar effect on photographic quality. Overexposure occurs on slopes inclined toward the sun as the sun angle is effectively increased. On the other hand, the sun angle is effectively lowered on slopes inclined away from the sun. These factors, combined in a complex way, cause variations in effective identification of lunar surface detail.

Table I shows the variations of some of the parameters and the resulting crater-size detectability. The smallest crater detectable at a given site is a function of many parameters, including some not shown in the table, such as altitude above the surface and actual lunar surface albedo obtained locally. It is evident that sites A-2, A-6, and A-7 have the

TABLE I.- SUN ANGLES AND ALBEDO DATA FOR LUNAR ORBITER I PRIME SITES

SHOWING DIFFERENCES IN EFFECTIVE RESOLUTION

| Site | Frame | Sun angle, deg | Albedo (a) | | Shutter setting, sec | Diameter of smallest crater detected on slopes away from sun, meters | Diameter of smallest average crater detected in sample level areas, meters |
|------|-------|----------------|------|--------|----------------------|------|------|
| | | | Mare | Upland | | | |
| A-1 | M-67 | 29.1 | 0.081 | 0.121 | 1/50 | 19.0 | 19.0 |
| A-2 | M-73 | 24.6 | 0.076 | 0.118 | 1/50 | 23.0 | 33.0 |
| A-3 | M-85 | 20.7 | 0.075 | ---- | 1/25 | 9.5 | 14.0 |
| A-4 | M-107 | 21.5 | ---- | 0.135 | 1/50 | 14.0 | 18.0 |
| A-5 | M-121 | 21.4 | 0.076 | ---- | 1/50 | 9.0 | 10.5 |
| A-6 | M-141 | 35.9 | ---- | 0.125 | 1/100 | 25.0 | 27.0 |
| A-7 | M-165 | 31.7 | 0.076 | ---- | 1/50 | 26.0 | 30.0 |
| A-8.1 | M-183 | 30.7 | 0.069 | ---- | 1/50 | 17.0 | 22.0 |
| A-9.2a | M-190 | 26.4 | 0.066 | ---- | 1/50 | 12.0 | 14.0 |
| A-9.2b | M-212 | 26.8 | 0.068 | ---- | 1/50 | 12.0 | 16.0 |

[a]Albedo obtained by Robert Wildey and Howard Pohn with U.S. Geological Survey 30-inch telescope, June 1966.

least effective resolution (largest minimum-size crater). Photogeologic interpretation and mapping for comparative purposes is not feasible or, at least, is made difficult in areas where the photographic quality is degraded. Lunar Orbiter I sites A-2 and A-6 are, therefore, not considered in detail in this preliminary analysis and only parts of sites A-1, A-8.1, and A-4 have been evaluated. Site A-7 has been evaluated, however, in spite of the overexposure of the film caused by high sun angle and high reflectance, because of its importance to Apollo site-selection analysis.

## Photographic Processing

A number of steps in photographic processing affect the overall quality of negatives and contact prints. The most serious of these is in the initial production of 35-mm film (by the Ground Reconstruction Equipment (GRE) from the magnetic-tape recordings of the telemetered video signal). Constant settings of the contrast ratio on the GRE yield photographs which incorporate the effects of the previously mentioned variables. Some areas were, therefore, "overexposed" on both negatives and prints. By increasing the contrast control on the GRE, the average resolution was considerably increased in these areas when new negatives were produced from the original magnetic-tape data. Counts of total craters in the same area of site A-7 on a "low gain" and on a "high gain" print of a medium-resolution frame illustrate the effective enhancement of this originally over-exposed area (fig. 12). Approximately twice as many small craters were measured on the high-gain photograph as on the low-gain photograph. The significance of this difference is apparent when the A-7 curves are compared with the cumulative size-frequency distribution function representing the Surveyor I area in site A-9.2. The low-gain print gives a false impression that the area is relatively smooth. Crater size-frequency data have also been plotted from high-gain photographs for sites A-1, A-4, A-8.1, as well as A-7. Although these data do not completely eliminate the variations in photographic quality and resolution, the roughness estimates are generally suitable for providing some quantitative confirmation of the visual classification shown on the geologic



Figure 12.- Cumulative crater size-frequency distributions for an area in site A-7 as measured on low- and high-gain reconstructed prints and for Surveyor I area of site A-9.2 (SS-1).

terrain maps. It should be noted, however, that such gain adjustment to favor overexposed areas will reduce the detectability of features in areas originally in shadow and now submerged in increased effective shadow.

## Photographic Supporting Data

Spacecraft altitude for photographic scale calculations and solar incidence angle for determining crater depth by shadow-measurement methods were necessary inputs for Apollo landing analysis screening procedures. Unfortunately, the only data available during screening operations were the computer-predicted data calculations rather than actual tracking data. Photographic scale errors of 5 to 10 percent are possible from the predicted data.

## Crater-Diameter Determination

One of the techniques used in the study of the lunar terrain is the determination of the crater diameters and depths. For rapid screening of the large number of Lunar Orbiter photographs for Apollo landing-site selection, a nominal diameter-to-depth ratio was established for a particular frame. The purpose of this particular approach was to obtain and define a crater diameter critical to the Apollo landing. The crater depth was established either by parallaxbar measurements or by a shadow-measurement method. If the sun elevation angle was not too large, the shadow method was preferred.

## Delineation of Rough Terrain

Many areas, such as hilly regions with steep slopes with a high density of craters, large craters, closely spaced craters, crater chains, high escarpments, and single hills, which are obviously unsuitable for Apollo landings but nevertheless of scientific interest, are delineated on the available photography for each site. Stereoscopic evaluation was made to aid this interpretation where stereoscopic photographic coverage was available. If stereoscopic coverage was not available, this delineation was made monoscopically.

## Crater Counts

For the crater-count survey at each site, the nominal crater size was determined according to the following measurement criteria:

| Diameter class, mm | Mean value, mm | Nominal crater size, m |
|---|---|---|
| 0.0 to 0.5 | 0.3 | 27 |
| 0.5 to 1.0 | .75 | 70 |
| 1.0 to 1.5 | 1.25 | 110 |
| 1.5 to 2.0 | 1.75 | 160 |
| Measure all craters greater than 2.0 | Measured value | |

In general, the crater-count survey included the range of diameters from about 30 meters to 1000 meters.

## Profiles

Profiles were derived photogrammetrically on a stereocomparator over some of the areas. The purpose of the profiles, in addition to the evaluation of crater geometry, was to determine the slopes in certain areas caused by features other than craters. Also, regional slopes across the areas may be determined from these profiles.

The slope values presented in this report include inherent errors due to framelet distortions and inaccuracies of the stereoscopic measurements. Therefore, they are only approximate values.

## Nomenclature

Inasmuch as the material presented in this report was obtained from varied sources without a standard set of definitions or nomenclature, the following explanations are presented.

The nomenclature for Apollo sites photographed by Lunar Orbiter I was established as A-1, A-2, to A-9.2. The letter A has no particular significance other than being indicative of the first flight or Mission I. The decimal identification of a site such as 8.1 or 9.2 merely indicates a change (either prior to or during flight) in the final site selection from that originally planned.

Geologic features of the lunar terrain are identified as follows. The four basic terrain units are represented by Roman numerals: Mare (I), Upland (II), Craters (III), and Structural Features (IV), as defined by Halm. Subunits of classification in each basic terrain unit are groups represented by capital letters and subdivisions of these groups represented by Arabic numerals. In a few instances it was necessary to represent a further breakdown of special terrain units by lowercase letters. For example, a crater rim with bright halos and rays, so defined, is III-A-3c.

# ANALYSIS

The following material is a brief description of each of the prime sites photographed by Lunar Orbiter I and, in most cases, some preliminary terrain assessment observations. The geologic interpretation of each site is accompanied by a tabulation of the terrain types identified on the site photographs. The terrain maps have some specific differences in the notations for terrain types due to the particular method used by the different members of the screening group. Although details varied, the definitions of basic terrain types noted in the section of this report entitled "Selection of terrain units" were used by all analysts. Most of the overall terrain assessment was conducted by study of the framelets reassembled into site or area geologic terrain maps. Each site is located, for reference purposes, on the ACIC lunar charts prepared from earth observations.

## Site A-1

Location.- Site A-1 lies within the lowlands of the western extremity of Mare Fecunditatis and a portion of the eastern extremity of the continental central highland. It is covered by Lunar Orbiter I medium-resolution frames 52 to 67. The selenographic coordinates for the corners of the site are:

| Longitude | Latitude |
|-----------|----------|
| 40.3° E | 0.2° N |
| 40.0° E | 1.2° S |
| 43.8° E | 0.5° S |
| 43.5° E | 1.9° S |

as illustrated in figure 13, the index map for the site.

Preliminary terrain assessment.- Site A-1 includes both mare and upland terrain. The geologic features, shown in map 3, and the detailed map explanation are presented in the appendix. The geologic terrain analysis was made by Terry W. Offield of the U.S. Geological Survey.

Mare (I).- The mare surface in this site is apparently homogenous, moderately cratered, and only slightly lineated. The cumulative crater size-frequency distribution in figure 14 indicates a moderately cratered surface.

Upland (II).- Upland topography borders the mare on the west (map 3). Small-scale roughness and a high density of small craters can be discerned on slopes with low effective sun angles. Horizontal to subhorizontal layering or fracturing can also be detected. This upland area has high relief relative to the mare.

Terraces (II-B$_1$) commonly occur at the base of steep upland slopes. This unit is probably formed by mass-wasting of material from the steep slopes.
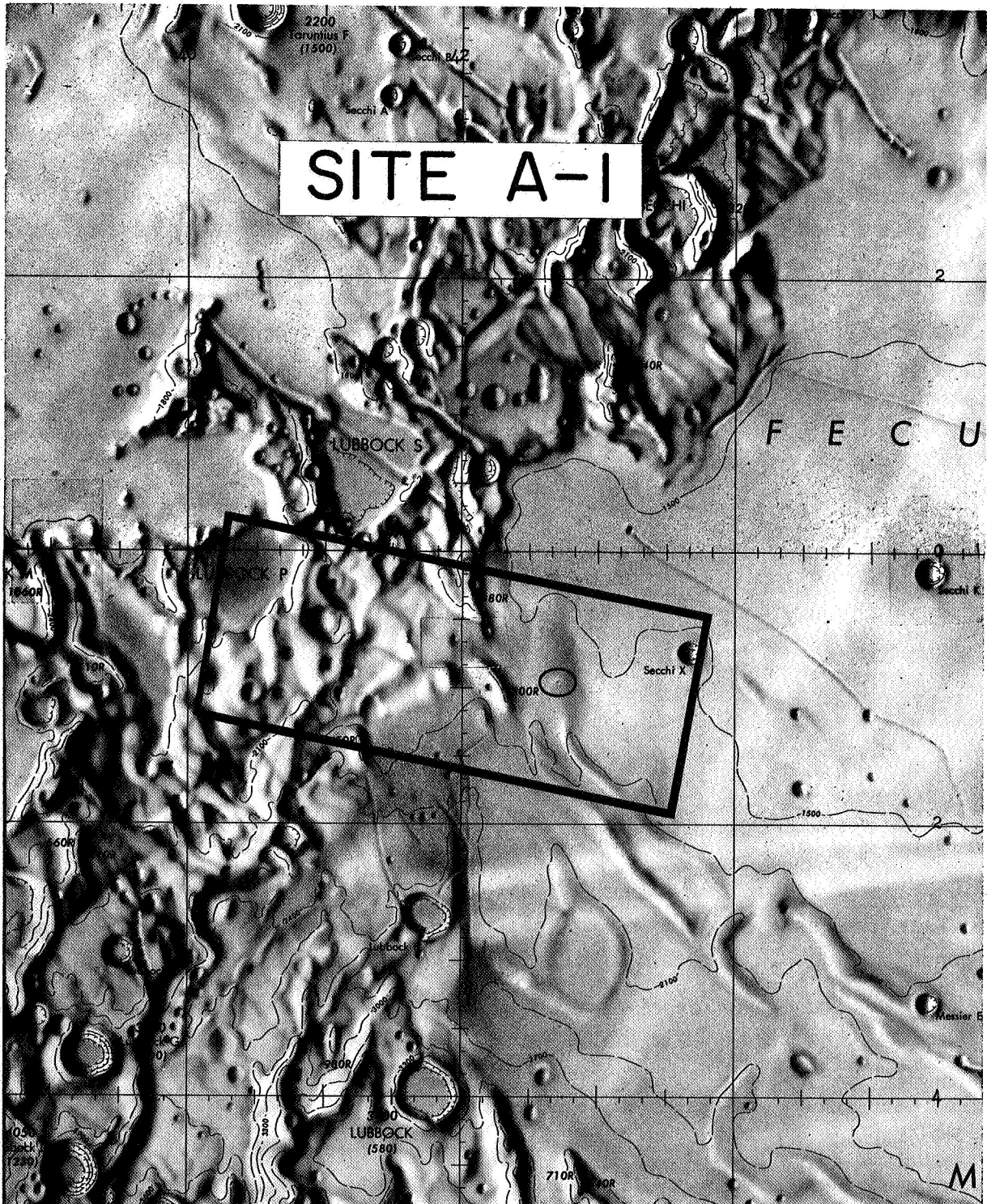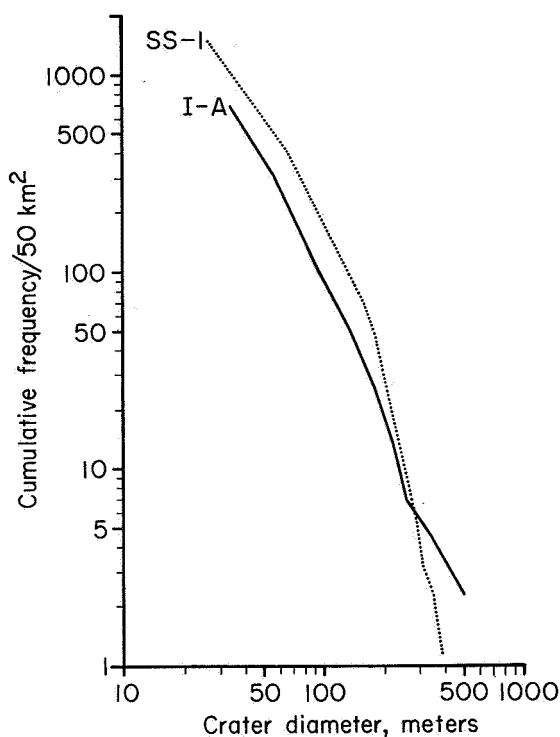
Figure 13.- Index map for site A-1.

Figure 14.- Cumulative crater size-frequency distribution for regional mare (I-A) in site A-1 compared with that for representative dark mare sample (SS-1) in Surveyor I area of site A-9.2.

Crater (III).- Craters vary from well-formed (III-A) to shallow subdued craters (III-B) (map 3). Craters with bright rims and rays (III-A-3c) appear to be randomly distributed on the mare and characteristically have rough terraced, rubbly walls (III-A-1a). The mare has a mottled appearance, which possibly suggests a high density of craters smaller than the limit of resolution (20 meters).

Blocks elevated above the general mare surface appear to be remnants of a large, pre-mare crater. This conclusion is based primarily on studies made at earth-based resolutions (Terry W. Offield, U.S. Geological Survey, 1966). Layering and fracturing is observed in a few places on these exposures.

Structural features (IV).- The mare surface is complicated by structural and volcanic features such as rills (IV-C-1), chain craters (IV-H), domes (IV-B), low ridges (IV-A), faults, lineaments, and irregular depressions (IV-G). These units are described in the geologic-terrain map explanation and shown in map 3.

The only infrared anomaly (J. M. Saari and R. S. Shorthill, Res. Note 66-4, Boeing Sci. Res. Lab., Nov. 1966) is centrally located within the site. Two named features are included within the limits of the site photographed: Secchi X and Lubbock P.

The high sun elevation (29°) at the time of the site A-1 photography reduced the shadow lengths and in many cases may have resulted in no shadows being cast by craters or protuberances. Thus, many small objects in the mare areas, or even relatively large objects in hummocky areas, where slopes may tend to increase the relative sun elevation, may be unidentifiable.

Site A-2

Location.- Lunar Orbiter site A-2 is a highland site bordering the southeast part of Mare Tranquillitatis. It is covered by medium-resolution frames 68 to 83. The selenographic coordinates for the corners of the site are:

| Longitude | Latitude |
|-----------|----------|
| 34.0° E | 1.1° N |
| 33.7° E | 0.2° S |
| 37.7° E | 0.4° N |
| 37.0° E | 0.9° S |

as illustrated in figure 15, the index map for the site. A subframe from high-resolution frame H-70 was also studied in the evaluation of site A-2.

Preliminary terrain assessment.- The quality of photography did not permit terrain assessment to the desired degree. However, the general nature of the terrain of the region is shown in the appendix in map 4. A better analysis will be possible by use of enhanced photographs.

Three named features within the boundaries of this site are crater Censorinus V, hill Maskelyne Zeta, and crater Maskelyne TA.

It is of interest to note that in the area of this particular site available lunar charts show areas of smooth terrain in certain regions with occasional grouping of craters 2 to 3 km in diameter. However, these medium-resolution photographs from Lunar Orbiter I reveal as many as 20 craters 1/2 to 3/4 km in diameter in a local region bounded by an 8- by 5-km ellipse and numerous smaller craters of all sizes down to the resolution limit of the medium-resolution photography. Craters less than 23 meters in diameter were too indistinct to be measurable. An analysis of one nearby, similar area covered by both medium- and high-resolution photography indicates approximately $2\frac{1}{2}$ times as many craters visible in the high-resolution photograph as there were in the medium-resolution photograph. This frame of high-resolution photography was smeared, but craters as small as 13 meters in diameter could be measured. The sun elevation angle at the camera intersect point was 23.7°, which should not cause an appreciable loss of detail. However, a close inspection of the photography indicates that within this area there is a high percentage with a loss of detail. In fact, an early photograph of part of this region taken a few orbits prior to passing over this site shows numerous slope reversals present in areas indicated "relatively smooth," a result which further emphasizes the significance of lighting angle on the reflectance level and its influence on the amount of detailed interpretation of lunar terrain that can be made with confidence.

## Site A-3

Location.- Site A-3 lies in southwestern Mare Tranquillitatis. It is covered by Lunar Orbiter I medium-resolution frames 85 to 100. The selenographic coordinates for the corners of the site are:
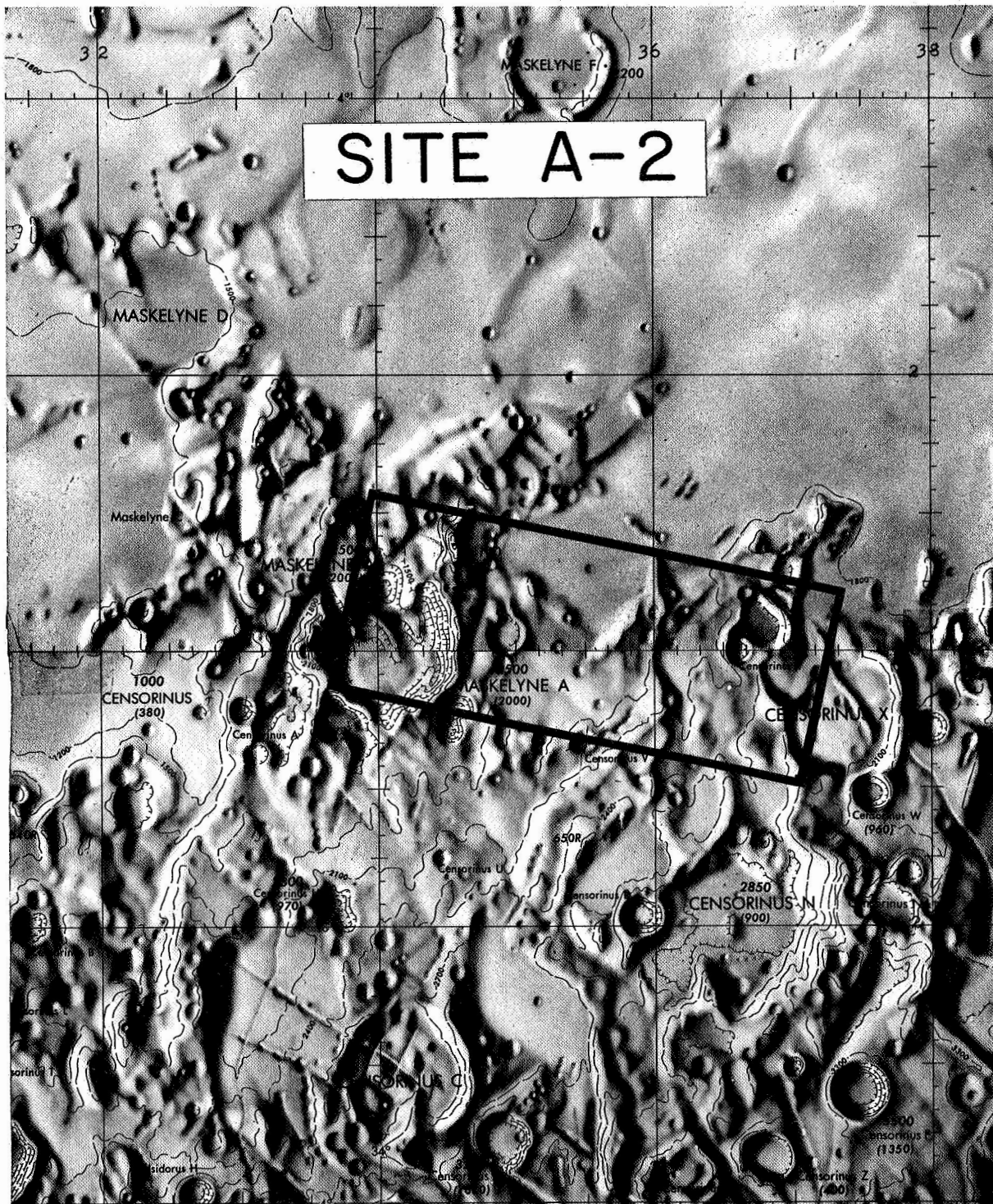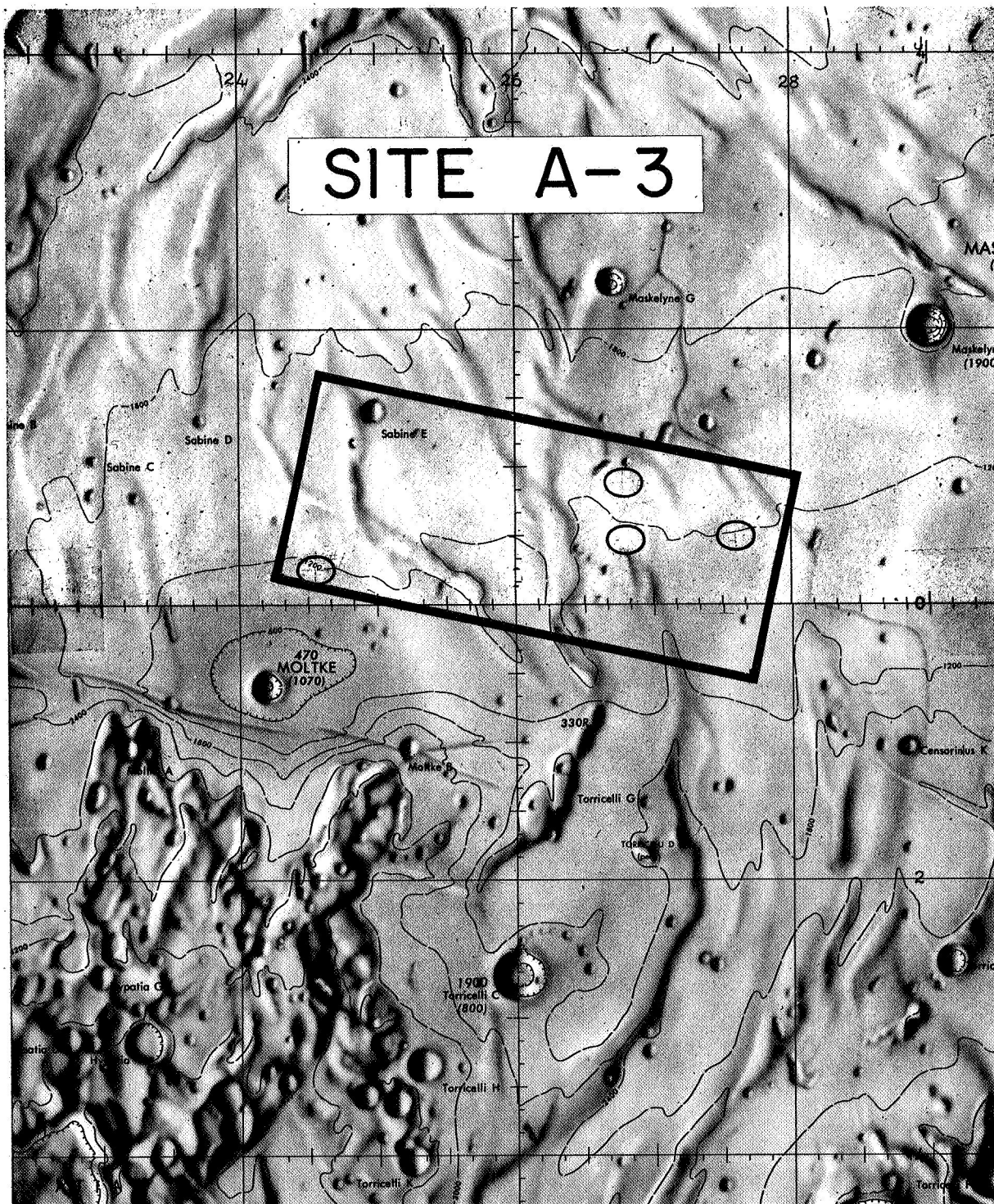
Figure 15.- Index map for site A-2.

Figure 16.- Index map for site A-3.

| Longitude | Latitude |
|-----------|----------|
| 24.6° E | 1.6° N |
| 24.3° E | 0.2° N |
| 28.0° E | 0.9° N |
| 27.7° E | 0.5° S |

as illustrated in figure 16, the index map for the site.

Preliminary terrain assessment.- The terrain map for site A-3 is given in the appendix as map 5 and is accompanied by the explanation of geologic features. The geologic terrain analysis was made by Maurice J. Grolier of the U.S. Geological Survey. The nominal site is divisible into two regions of approximately equal area: a western part, which appears darker and smoother in earth-based photographs, and an eastern region interrupted by subparallel ridges trending northwestward (Maurice J. Grolier, U.S. Geological Survey, 1966). A 1° shift eastward in the location of the center from the nominal site occurred during the mission, so that only a small, but still representative, sample of the western region was photographed.

Mare (I-A).- The average regional mare is a plain of relatively low relief, varying in crater density and size. The mare surface is interrupted by northwestward-trending ridges and a small segment of a rill, Rima Maskelyne I, in the extreme northeast corner of the site. Depressions, crater fields, isolated boulders, and a few domelike hills are present. At small scale, all these features contribute to the surficial roughness of the mare.

The mare surface is cratered at varying densities and is divided accordingly into three subunits: a rougher mare (I-A-1), a smoother mare (I-A-2), and a rayed mare (I-A-R).

Areal statistical samples are outlined in map 5. The rougher mare becomes more areally extensive, eastward across the site. Its crater density is 670 craters (34 meters in diameter) per 50 km². Unit I-A-1 in this site is apparently smoother than the mare surface at the Surveyor I landing site in Oceanus Procellarum (Lunar Orbiter site A-9.2) for craters less than 200 meters in diameter. For larger craters, the Surveyor I landing site is smoother (fig. 17).

The smoother mare unit, I-A-2, has a crater density ranging from 600 to 740 craters (34 meters in diameter) per 50 km². The unit is generally less densely cratered than the Surveyor I landing site, except for craters that are more than 200 meters in diameter (fig. 17).

Mare unit I-A-2 is smoothest in the southwestern corner of the site. The cumulative size-frequency curve shows a crater density of 230 craters (32 meters in diameter) per 50 km² (not shown in fig. 17). Even in this sampled area, unit I-A-2 has a higher
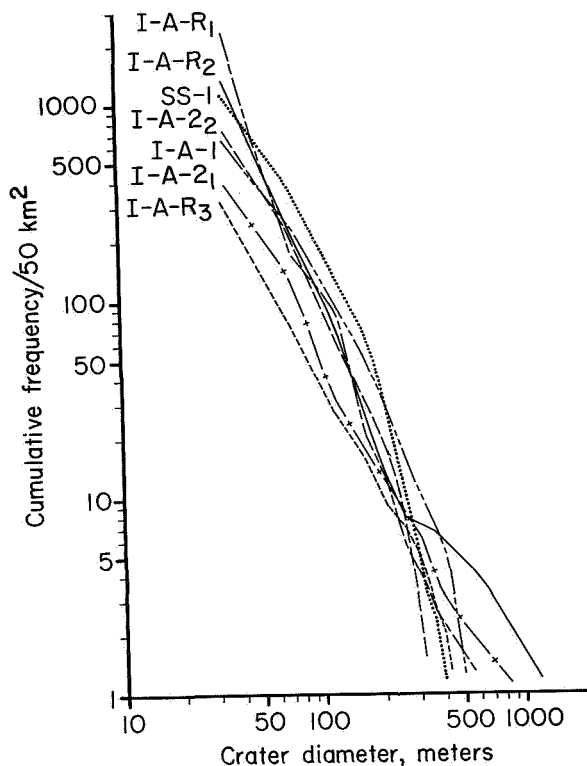
Figure 17.- Cumulative crater size-frequency distributions for samples of various mare units in site A-3 compared with that for representative dark mare sample (SS-1) in Surveyor I area of site A-9.2.

crater density than the Surveyor I landing site for craters more than 235 meters in diameter.

The rayed mare, I-A-R, has a slightly higher reflectivity than the surrounding mare, and locally may even display a specular quality as noted near the center of map 5. The rayed mare, especially in the western half of the site, is rougher than the Surveyor landing site for craters smaller than 45 meters in diameter. It may even be very densely pitted, with pits about 25 meters wide and about 5 meters deep.

The three mare subunits are comparable in crater density for craters ranging from 60 to 130 meters in diameter. The easternmost ray in the eastern quarter of the site (map 5) has the lowest crater density in the entire site. This ray has about 325 craters (34 meters in diameter) per 50 km$^2$ and appears relatively smooth. The reflectivity of this ray is diffuse and intermediate between the reflectivity of other rayed mare areas

(0.096 to 0.102) and that of ridges within the site (0.109 to 0.114). The diffuse reflectivity of this ray appears related to the thinness of the deposit and its lateral gradation onto non-rayed mare. Craters older than the ray are not completely obliterated; they appear subdued under or through the ray. Some craters, mostly in the diameter range between 33 and 70 meters, appear to be contemporaneous with, or more recent than, the ray. These craters are sharp, well-formed, and commonly exhibit a light halo around them. Their occurrence is in a ratio of 1 to 2.5 with that of the craters older than the ray.

The relative smoothness of the rayed mare can be visually appraised in Lunar Orbiter medium-resolution photographs. It is confirmed by statistical analysis, at least within a broad range of crater diameters in the three areas sampled.

Apparently, the rayed mare in the eastern region of the photographed area does not stand in positive relief above the surrounding mare; it even appears slightly lower. The hypothesis is that the surficial roughness of a ray might be related to the distance to the crater from which it originates. At long distances from the crater of origin, deposition

32

rather than pitting may occur and slight compressing or reworking of the lunar surficial layer at the time of ray deposition may have a smoothing effect on mare topography.

Craters (III-A).- Craters are divided into well-formed and subdued craters. Only the largest of the well-formed craters, about 1 km in diameter or more, have been differentiated. Most of these craters have raised rims that exhibit rather high reflectivity toward the sun. (As used in this report, "raised rim" applies to either bedrock raised above the level of surrounding mare by mechanical deformation or to a ring of ejecta.) Lunar slopes and, to a lesser extent, crater rims are commonly lined with slump terracettes.

The largest crater is Sabine E, a well-formed, almost rimless crater of high reflectivity in the northwest corner of the site. Sabine E is about 5 km wide and 0.790 km deep (AIC chart 60C). A peculiar matted structure, not unlike burlap weave, is displayed along the inner slopes of Sabine E. This structure, made up of both radial and concentric "threads," may or may not reflect the bedrock that underlies the lunar surface. "Burlap weave" structure is prominently and repeatedly displayed in the walls of crater fields, depressions, escarpments, and fault scarps. It is distinct from slump terracettes, and appears to be a bedrock characteristic at or near the lunar surface at the resolution of Lunar Orbiter medium-resolution frames. The threads in the weave observed in escarpments are nearly at right angles to each other and trend northwest or northeastward.

Well-formed craters of many kinds, in the 50- to 100-meter-diameter range, dot the mare surface. They include craters with a raised rim, or even a lip, craters with a light halo around a rim with or without rays, and craters with very rugged, nearly vertical interior walls, and a circular shelf down the wall. The shelf is suggestive of the existence of a lunar surficial layer. Subdued craters, mostly less than 0.5 km in diameter, rimless or with low rim, dot the mare surface. They are, for the most part, features of negative relief and of varying depth.

Crater fields (III-C).- Most crater fields are elongated clusters of ghostlike, overlapping craters, with angular outlines. Commonly, the cluster exhibits a raised rim, which, in distinction with the raised rim of most well-formed craters, appears to involve bedrock deformation around the crater field. Large crater fields include from two to several dozens of individual craters, commonly arranged linearly.

Another type of crater field involves very closely spaced, separate subdued craters, generally less than 0.5 km in diameter. This type of crater field, although not differentiated from the first type, is little more than a very rough, densely cratered mare.

Crater fields have a low crater density with a certain range of crater diameter and may be smoother than the mare itself. They appear to share this characteristic with parts of mare ridges and mare depressions. This rather surprising and unexpected

finding may be due to the obliteration of many craters by slumping along steep slopes, or by smoothing processes associated with uplift, collapse, and subsidence.

Mare ridges (IV-A).- Mare ridges are prominently asymmetric with a steep southwest slope and a gentle southeast slope. They occur in discontinuous, linear to curvilinear segments, 0.5 km wide and many kilometers long, somewhat en echelon, and trending northwestward. Some segments, bounded by linear escarpments, are suggestive of terrestrial fault blocks. The intermontane plain between blocks as shown in map 5 is more heavily cratered than the ridges and apparently less than the surrounding mare.

Mare ridges appear to be the loci of low domical hills of two types, undifferentiated in map 5.

Domes (IV-B).- The first type of domelike hills occurs on ridges, as in the south-central part of the site, where two such hills rise 130 and 60 meters above the general level of the ridge. An elongated dome, possibly made up of two coalescing hills, also occurs on the ridge in the southwestern part of the ridge. The top of this dome appears relatively smooth and flat. High reflectivity is characteristic of these hills; slump terracettes, referred to as "tree-bark" texture, commonly occur on their slopes. The second type of hills mapped as domes occurs on the mare, along the sides or ridges or near their tapering end (map 5).

Mare depressions (IV-G).- Mare depressions are irregular areas below the regional mare level with rounded, ghostlike craters. The surface of the depressions is relatively dark and smooth. It is generally less cratered than the sorrounding mare.

Summary.- Site A-3 is one of the smoothest sites photographed during Mission I, when its roughness is evaluated in terms of crater density and size. The least cratered areas occur in the southwesternmost part of the site, in terrain unit I-A-2, and also on the easternmost ray I-A-R. Photographs of the nonridged mare, west of the site, and detailed analysis of rays with high-resolution photographs were required for further evaluation of these two most promising terrain units.

Two named features within the boundaries of the site A-3 are crater Sabine E and Rima Maskelyne.

## Site A-4

Location.- Site A-4 is in the central highlands area between Mare Tranquillitatis and Sinus Medii. It is covered by Lunar Orbiter I medium-resolution frames 105 to 112. The selenographic coordinates for the corners of the site are:
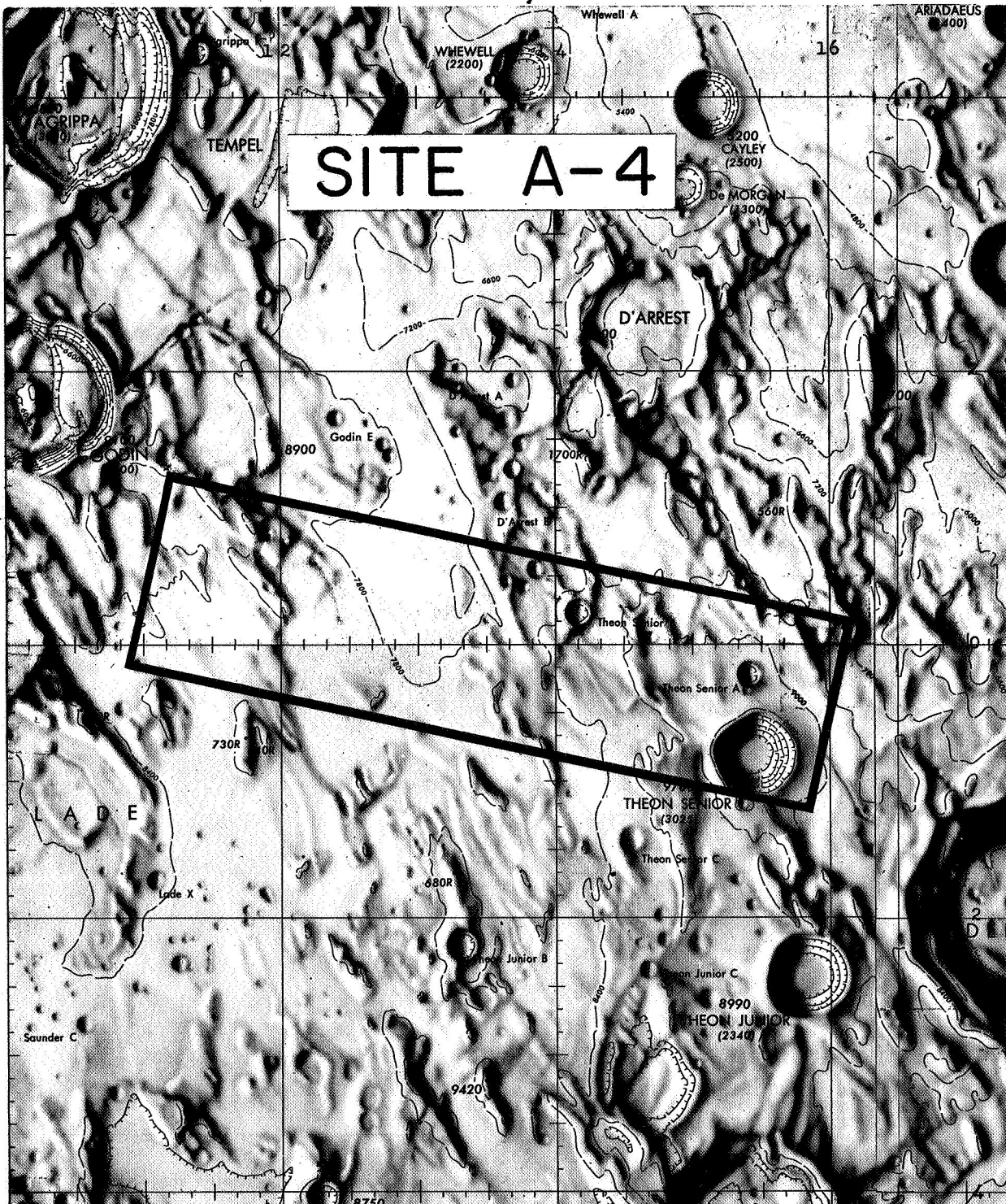
Figure 18.- Index map for site A-4.

|             | Longitude | Latitude  |
|-------------|-----------|-----------|
|             | 11.1° E   | 1.2° N    |
|             | 10.9° E   | 0.1° S    |
|             | 16.1° E   | 0.1° N    |
|             | 15.8° E   | 1.2° S    |

as illustrated in figure 18, the index map for the site.

Preliminary terrain assessment.- Site A-4 was selected to provide representative samples of terra and upland-plains units for assessment as potential areas for Apollo landings (Lawrence C. Rowan, U.S. Geological Survey, 1966). The geologic features shown in map 6, the terrain features shown in map 7, and the explanation of the geologic features are given in the appendix. The geologic terrain analysis was made by Thor N. V. Karlstrom of the U.S. Geological Survey.

Preliminary postflight evaluation indicates that the flattest area in the site, which is largely restricted to medium-resolution frame M-107 (map 6), is underlain by plains-forming material. The plains-forming unit fills a structural trough lying between strongly sculptured uplands with moderate to steep slopes. The surface of the plains-forming material is densely populated by craters ranging in size from a few kilometers to about 20 meters (the limit of photographic average identification resolution). The craters vary appreciably in size, shape, and distribution throughout the unit, and include both bright halo craters and well-formed craters with moderate albedos. Many of the craters with moderate albedo contain conical or domical mounds on their floors. Crater counts (fig. 19) from one of the smoothest appearing areas in the unit indicate a high crater density, appreciably higher than that in smooth mare units. Consistent with the preflight evaluation of the upland-plains units based on telescopic photographs, the higher resolution Lunar Orbiter photography indicates both a higher albedo and a higher crater density than that of average mare.
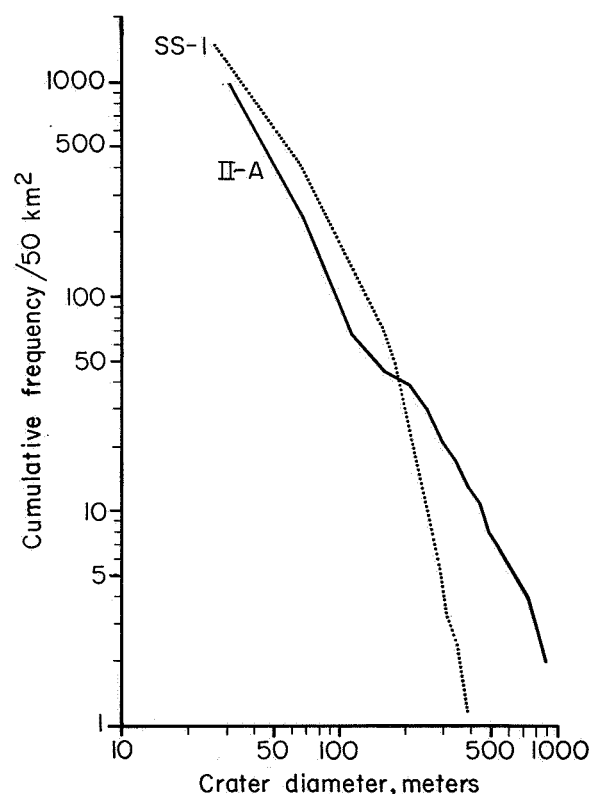


Figure 19.- Cumulative crater-size frequency distribution for sample of upland plains unit (II-A) in site A-4 compared with that for representative dark mare sample (SS-1) in Surveyor I area of site A-9.2.

The craters Theon Senior B and Theon Senior A and Theon Senior are the prominent features located within this site as shown in map 7.

## Site A-5

Location.- Site A-5 is located near the approximate center of the visible face of the moon, and lies in the southwestern portion of Sinus Medii. It is covered by Lunar Orbiter Mission I medium-resolution frames 118 to 133. The selenographic coordinates for the corners of the site are:

| Longitude | Latitude |
|-----------|----------|
| 3.0° W | 1.0° N |
| 0.2° E | 0.3° N |
| 0.1° W | 0.9° S |
| 3.2° W | 0.3° S |

as illustrated in figure 20, the index map for the site. The crater Oppolzer A is the only named feature within the area photographed.

Preliminary terrain assessment.- The site A-5 terrain map (map 8) and the accompanying explanation of geologic features are presented in the appendix. The geologic terrain analysis was made by Lawrence C. Rowan of the U.S. Geological Survey. This site provides an average sample of regional mare. Uplands border the site on the southeast and west and an isolated block of upland trends northwest across the mare in the western part of the site. The mare surface is relatively rough and complicated by the presence of crater fields, irregular depressions, mare ridges, troughs, well-formed craters, and modified, subdued craters. A zone of apparent structural weakness extends northeastward across the site, merging into a large mare ridge. Terrain units of minor extent include linear rills, lineaments, and faults, and a small dome.

Mare (I).- Average regional mare covers about 65 percent of the area. The distribution of craters with differing morphology is variable, so that terrain subdivisions are difficult to delineate. Only one subdivision, unit I-A-2, is presently recognized.

A wide range of roughness is indicated by the cumulative size-frequency distributions (fig. 21) of sample areas 1 and 3 as located in map 8. The most pronounced differences are for craters less than 100 meters in diameter and greater than 200 meters in diameter. Sample 1 has about twice as many craters 50 meters in diameter as sample 3. Samples 2 and 4 are not shown in map 8, but are of intermediate density. Samples 1 and 3 appear, then, to represent end-members of the crater-density spectrum on the regional mare surface at these identification resolutions.

Mare subunit I-A-2 is the smoothest area found in the site. The crater density (fig. 21) is markedly lower than for any other unit. The area of this unit is, unfortunately,
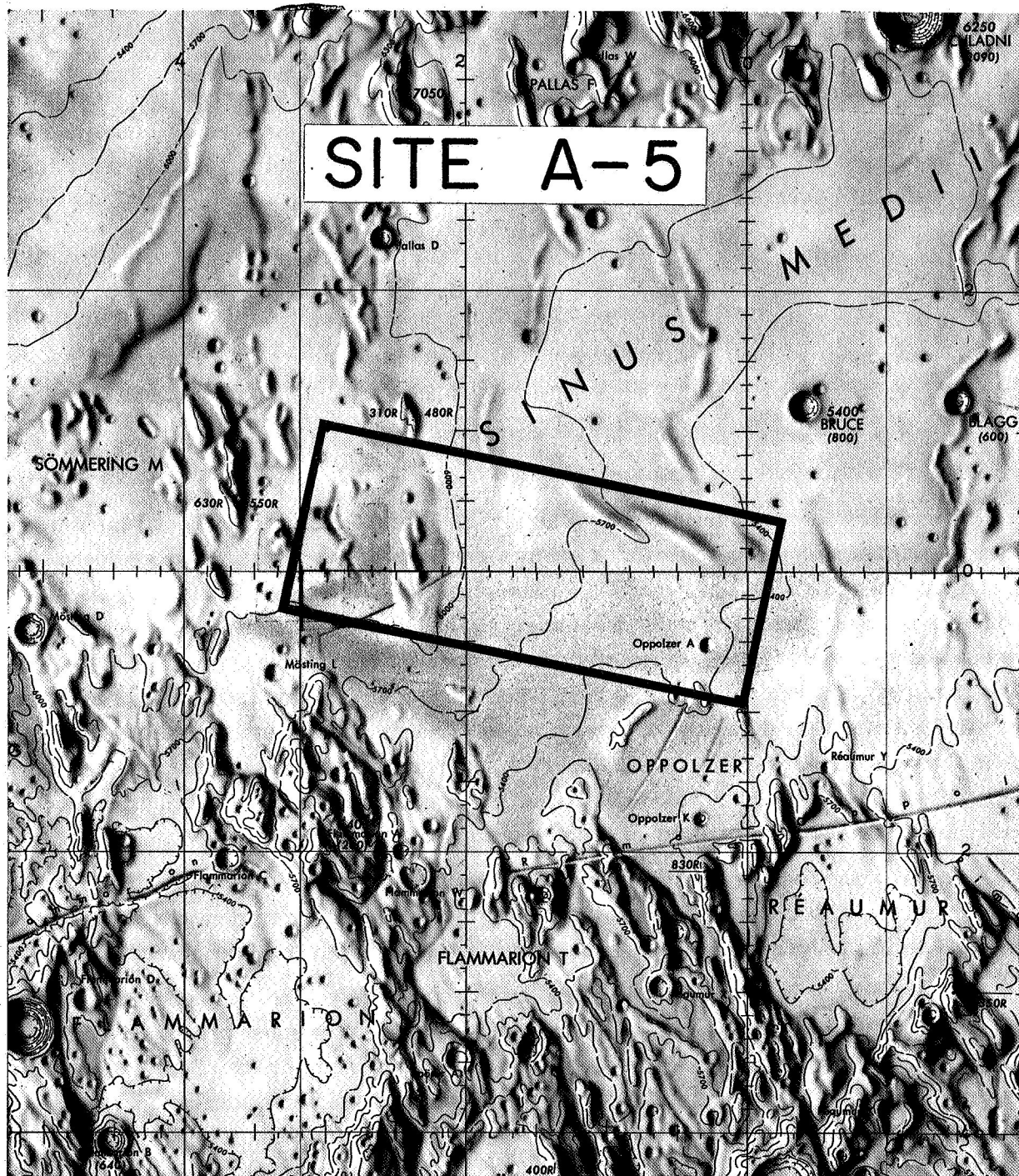
Figure 20.- Index map for site A-5.
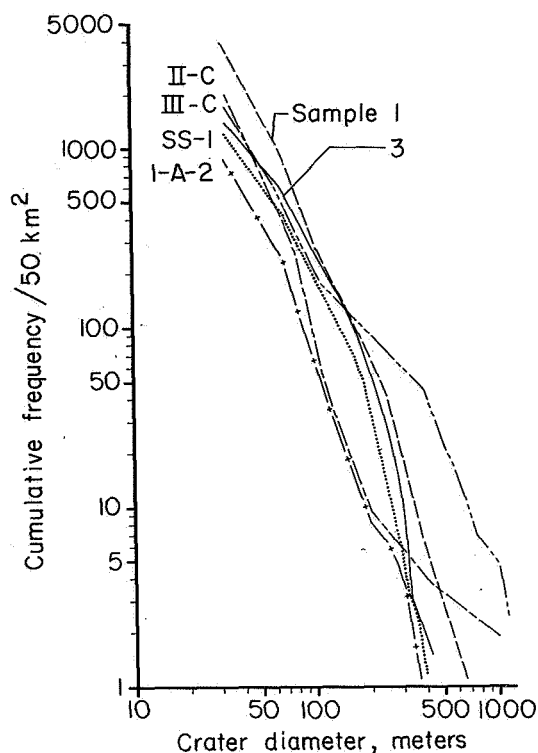
Figure 21.- Cumulative crater-size frequency distributions for samples 1 and 3 and unit I-A-2 in regional mare (I-A), for uplands (II-C), and for crater fields (III-C) in site A-5 compared with that for representative dark mare sample (SS-1) in Surveyor I area of site A-9.2.

relatively small (22 km$^2$) and elongated in the north-south direction.

The relative roughness of samples 1 and 3 appears to be confirmed by slope-component samples of these areas. Statistical relative roughness parameters for sample 3 are: absolute arithmetic mean $\overline{X}_{Ab} \approx 1.0^{\circ}$ and the algebraic standard deviation $\sigma_{Al} \approx 1.2^{\circ}$. In contrast, values for sample 1 are the $\overline{X}_{Ab} \approx 2.5^{\circ}$ and the $\sigma_{Al} \approx 2.6^{\circ}$. Values for unit I-A-2 have not yet been obtained.

Upland (II).- Two main upland terrain units are apparent:

(1) Upland, hummocky and cratered. Hummocky, cratered upland, mapped as II-B, occurs in the west and southwest of the site. One subdivision, II-B-1 (map 8), is apparently a transitional unit between the isolated upland block (II-C) and the surrounding regional mare. This unit is somewhat more subdued than unit II-B.

(2) Upland, sculptured, moderate relief. Terrain mapped as II-C (map 8) is principally an isolated north-northwest-trending block of upland in the western part of the site. It has moderate relief (75 to 150 meters) relative to the surrounding regional mare. The block is sculptured by prominent northeast- and northwest-trending faults and lineaments. Regional slopes, measured in an approximate east-west direction by photogrammetric and photoclinometric techniques, range from 4$^{\circ}$ to 8$^{\circ}$. The topographic profile S-14 shown in figure 22 and located in map 8 was measured photoclinometrically. For 8-meter slope lengths, $\overline{X}_{Ab} \approx 5.0^{\circ}$ and $\sigma_{Al} \approx 6.0^{\circ}$ in this sample. These values suggest that the small-scale roughness of this upland unit is significantly greater than that of the regional mare.

The cumulative size-frequency distribution function for craters in unit II-C is shown in figure 21. Although the density of craters less than 75 meters in diameter is similar to that of the regional mare, there is a marked deficiency of 75- to 500-meter-diameter craters. This feature has been noted in other upland areas and may be due to destruction of craters by mass-wasting.

Crater (III).- Craters are subdivided into two groups, well-formed craters (III-A) and modified, subdued craters (III-B). The character of these two types, as well as

39
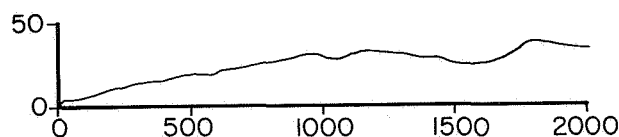
(a) Profile S-14; upland (III-C).
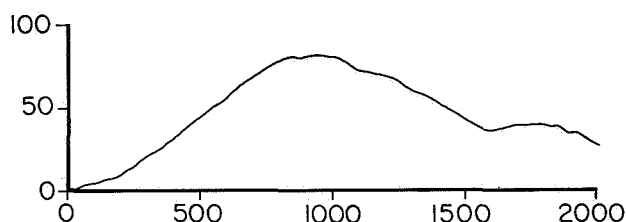


(b) Profile S-18; regional mare (I-A).

Figure 22.- Topographic profiles of areas in site A-5. Measurements in meters; vertical exaggeration approximately ×6. Derived by photoclinometric technique.

descriptions of their component subunits, is given in the geologic terrain map explanation with map 8.

Army Map Service photogrammetrists have compiled numerous topographic profiles across various crater types. Several of these are shown here (figs. 23 and 24) to demonstrate fundamental features. Profiles 15 and 17 represent III-A craters with characteristic moderately steep slopes and raised rims; the latter profile is modified slightly by a slump block on the west side. Craters III-B (profile 10) generally have more subdued rims and less steep walls. Well-formed craters with bright rims appear to be randomly distributed across the site. The walls of these craters are characteristically rubbly, terraced, and steep, with blocks and aggregates in the floors. Profiles 3 and 13 represent these features. The photoclinometrically derived profile S-18 in figure 22 shows a low, broad III-B crater with a slightly raised eastern rim. Topographic profile data are especially important for interpreting the engineering properties of the lunar surface material as well as terrain roughness and will be used extensively in future analyses of the prime sites.

Crater fields are widely distributed and contribute greatly to the roughness. The component craters are usually somewhat subdued. They vary in size from field to field, but generally have constant diameters within a field. The cumulative size-frequency distribution representing unit III-C (fig. 21) shows that the individual craters are generally large (> 100 meters in diameter). This unit is commonly transitional into irregular depressions and troughs.

Structural features (IV).- Most prominent among the linear or curvilinear structural features is the large mare ridge extending across the north-central part of the site. It appears to be highly fractured and faulted and, to the southwest, merges with a fractured zone. This same zone may displace the upland block in the west.

Faults, lineaments, and rills trend predominately northeast and north, coinciding with the fundamental "lunar grid" trends. Chain craters are commonly alined north-south or form loops.

40
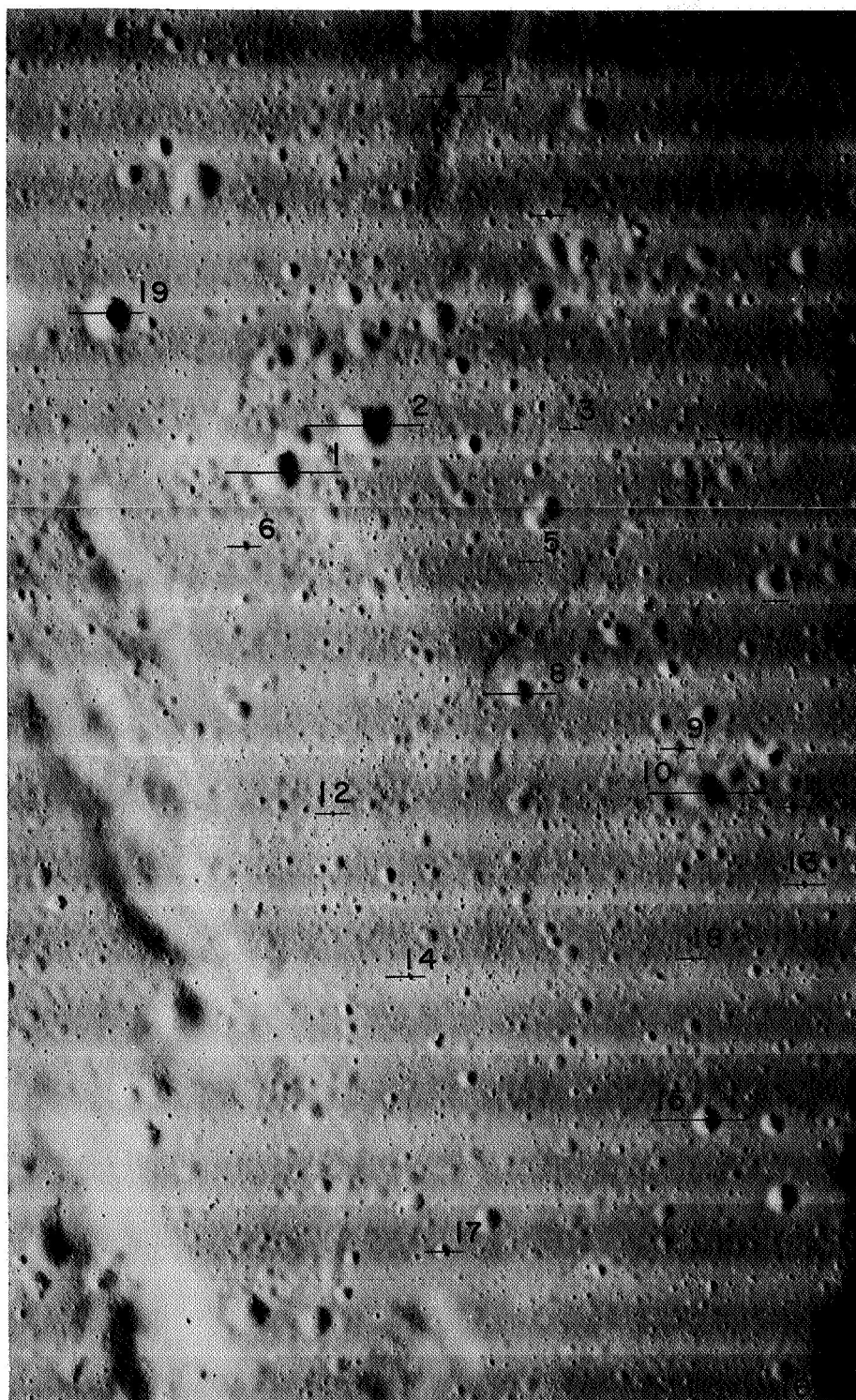
Figure 23.- Location of site A-5 profiles shown in figure 24.
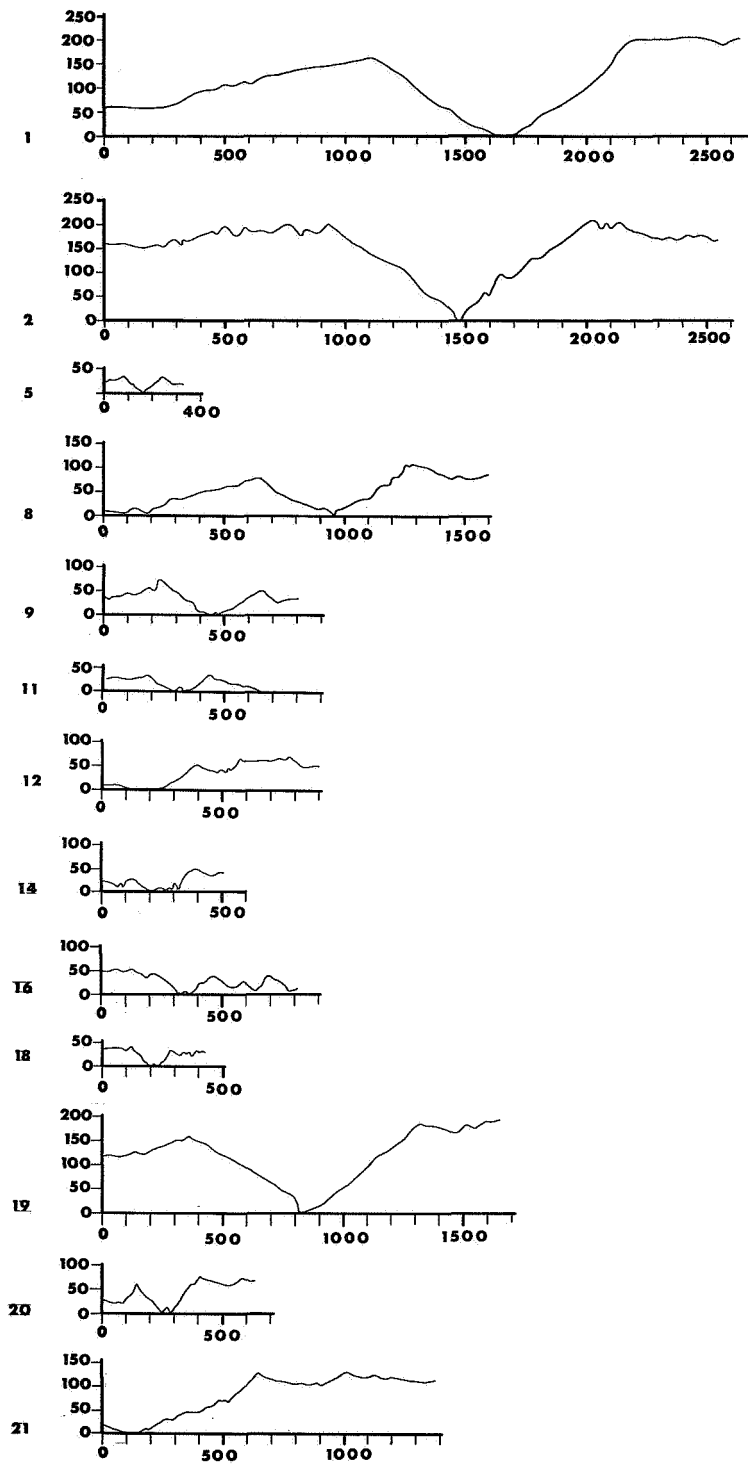
Figure 24.- Topographic profiles of craters in site A-5. Locations shown in figure 23. Measurements in meters; vertical exaggeration ×2. Photogrammetrically derived on stereocomparator by Cleveland Lanham and Thomas Tuel, Army Map Service.
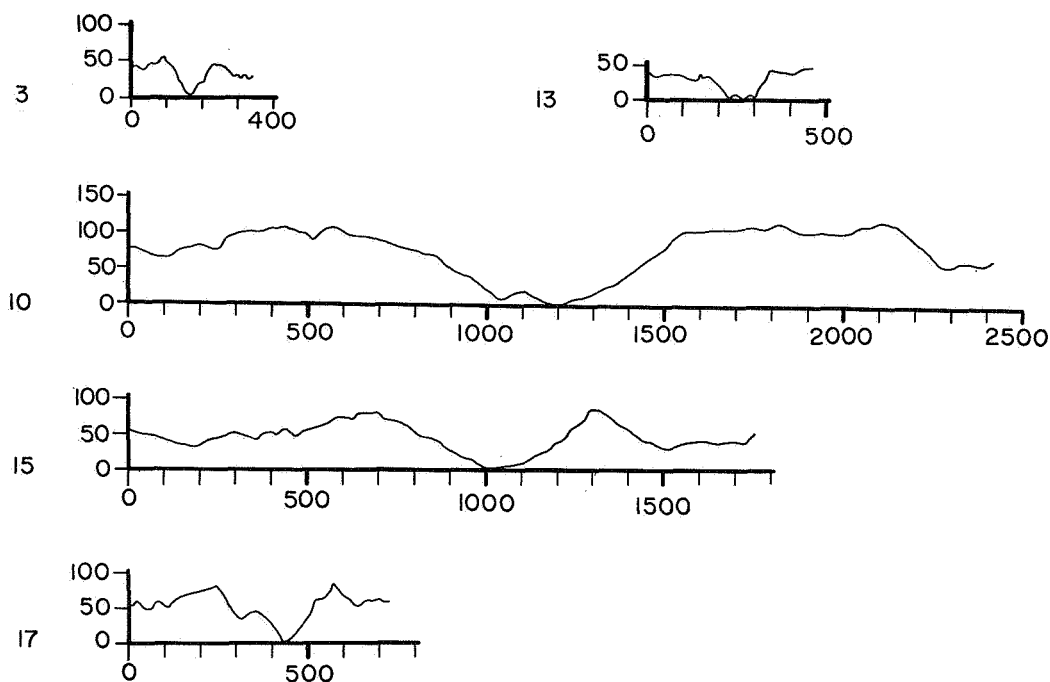
Figure 24.- Concluded.

Telescopic observations indicate that this site consists, for the most part, of low ridges and hills (Dahlem, 1966). Open areas between ridges appear as broad plains containing a few scattered craterlets; and, there is little observational evidence of extensive cratering, whereas the Lunar Orbiter I photography reveals many additional terrain features including numerous craters much smaller than the 1/2-km-diameter limit imposed by earth-based observation.

## Site A-6

Location.- Site A-6 lies within the northern sector of the central continental highlands and includes portions of the Flammarion and Spörer highland basins. It is covered by Lunar Orbiter I medium-resolution frames 141 to 148. The selenographic coordinates for the corners of the site are:

| Longitude | Latitude |
|-----------|----------|
| 4.5° W | 2.8° S |
| 4.7° W | 4.0° S |
| 0.5° E | 3.7° S |
| 0.3° E | 5.1° S |

as illustrated in figure 25, the index map for the site.
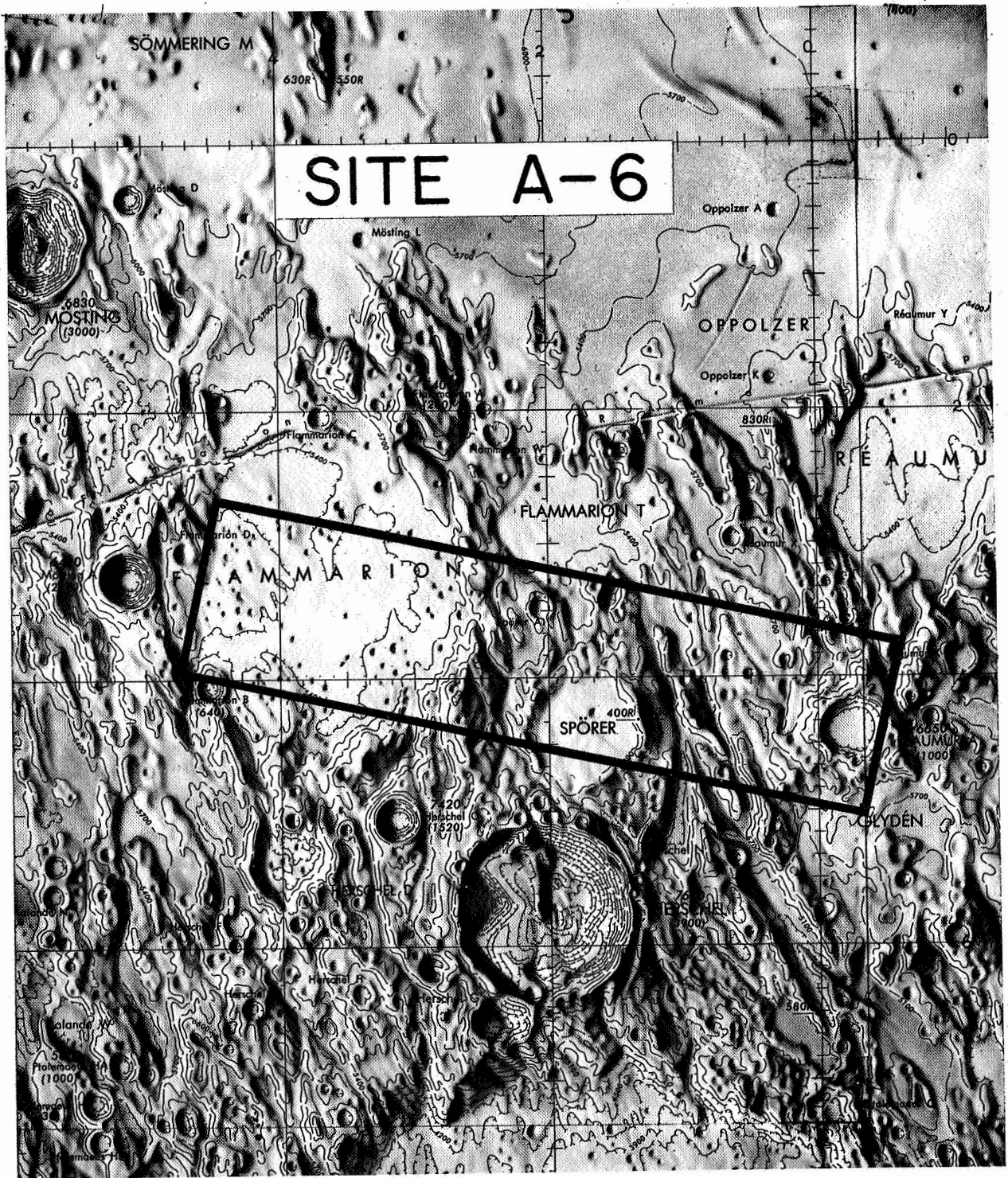
Figure 25.- Index map for site A-6.

Preliminary terrain assessment.- The quality of photography did not permit terrain assessment to the degree desired for site A-6. The high sun elevation degraded the detail of lunar terrain features as shown in map 9, which can only be used as a qualitative guide for overall assessment. Enhanced photographs will make a better analysis possible.

Included within site A-6 are the crater Spörer A at upper center, a major portion of the Flammarion basin in the northwest, and Réaumur A in the east. The northern half of Spörer and a small portion of Flammarion B also lie within the site.

Earth-based observers have described a portion of the Flammarion floor as containing a low ridge, dropping into a shallow basin, with numerous shallow depressions alined with the ridge. These earth-based observations generally describe the area as seen in the Lunar Orbiter photography. The Lunar Orbiter medium-resolution photography reveals more depressions and craters, ranging downward in size from those depicted in the charts to features at the limit of the resolution of the photography. These depressions join and overlap to give the surface a hummocky texture. This texture is more extreme and noticeable to the east of the ridge described but still exists to a lesser degree in the area evaluated for possible landings. However, the high sun elevation at the time of the site photography (35°) makes it difficult to estimate relative smoothness. Many depressions and craters throughout this area are barely discernible.

## Site A-7

Location.- Site A-7 is located in the lowland-mare area between Lansberg and Fra Mauro craters. It is covered by Lunar Orbiter I medium-resolution frames 157 to 172. The selenographic coordinates for the corners of the site are:

| Longitude | Latitude |
|-----------|----------|
| 23.6° W | 2.4° S |
| 23.9° W | 3.8° S |
| 20.4° W | 3.0° S |
| 20.6° W | 4.5° S |

as illustrated in figure 26, the index map for the site.

Preliminary terrain assessment.- The site A-7 terrain map (map 10) and the explanation of the geologic features are given in the appendix. The geologic terrain analysis was made by Richard E. Eggleton of the U.S. Geological Survey. The area shown contains about 92 percent regional mare and 5 percent terra. The largest well-formed crater in the site, Fra Mauro B, mapped as unit III-A, occupies about 3 percent of the total area. The mare surface is abundantly cratered, and the craters are 1.7 km or less in
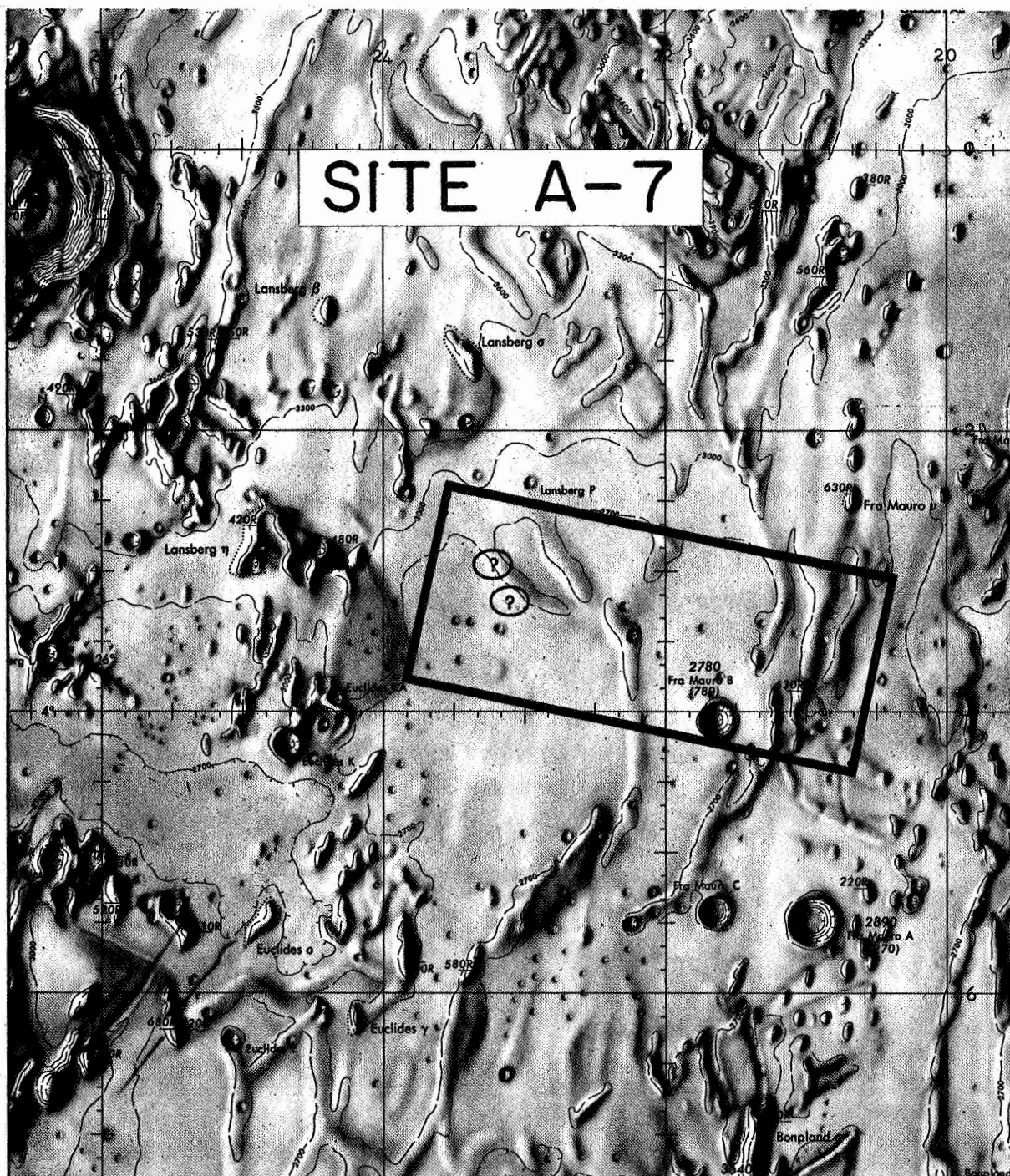
Figure 26.- Index map for site A-7.

crest-to-crest diameter. Several rays, which in full-moon photographs appear as broad, light-colored streaks, cross the site. Some ridges rise above the surface of the mare in the eastern third of the site. The sun elevation above the horizon at this site exceeded 30° and resulted in the inability to detect craters less than 26 to 30 km in diameter. The density extremes indicating excessive light intensity are shown graphically in the upper curve of figure 27, wherein nearly all the photometric density trace is above the range of the preexposed gray scale on the film-edge data. For the purpose of analysis of photography of this site, the crater counts were made on prints of medium-resolution frames which had been assembled from film made at a high-gain setting on the GRE as noted previously.

The geology of the site and an extensive surrounding area has been mapped previously by Richard E. Eggleton, U.S. Geological Survey, 1965. A preflight site-evaluation report by West (1966) includes significant quantitative treatment of relative full-moon albedo and of terrain roughness parameters.
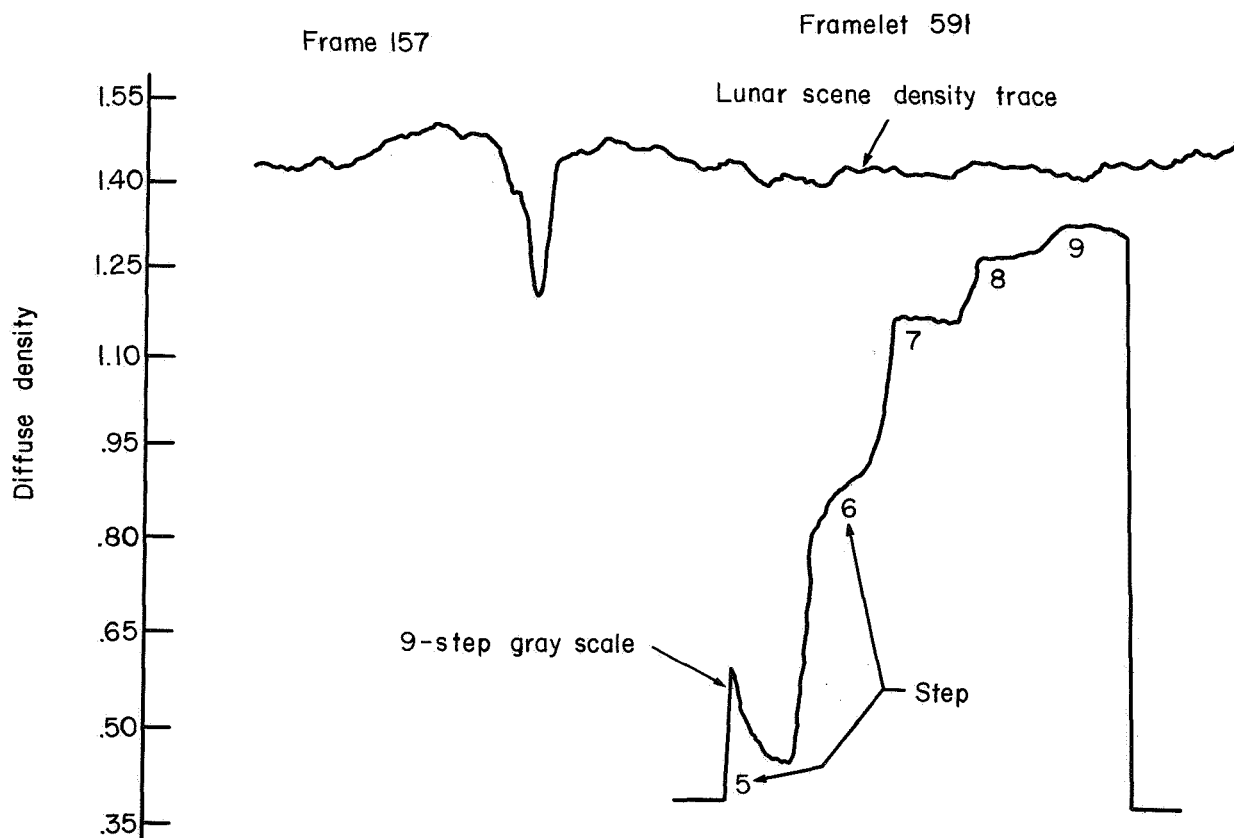


Figure 27.- Photometric density trace for site A-7.

Mare, undifferentiated (I-A).- Topographically, the surface of the regional mare is characterized by variations in both density and size of craters. Earth-based and Ranger photographs have shown that isolated circular craters larger than about 0.75 km in diameter are randomly distributed over the mare surface. Isolated craters of approximately this diameter and crater fields are excluded from the mare terrain units.

The regional mare in this site is subdivided into four main units: I-A, I-A-4, I-A-6, and I-A-7. Terrain units I-A-2, I-A-3, and I-A-5 are transitional. Terrain roughness in the seven units is expressed in terms of crater density per unit area, decreasing from unit I-A-1 to unit I-A-7.

Crater counts shown in the cumulative frequency curve of figure 28 show that unit I-A-4 in this site has a crater density of about 500 craters (with a diameter of 60 meters) per 50 km$^2$.

Terrain unit I-A-1 is characterized by an abundance of craters, from 0.25 to 0.5 km in diameter. Terrain units I-A-2 and I-A-3 are generally less cratered and they lack craters in the diameter range of the larger craters of unit I-A-1. The fourth mare terrain unit, I-A-4, is markedly less cratered than the first three mare units, as is unit I-A-5. Terrain unit I-A-6 is essentially coextensive with light-colored streaks observed in earth-based lunar photographs at 1-km resolution. Mare surface that appears thickly mantled with ray material is labeled III-E. Terrain unit I-A-7 is a small, nearly craterless area, measuring about 2 by 4 km, about 17 km west of the northeast corner of the site; associated with it are low, dome-shaped hills.

Upland (II).- The upland is restricted to the eastern quarter of this site. It is covered by craters 0.25 to 1.5 km in diameter. The upland is subdivided into three units of increasing local relief: II-B, II-C, and II-C$_1$, as shown in the explanation with map 10.

Craters (III).- Individual craters and crater components have been mapped only where they might constitute a terrain hazard to lunar landing and surface operations.
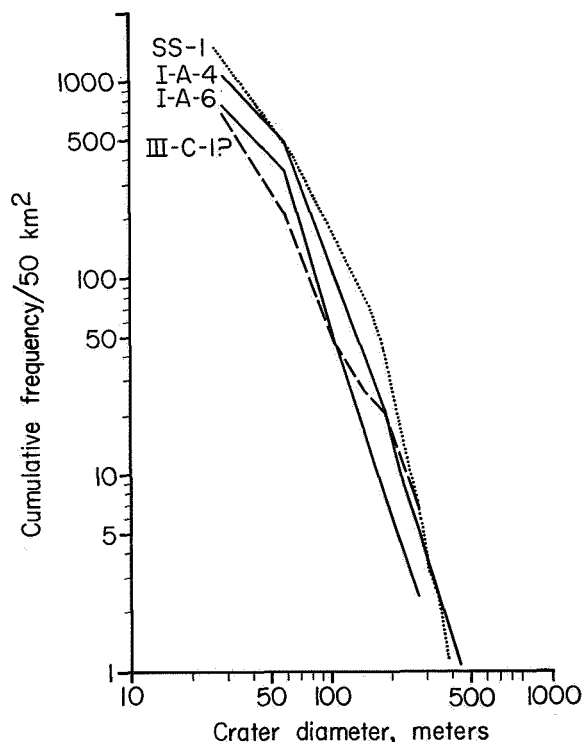


Figure 28.- Cumulative crater size-frequency distributions for areas in site A-7 compared with that for representative dark mare sample (SS-1) in Surveyor I area of site A-9.2.

48

Craters fall within two broad categories: well-formed craters and modified craters, generally of subdued form. Craters with convex-upward interior walls, or dimple craters, are a special kind of well-formed craters.

(1) Well-formed craters (III-A). The components of well-formed craters are the interior wall, the floor, the small mounds at the bottoms of craters, and the rim.

The interior wall, which may include part of the floor, is commonly smooth, but may be rough locally. In Fra Mauro B the interior wall is mapped as III-A-1b; it is moderately smooth, but it has "tree-bark" texture, and a low ridge, probably a debris stream trending downslope. The toe of the slope at the bottom of unit III-A-1b in Fra Mauro B is mapped as unit III-A-1b$_1$. It may be analogous to II-C-1.

Terrain unit III-A-3c includes craters with bright halos and rays. Such craters are less than 200 meters in diameter. They typically have raised rims with concave-upward profiles. Because of the small size of these craters, the unit includes crater wall and floor also. The rim material of these craters is likely to be blocky.

Another type of well-formed crater, the dimple crater (III-D), is most common in two clusters in the terra in the southeast quarter of the site. Dimple craters have convex-upward interior slopes, suggesting that particulate surficial material may have drained down a hole in the center.

(2) Modified craters (III-B). The components of subdued craters include the interior wall, smooth or rough, a mound at the bottom, and a rim. Commonly, the rim grades into the interior slope in subdued craters.

(3) Crater fields (III-C). The crater fields are subdivided into the two terrain units III-C-1 and III-C-2. Craters that touch or partly overlap each other are referred to as composite craters. As observed on earth-based lunar photographs, composite craters are abundant in the fields of satellitic craters that surround many large lunar craters. Commonly, they lack crater wall and rim in the area of overlap and they occur in groups of 5 to 20 individual craters. This unit exhibits the whole range of crater sizes and depth-to-diameter ratios.

Some craters in the diameter range from 0.15 to 0.4 km have a terrace completely ringing the upper part of the interior wall. These craters occur with an areal density of about 0.6 to 0.7 per km$^2$ and nearly all of them are steep walled above and below the bench. The bench commonly is a well-developed shelf, 5 to 10 meters below the level of the mare immediately surrounding the crater. Such crater walls are mapped as unit III-A-1c. Where the circular shelf is ill defined, the crater wall is mapped as III-A-1c$_1$; where the level of the shelf varies from a few meters to a few tens of meters below the surrounding mare, the crater wall is mapped as III-A-1c$_2$. These terraces may be at the base of a weak surface layer.

The rim of well-formed craters constitutes unit III-A-3. Commonly, the rims of craters larger than 15 km across are hummocky near the rim crest with radial ridges and troughs further out. Unit III-A-3a, the hummocky terrain, is mapped around Fra Mauro B. Another rim unit, III-A-3a$_1$, is located in the upper part of the interior wall of Fra Mauro B. It may represent the outcrop of crater rim material in the crater wall and show the thickness of this unit. The crater lip with steep slope and tree-bark texture is classified as unit III-A-3d.

The outer profile of craters with raised rims varies between two extremes. One is concave upward, with slope of 10° to 15° near the rim crest; the slope along the interior wall is steep, amounting to 30° in Fra Mauro B. The other type is convex upward, gently sloping and typical of shallow craters with relatively low interior slopes. The concave-upward types are classified as modified craters.

Structural features (IV).- Among the positive features in this site are mare ridges (IV-A) and domes (IV-B). They occur principally in the easternmost third of the site.

Mare ridges mostly occur in discontinuous segments, generally 2 to 10 km long, 1 to 0.25 km wide, and alined in a northward direction. These are low, flat-topped, and somewhat sinuous, wandering laterally 1 or 2 km. They occupy only a fraction of the total site area. In the north-central part of the site are two circular mare ridges that apparently overlie buried craters.

A few domes are seen rising above the mare surface. Crater Fra Mauro B is the one named feature included within the boundaries of this photographed area.

## Site A-8.1

Location.- Lunar Orbiter site A-8.1 is in the southeast part of Oceanus Procellarum. It is covered by Lunar Orbiter I medium-resolution frames 176 to 183. The selenographic coordinates for the corners of the site are:

| Longitude | Latitude |
|-----------|----------|
| 37.5° W | 2.1° S |
| 37.8° W | 3.4° S |
| 35.4° W | 2.5° S |
| 35.7° W | 3.9° S |

as illustrated in figure 29, the index map for the site.

Preliminary terrain assessment.- The terrain map of site A-8.1 (map 11) and the accompanying geologic explanation is given in the appendix. The geologic terrain analysis was made by David Cummings of the U.S. Geological Survey. The cratered mare in the vicinity of this site is partly covered by ray material from the crater Kepler and possibly Copernicus. This evaluation is based on analysis of only one Lunar Orbiter photograph
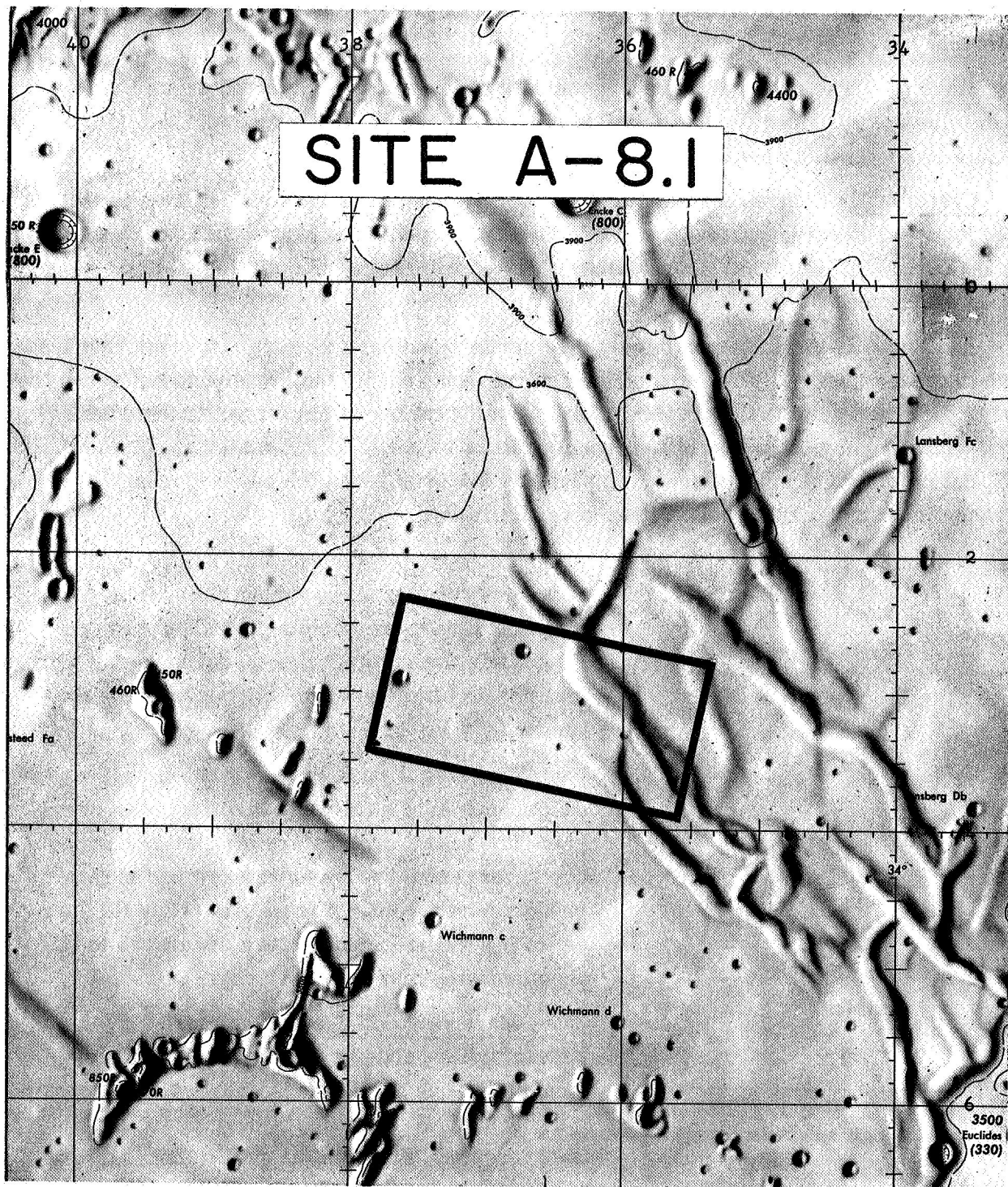
Figure 29.- Index map for site A-8.1.

(frame M-183) which covers a sample of the cratered regional mare, including well-developed mare ridge. Previous work at this site is given by David Cummings (U.S. Geological Survey, 1966).

Mare (I).- The regional mare is generally of low albedo. Selected areas have crater-size distributions (fig. 30) similar to those of the dark mare sample (SS-1) from site A-9.2, suggesting comparable surface roughness.

Craters (III).- Three main categories of well-formed craters are present in the site: funnel craters; concave-floored craters; and flat-floored craters. The funnel craters include undifferentiated floors with one or more craters, smooth floors, and floors with central peaks.

The funnel craters are seemingly the youngest and have a sharp rim crest that rises above the mare surface. The tops of the central peaks within the craters do not reach the level of the mare outside the craters. Some small craters within larger craters have slightly raised rims. Several of the funnel craters have bright ray material outside the rims, but no blocks could be seen within the ray material or on the outer slopes. Terrace-like forms can be seen within several craters.
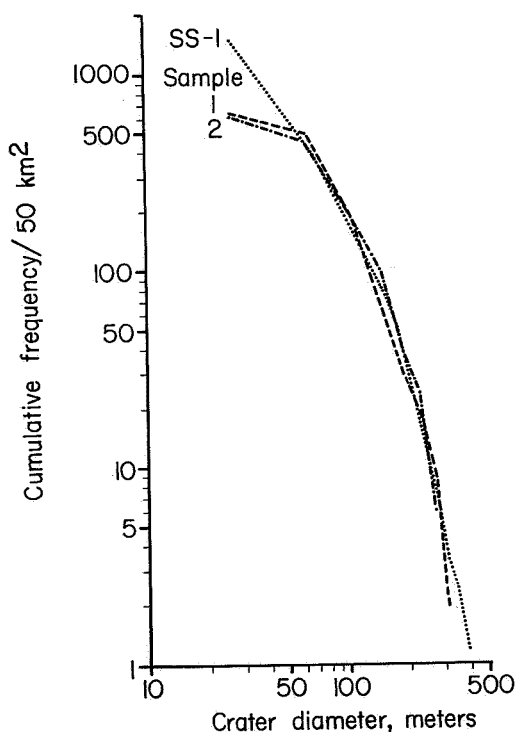


Figure 30.- Cumulative crater size-frequency distributions for samples of mare unit in site A-8.1 compared with that for representative dark mare sample (SS-1) in Surveyor I area of site A-9.2.

The concave-floored and flat-floored craters have rounded and subdued rims. Some flat-floored craters are seemingly without rims. Craters in these categories do not have ray material nor do terraces obviously occur in the crater walls.

The gradation of crater morphology suggests differences in age rather than differences in origin. The funnel craters are similar in morphology to terrestrial volcanic craters and may be predominantly volcanic in origin. Only the largest of the well-formed craters are shown in the accompanying map (map 11).

Mare ridges (IV-A).- The mare ridges appear to be bounded by either one steep slope (scarp) and one gentle slope or two steep slopes (map 11). The steep slopes have up to four distinct terraces, whereas the gentle slopes do not have terraces, but grade into the adjoining mare.

The ridges have central depressions. The floor of the depression is topographically higher

than the surrounding mare. The floor is slightly concave upward; some flat areas occur but distinct convexity was detected. Craters of all categories and age can be seen within the depressions and on the outer sides. There does not seem to be any difference in crater density between the ridges and the mare.

Very few lineaments were observed. The terraces may reflect structural control, but no definite pattern of control can be discerned.

Although the mare ridges are discontinuous and sinuous, a northwest trend is apparent. The wrinkle ridges are parallel to one another. The two major ridges appear to have a structural continuity even though they are separated by mare. The sinuosity of these ridges, in plan view, is approximately symmetrical about northeast-southwest axes. The pattern of the ridges may be an expression of the "lunar grid" system. A tectonic origin of the ridges without any evident magmatic intrusion seems probable.

In summary, the photography of this site indicates that the regional mare unit is comparable in roughness to mare in other sites, and crater distributions in the smoothest appearing areas are essentially similar to these of the dark mare regions in site A-9.2.

## Site A-9.2

Location.- Site A-9.2 is located about 60 km north of the crater Flamsteed and about 330 km southwest of crater Kepler. Site A-9.2a is covered by Lunar Orbiter I medium-resolution frames 184 to 199, and site A-9.2b is covered by medium-resolution frames 200 to 215. These sites were photographed on successive orbits and the photography not only has a high percentage of forward overlap but also a high percentage of side lap. The selenographic coordinates for the corners of site A-9.2a are as follows:

| Longitude | Latitude |
|-----------|----------|
| 44.9° W | 1.0° S |
| 45.2° W | 2.2° S |
| 41.9° W | 1.7° S |
| 42.2° W | 2.9° S |

and of site A-9.2b are as follows:

| Longitude | Latitude |
|-----------|----------|
| 44.9° W | 1.4° S |
| 45.2° W | 2.7° S |
| 41.9° W | 2.1° S |
| 42.2° W | 3.3° S |

The location of the site is shown in figure 31.
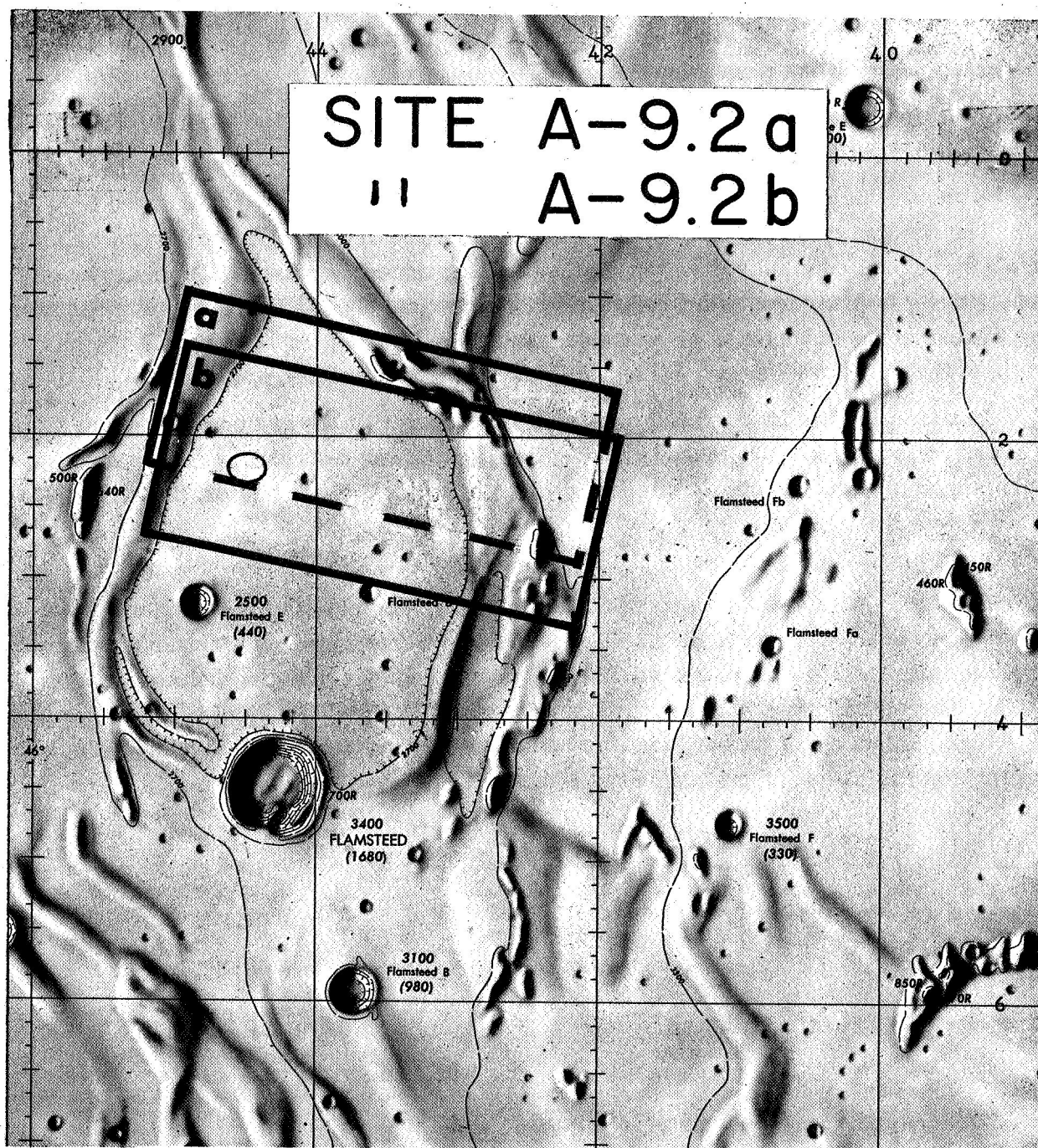
Figure 31.- Index map for site A-9.2.

Preliminary terrain assessment.- Site A-9.2 includes the northeastern part of an incomplete, partly buried, old crater with an outer diameter of about 100 km and dark mare within it, on which Surveyor I landed. The smooth-appearing regional dark mare was selected as a potential Apollo landing site by preflight topographic, geologic, and terrain evaluation (McCauley, 1966). The successful landing of Surveyor I on the mare surface provides an invaluable sample of small-scale surface roughness and bearing strength of dark mare materials.

A geologic description of this site and its subdivision into geologic terrain units (map 12) are in the appendix. The geologic terrain analysis was made by Thor N. V. Karlstrom of the U.S. Geological Survey.

Mare (I).- Dark mare occupies part of the interior of the modified crater (III-B) and occurs outside the crater rim with similar character in both occurrences. On the west, the dark mare grades into mare with grossly comparable surface character but with higher albedo and generally higher density in large craters and in small craters. The dark mare extends to the eastern margin of the site and is interrupted by elongate upland ridges or remnants of the partly buried old crater rim which rise as much as 600 meters or more above the surrounding mare surface.
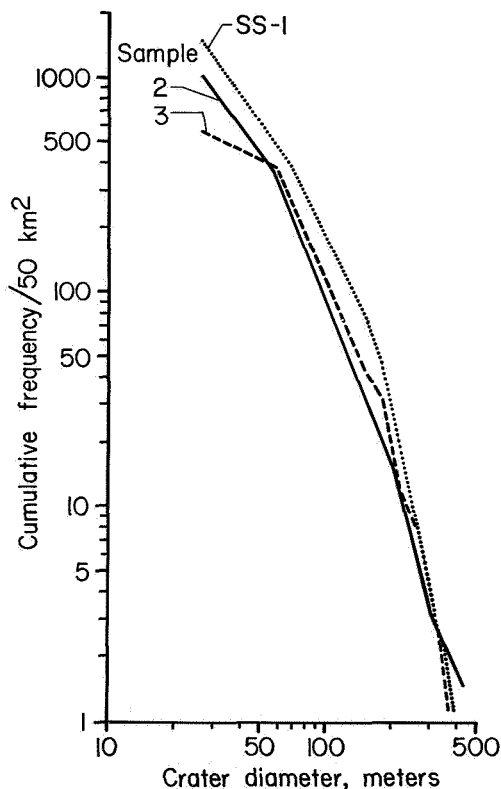


Figure 32.- Cumulative crater size-frequency distributions for samples of dark mare (unit I-B) in site A-9.2 compared with that for representative dark mare sample (SS-1) in Surveyor I area of site A-9.2.

The dark mare, though comparatively smooth in appearance, is densely cratered and characterized by abrupt variations in the distribution of craters of differing sizes and shapes. Diameters of nearly 500 craters range from the approximate lower limit of resolution (about 10 meters) to more than 14 km (crater Flamsteed D). Most resolvable craters are less than 50 meters in diameter. Crater depths range from less than 1 meter to more than 2 km. Diameter-to-depth ratios range from 0.01 to 0.63, reflecting great variation in crater shapes. Crater slopes range from less than 1° to more than 36°. Cumulative frequency curves of crater size in representative areas of the map unit are shown in figure 32.

Although relief on the dark mare is largely a function of cratering, other topographic features contribute to gross surface roughness. Mare ridges are measured to be a few meters to 100 meters high. Photogrammetrically

55

measured profiles of mare and modified crater ridges suggest that the mare surface is not as flat as it appears to be in monoscopic photographs but that it has appreciable local relief and gross irregular slopes between craters (fig. 33, profiles A, B, and C).

Analyzed in terms of smallest resolvable roughness characteristics, the dark mare is made up of a mosaic of small darker circular, elliptical, or linear zones with low crater density within more densely cratered areas. Except in localized areas, lineaments indicating fractures, rows of craters, ridges, and depressions, at or just below resolution, suggest that ground roughness generally is greater than 1 meter throughout the unit. The ground texture pattern in the Surveyor I site (see map 12) is similar in character to patterns for other representative areas in the dark mare unit, suggesting an appreciable degree of material homogeneity and a roughly comparable degree of small-scale roughness throughout most of the unit. Large blocks evident in or on crater walls and rims
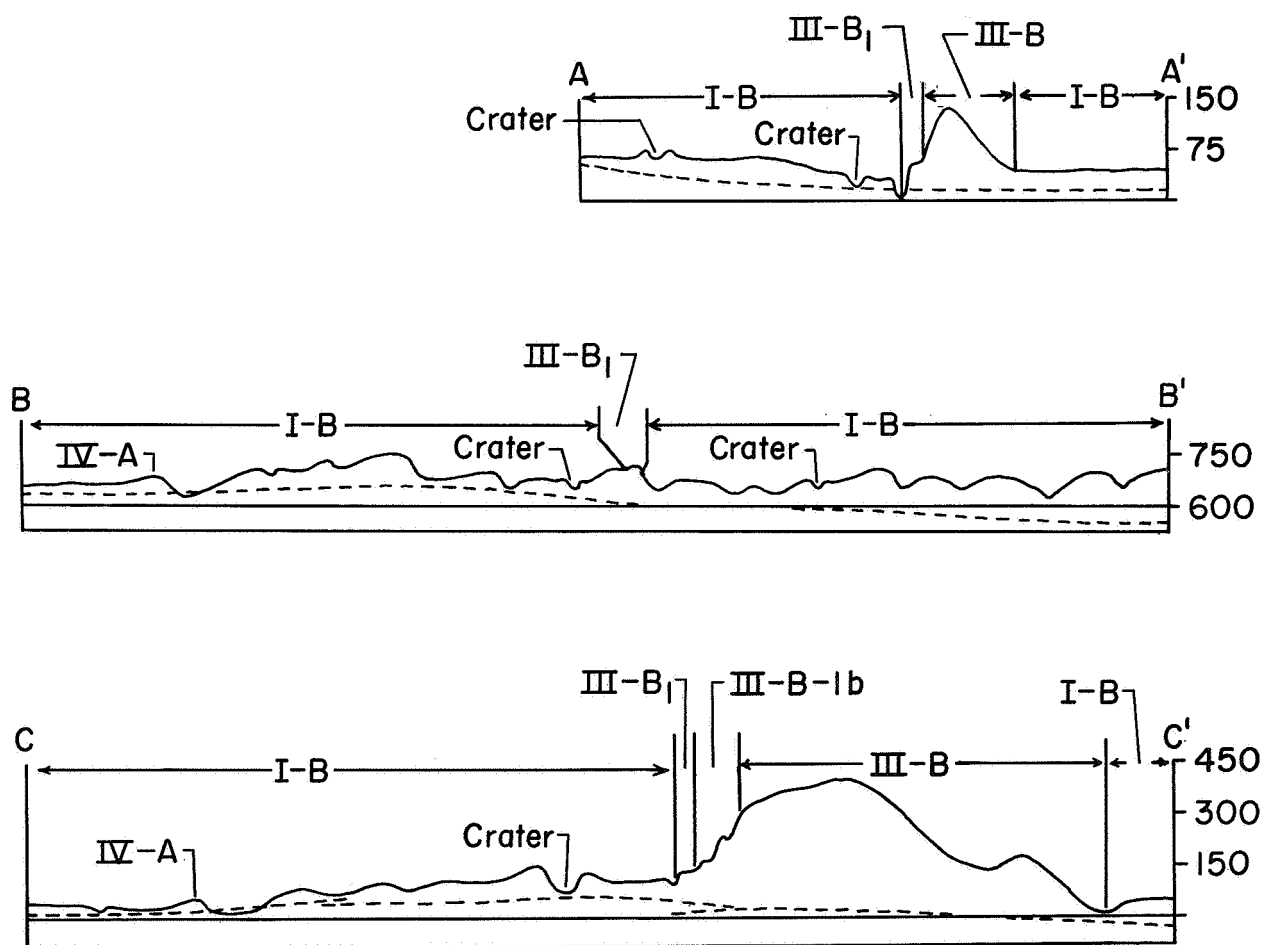
Figure 33.- Topographic profiles of mare and old crater ridges in site A-9.2. Heights in meters; vertical exaggeration ×10. Dash line indicates uncorrected apparent datum-plane warping. Derived photogrammetrically on ER-55 plotter by Gary Nakata, U.S. Geological Survey.

suggest that the depth to coherent bedrock beneath unconsolidated materials is relatively shallow in some localities.

Units I-A-1 (rough-rayed mare) and I-A-2 (smooth-rayed mare) are distinguished from dark mare largely by their somewhat higher albedo. The boundary between the dark mare and the smoother unit is, however, irregular and gradational and is difficult to locate in Lunar Orbiter photography. The crater count of a representative area in unit I-A-2 (fig. 34, area 4) is distinctly different from the dark mare samples, with a greater total crater density and smaller number of larger craters. The crater sample taken from the transition zone between dark and rayed mare (fig. 34, area 5) reflects the gradational character of the contact in the site and is more similar to the dark mare samples.

Crater (III).- The remnants of the old crater structure include isolated ridges with slopes ranging from gentle to steep. The steeper wall slopes are delineated as III-B-1 and show intersecting lines that may be fractures, suggesting that coherent bedrock lies at or close to the surface. Boulder streams, with blocks as much as 30 meters high, are locally traceable upslope to what appear to be steep, even, overhanging, exposed bedrock ledges. The upland slopes are apparently less cratered than the lower mare surfaces (figs. 32, 34, and 35), suggesting progressive destruction of craters by downslope migration of comminuted surficial materials.

Strong lineament patterns on the old crater slopes parallel those in the surrounding mare. This similarity in trends suggests direct control by basement rock fractures of lineament development. Azimuth frequency samples of mare and old crater rim lineaments show strong preferred north, northeast, and northwest orientations essentially those of the lunar grid.

Mare craters have been discussed as a parameter of gross surface roughness in unit I-B. The sculptured crater-rim ridges constitute the major topographic approach hazard in the site for Apollo landings. The larger craters are designated on the map as units III-A-1, III-A-3, and III-A-3c. Photogrammetrically derived profiles
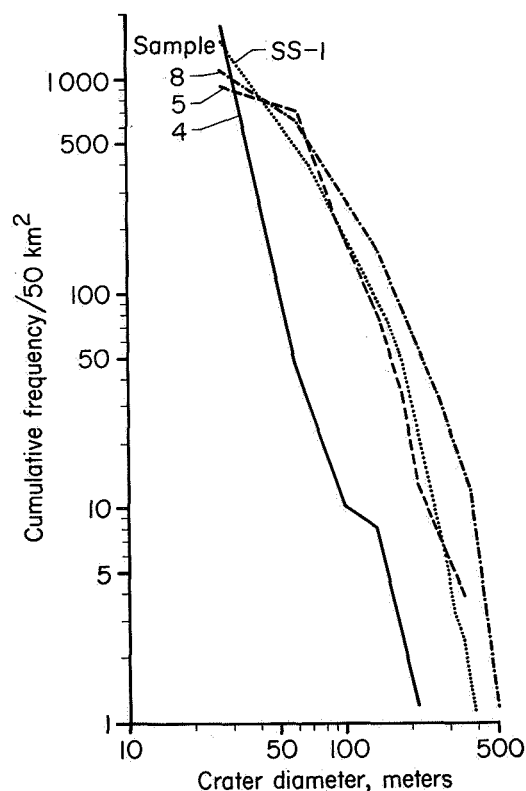


Figure 34.- Cumulative crater size-frequency distributions for samples of rayed mare in site A-9.2 compared with that for representative dark mare sample (SS-1) in Surveyor I area of site A-9.2.

57

SS-I

1000
500

Sample
6
7

100

50

Cumulative frequency/50 km$^2$

10

5

1

10    50  100        500

Crater diameter, meters
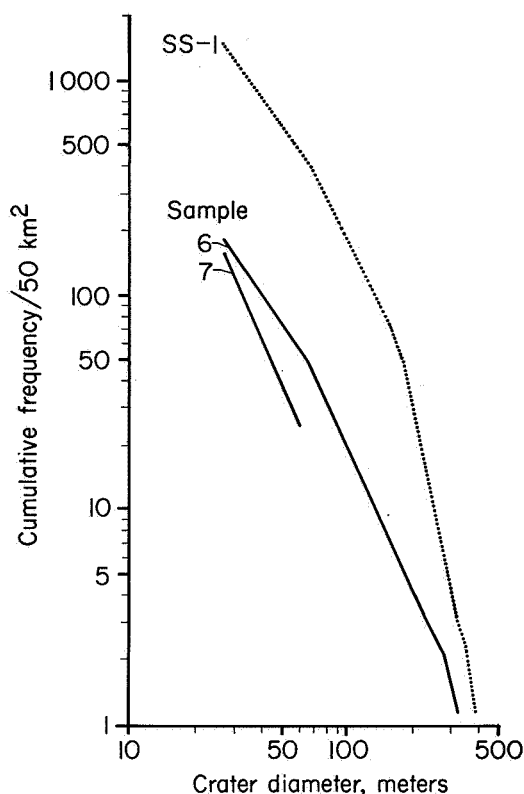
Figure 35.- Cumulative crater size-frequency distributions for sample areas representing old crater rim slopes in site A-9.2 compared with that for representative dark mare sample (SS-1) in Surveyor I area of site A-9.2.

of the craters identified in figure 36 illustrate variability in crater forms within the site (fig. 37).

Marginal ridges or terraces at the base of the deformed crater comprise one of the most interesting geologic features in the site. Their position at the base of steep slopes suggests colluvial deposits resulting from mass-wasting of upper slopes. On the other hand, there is uniform development at the base of both gentle and steep slopes; ridges are present in areas of no slopes; and the ridges, although in general positioned above the mare, are separated from it by a marginal trench (fig. 33, profiles A, B, and C). These latter characteristics seem more consistent with a structural origin and suggest that the marginal terraces may represent marginal facies of the original mare fall, left perched along basin margins by differential subsidence during compaction of solidification of the mare material following extrusion.

The homogeneity of the ground textural patterns within the dark mare unit strongly suggests that the bearing-strength data obtained from the Surveyor I site (350 grams/cm$^2$) hold generally throughout the dark mare unit. The differences between the dark mare and the smoother rayed mare unit, which has slightly higher surface reflectivity and greater density of smaller craters, are small. These differences being small suggests that the bearing strength of the ground in the rayed mare areas is closely comparable to that in the dark mare areas. Earth-based photography shows this area to be relatively smooth with a low density of craters. Lunar Orbiter photographs show the lunar surface in the general region of Surveyor to be relatively flat with a high density of craters and with large blocks visible only on some escarpments that slope away from the sun. The terrain within 1 to 2 km surrounding the landed Surveyor appears as a gently rolling surface studded with craters ranging in diameter from a few centimeters to several hundred meters. The lunar surface was also shown to be littered with coarse blocks and fragments which are not evident from either earth-based or Lunar Orbiter photography.

Figure 36.- Location of site A-9.2 profiles shown in figure 37.
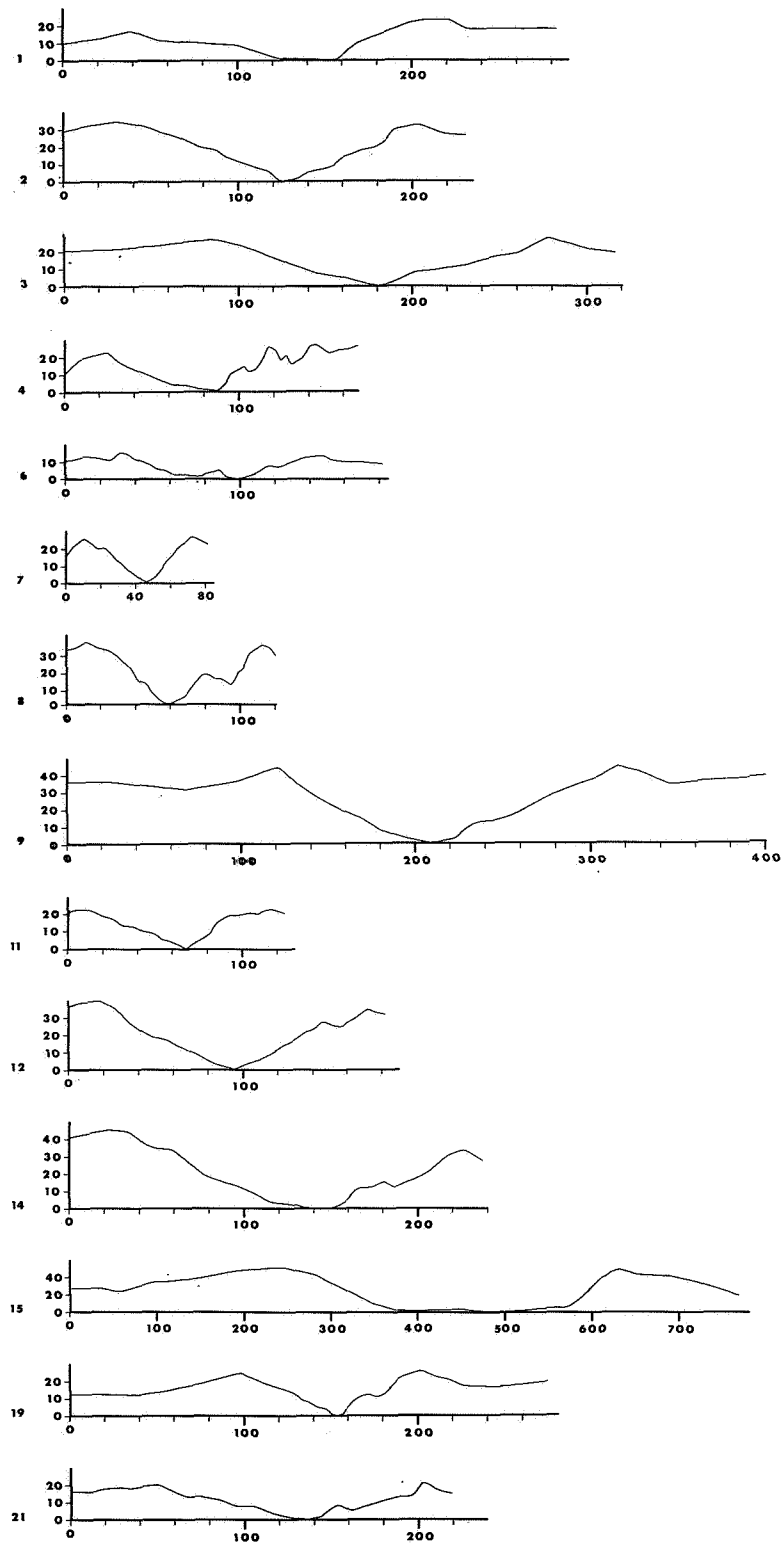
Figure 37.- Topographic profiles of craters in site A-9.2. Locations shown in figure 36. Measurements in meters; no vertical exaggeration. Photogrammetrically derived on stereocomparator by Cleveland Lanham and Thomas Tuel, Army Map Service.

# RANKING OF SITES IN ORDER OF RELATIVE ROUGHNESS

On the basis of preliminary geologic terrain maps, crater-density data, and photogrammetric and photoclinometric measurements on the Lunar Orbiter I prime-site photography, a ranking of sites as a function of relative roughness is presented in the following table:

| Site | Principal terrain units in order of increasing relative roughness | Terrain unit description |
|---|---|---|
| A-9.2 | I-B | Low crater density and albedo; widely distributed moderate number of blocks |
| A-3 | I-A-2 | Low crater density, primarily in western part of site |
| A-3 | I-A-R | Theophilus ray material in eastern part of site; low crater density, subdued subjacent topography, high albedo |
| A-1 | I-A | Low crater density |
| A-7 | I-A-6 | Low crater density, subdued topography, moderately high albedo; generally confined to small areas in west-central part of site |
| A-8.1 | I-A | Moderate crater density |
| A-7 | I-A-4 | Moderate crater density; more widely distributed than unit I-A-6 |
| A-5 | I-A | Highly variable crater density, but usually moderate to high; a few small, smooth areas (I-A-2) |
| A-6 | III-B-3 | Moderate crater density, undulating topography with high frequency of craters > 200 meters in diameter |
| A-4 | II-A | High frequency of 200- to 900-meter-diameter crater, moderate frequency of craters > 200 meters in diameter |
| A-2 | II-C, II-D | High slopes; crater density indeterminate |

# COMMENTARY ON LUNAR TERRAIN FEATURES

## SHOWN IN SELECTED PHOTOGRAPHS

### INTRODUCTION

A few medium-resolution frames have been selected of each of the prime sites photographed (figs. 38 to 46) to illustrate the varied terrain types and geologic features more clearly than may be evident from the information given in the previous sections on terrain evaluation. In addition, scenes are selected (figs. 47 to 56) from the photographs which were taken as film-set frames during the course of the mission. Though not related to the prime sites, they contain much of geologic interest of both the near and the far sides of the moon.

These photographs are arranged so that the direction of north is to the top of the page and the spacecraft is flying in orbit from left to right. Sunlight is coming from the right in near-side photographs and from left in far-side photographs.

It should be noted that the photographs are made up of reassembled strips of trimmed 35-mm film obtained from the Ground Reconstruction Equipment which reproduces the electronically scanned film in the spacecraft. Because these particular film strips were quickly hand assembled, there are noticeable gaps and overlap lines between strips, and other minor stray light discontinuities which are not to be construed as part of the lunar scene.

Several of the photographs are accompanied by only a brief statement as to location, area covered, and the angle of inclination of the sun at the target center. Any additional information was taken from the press-conference commentary of specialists of the U.S. Geological Survey who presented it at the Langley Research Center on October 6, 1966, for general circulation.

### GEOLOGIC INTERPRETATION OF SITE A-9.2 PHOTOGRAPHY

The westernmost of the sites photographed on the Lunar Orbiter Mission I was in the region of dark mare in the Ocean of Storms (Surveyor I target area) and was considered prior to the flight to be potentially one of the smoother terrain units of the lunar surface. It is of interest to observe the appearance of the site as photographed by the 61-in. reflecting telescope of the Naval Observatory near Flagstaff, Arizona (fig. 57), which is one of the best taken of this area prior to Lunar Orbiter I. The large dark area in the center of the marked frame is the one of interest, on the assumption that volcanic areas on the lunar surface which appear darkest and smoothest may be the youngest and possibly the least populated with crater fields and surface irregularities.

A special geologic map, prepared by Thor N. V. Karlstrom of the U.S. Geological Survey from Lunar Orbiter photographs of site A-9.2 and shown in figure 58, provides a wealth of new, detailed information on surface characteristics. A portion of a 300-meter ridge (shown in the center of fig. 46) is typified by faulting along its steep 20° slope on the western side. The eastern side of its slope is much less severe. The lunar surface at such locations is broken into blocks, much like the fault blocks in the western United States. Also indicated is the slumping of blocks off slopes and their downward movement under the force of gravity.

In the escarpment shown in the lower portion of figure 58 (clearly visible in fig. 46) the rocks are broken and exposed to view, showing 300 meters of layered rock. The dash lines represent material moving downward, a process called mass-wasting. Apparently, this is a very active process on the moon. Some of the blocks moving in this area are over 100 meters in length. At the foot of the slope is a convex-upward bulge that represents the piling up of material that has progressed down the slope. Two basic processes are indicated: first, the breaking of the surface and its uplift and, second, the wearing down of the surface by the mass-wasting action.

## CRATER EJECTA PATTERNS AND VOLCANISM

Figure 59 illustrates a basic characteristic of a high-energy explosion on a terrain. This large crater was formed by a test explosion of an underground nuclear device in Nevada. Its principal characteristics – deep penetration, steep side walls, slumped and wasted inner ridge, and hummocked rim with pronounced ejecta rays – are typical and are found in many photographs of lunar terrain featuring large impact craters.

A striking similarity to this manmade earth crater is evident in figure 60, which shows examples of both impact and volcanic processes. The large impact crater is Encke C which exhibits all the detail of the heavily rayed ejecta field shown in figure 59. East of the crater Encke is a fault zone running north to south similar to the one observed at site A-9.2 in figure 45. There, however, an outstanding formation of a volcanic cone formed by volcanic ejecta is observed in the center of the fault. A number of features on the lunar surface believed to be volcanic had previously been observed from earth-based stations. Their origin is now confirmed by Lunar Orbiter I photography, and volcanism can be identified as a primary modifying process on the surface of the moon.

## EARTH-MOON PHOTOGRAPHY

The high-resolution photograph (fig. 61) is enlarged in figure 62 to give greater emphasis to the panoramic view of the lunar surface. At the time this photograph was

taken, the spacecraft was about 1200 km above the moon and moving farther away on its path in orbit around the far side as it approached the apolune point of the trajectory.

The distance spanned along the lunar surface is about 480 km. The diameter of the largest crater in the foreground is about 55 km. This scene shows a very tormented surface of the moon. The extremely cratered, pitted topography, with rugged undulating contours is typical of the far side of the moon. The craters, for the most part, are saucer-shaped and have a large diameter-to-depth ratio. There are benches along the walls, and large segments of the crater walls are slumped over the crater floors.

In this same photograph, the earth is setting behind the east limb of the moon (as viewed from the spacecraft). The north pole of earth is oriented to the right. The geographic north-south axis is inclined about $7^\circ$ northwest of the terminator in the northern hemisphere and by an equal amount southeast of it in the southern hemisphere. Greater detail of the cloud formations is shown in figure 63, which is an enlargement of the earth itself. As a guide for locating landmarks, figure 64 is included. This figure shows a globe illuminated to simulate the conditions which existed at the time of photography.

The ESSA I satellite which photographed earth the same day as Lunar Orbiter I, on August 23, 1966, provided cloud-cover photographs which assisted in the identification of land masses.

A principal feature of an oblique photograph such as that shown in figure 61 is the unusual sense of depth perception it presents of the terrain. Such a view is the one most likely to be experienced by an astronaut as he circles the moon on his approach to the landing site. Such photography is also of considerable value in the scientific study of the lunar terrain.

A second photograph (medium resolution) of the earth taken from lunar orbit viewing a significant portion of the far side of the moon is given as figure 65 to show the density distribution of large craters. A very large old crater with a central prominence surrounded by a relatively smooth floor is an outstanding feature shown in this region of the moon not seen from earth.
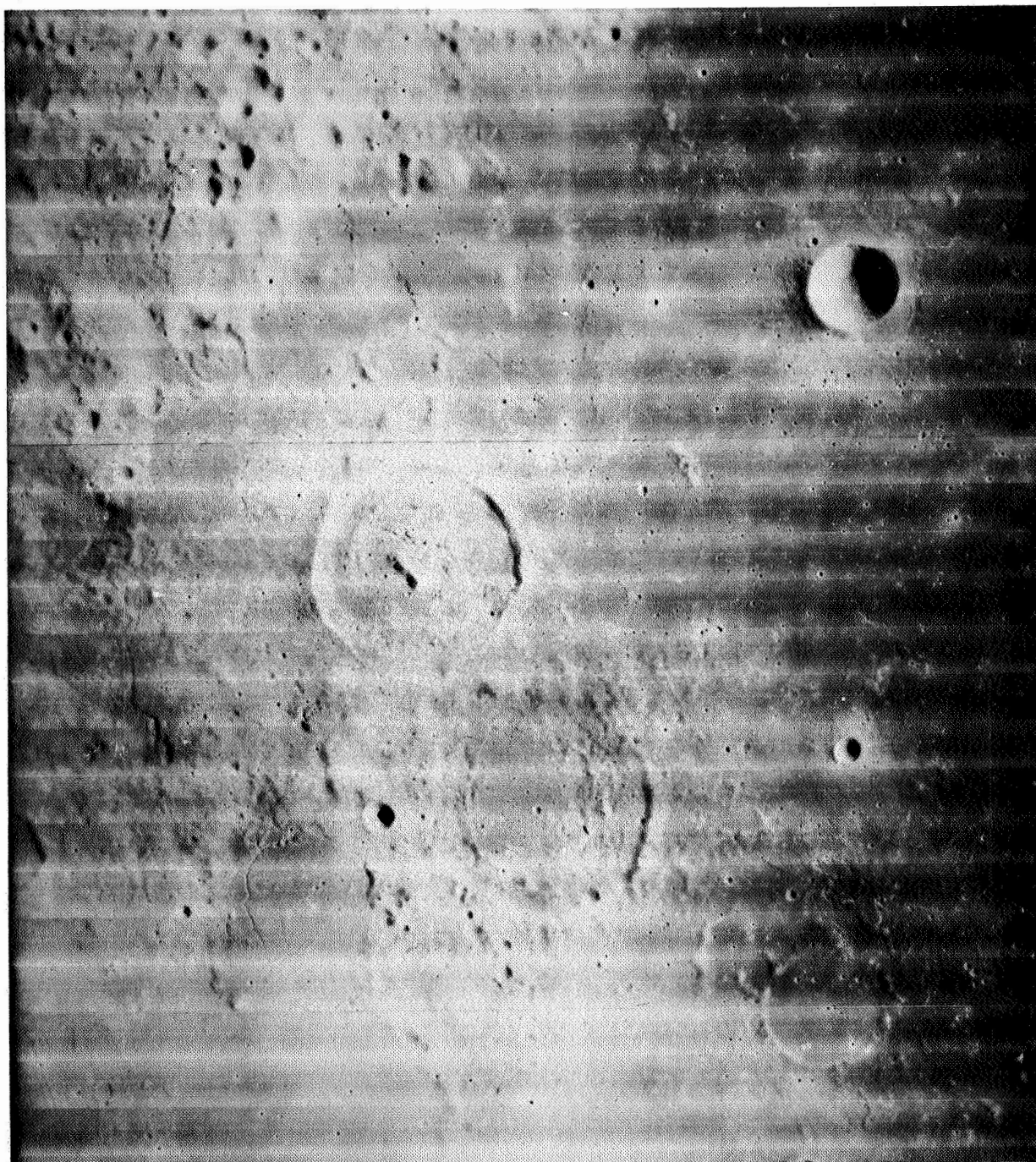
L-66-7840

Figure 38.- First photographic frame taken by Lunar Orbiter I of lunar terrain on August 18, 1966. Photograph is first of 16 taken at site A-0, located in Sea of Smyth, at approximately 83°59' east longitude and 1°54' north latitude. Sun angle is about 24° from horizontal. Area of lunar terrain shown is about 153 by 181 km (95 by 112 mi.).
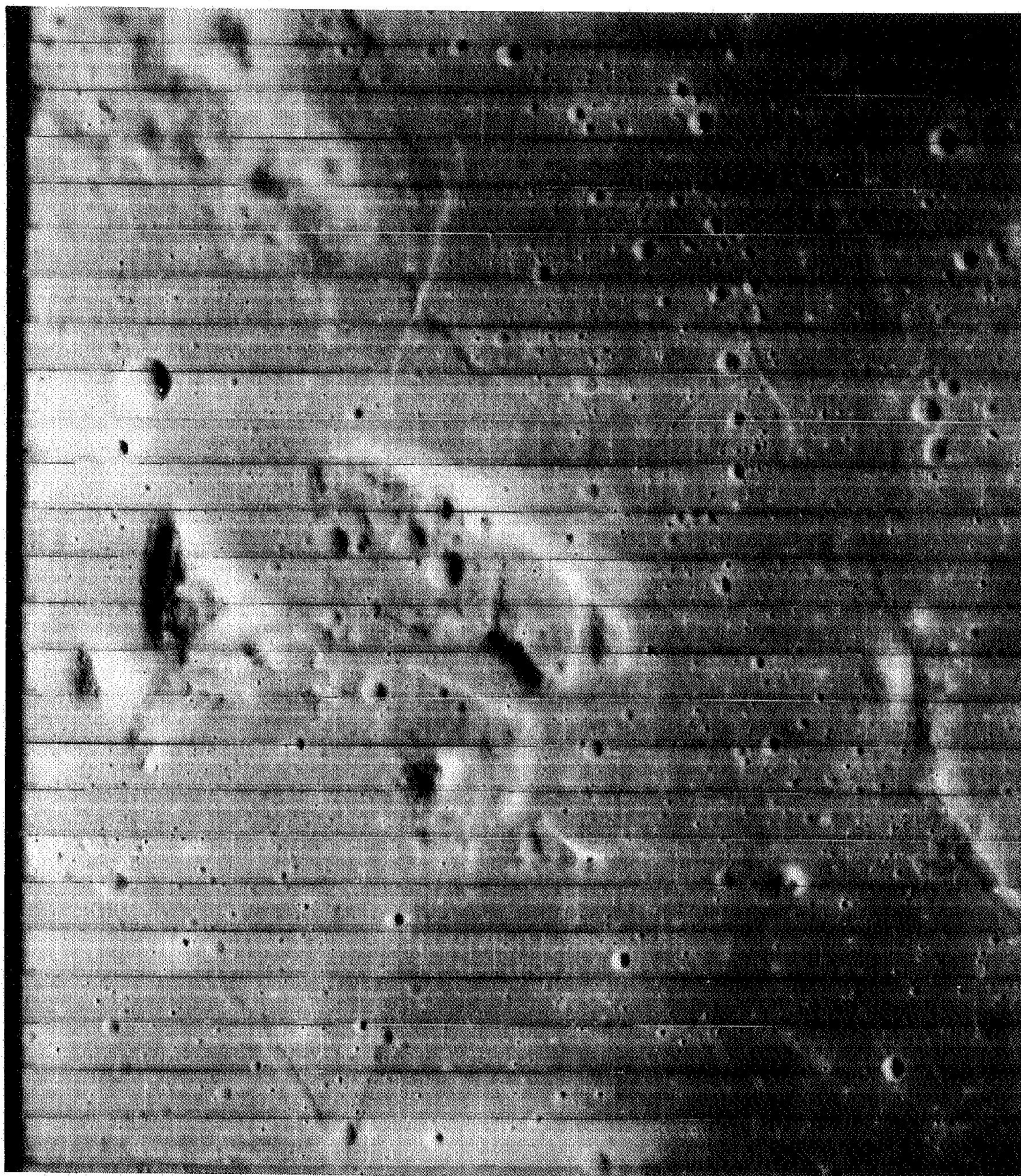
L-66-7830

Figure 39.- Medium-resolution photograph is eleventh of 16 taken of site A-1, located on western boundary of Sea of Fertility, at approximately 42°17' east longitude and 0°53' south latitude. Sun angle is about 29° from horizontal. Area viewed is about 37 by 43.5 km (23 by 27 mi.). A group of rugged prominences are clustered near center of frame; to right of center is an outstanding crater ray running north and south.
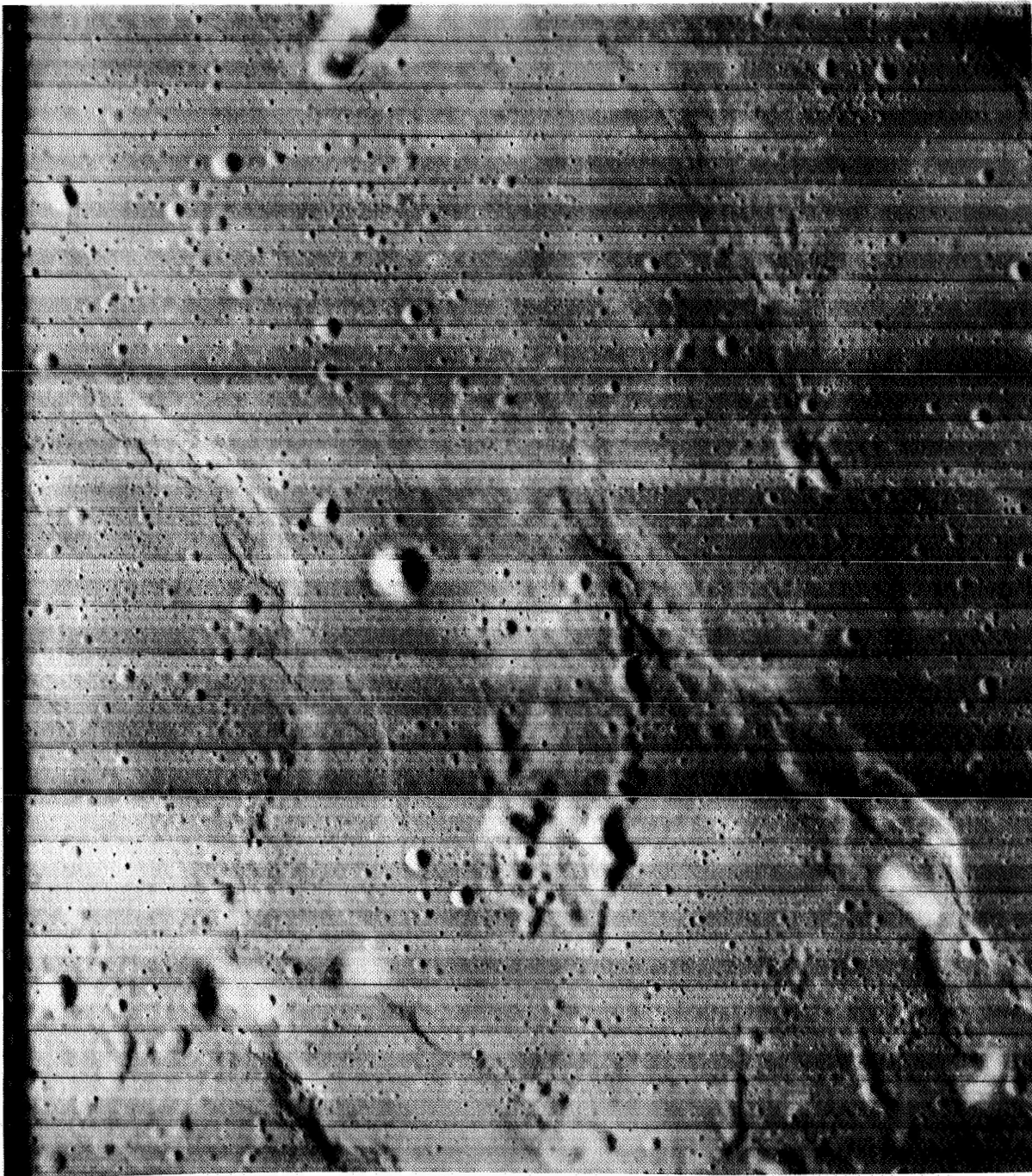
L-66-7845

Figure 40.- Medium-resolution photograph is twelfth of 16 taken of site A-3, located in Sea of Tranquility, at approximately 26°41' east longitude and 0°27' north latitude. Sun angle is about 21° from horizontal. Area shown is about 37 by 43.5 km (23 by 27 mi.). Region of mare is heavily populated with surface irregularities, ridges, and crevasses, and is quite heavily populated with deep craters.

L-66-7837
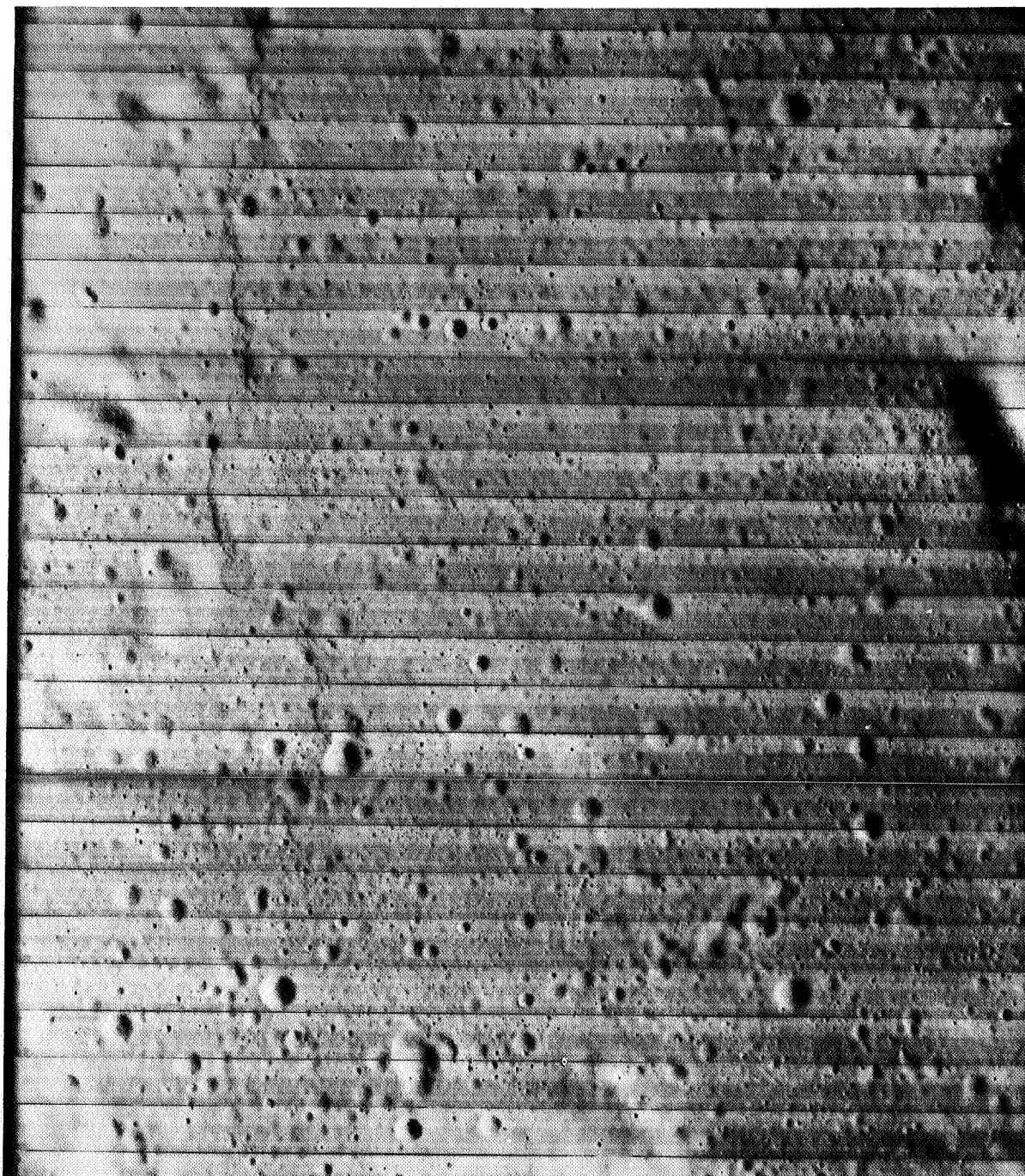
Figure 41.- Medium-resolution photograph is third of eight taken of site A-4, located in highland basin in east-central region of moon, at approximately 12°41' east longitude and 0°11' north latitude. Sun angle is about 20° from horizontal. Area shown is about 37 by 43.5 km (23 by 27 mi.). High density of craters is evident as is rent of surface running north and south in region left of center of frame.

L-66-7827
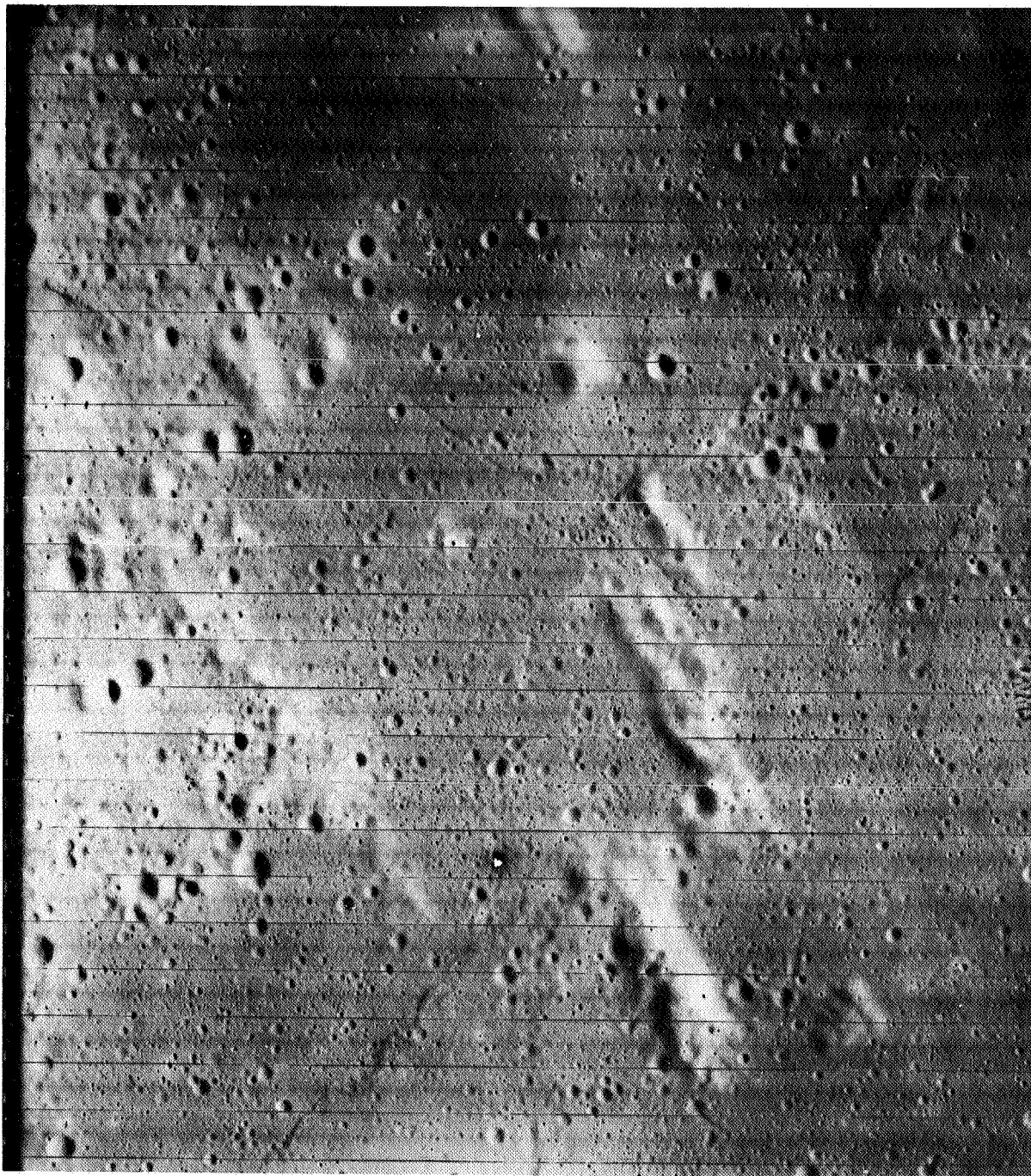
Figure 42.- Medium-resolution photograph is first of 16 taken of site A-5, located in Sinus Medii, at approximately 2°34' west longitude and 0°16' north latitude. Sun angle is about 20° from horizontal. Area of lunar terrain shown is about 37 by 43.5 km (23 by 27 mi.). Area of high reflectance on left and in two regions near center of frame denote steep slopes compared with surrounding mare. This mare region showed no such detail from earth-based photography.

L-66-7847
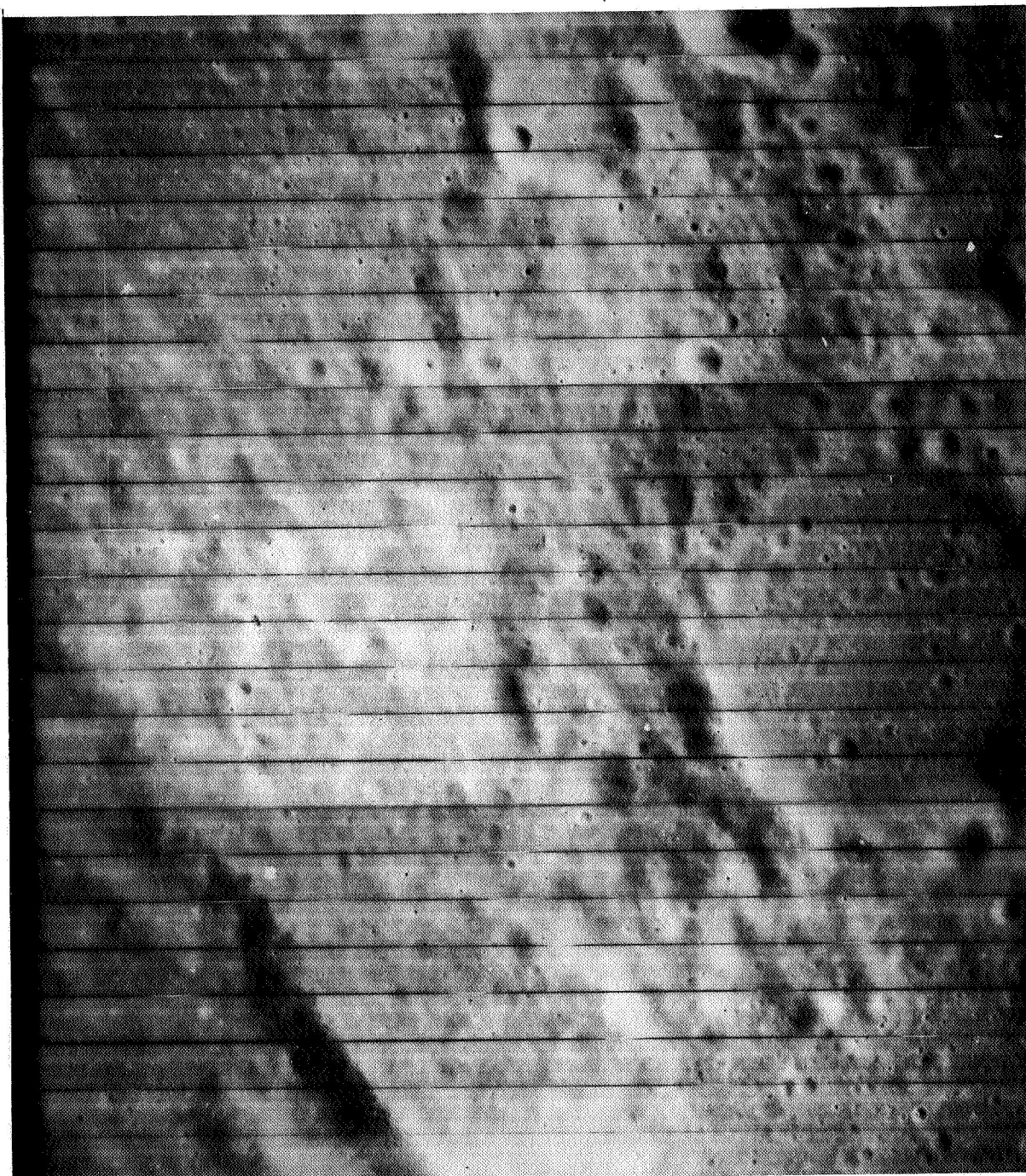
Figure 43.- Medium-resolution photograph is eighth of eight taken of site A-6, located south of Sinus Medii, at approximately $0°10'$ west longitude and $4°16'$ south latitude. Sun angle is about $36°$ from horizontal, which results in effective overexposure of scene and noticeable reduction of terrain detail. Area viewed is about 38.5 by 45 km (24 by 28 mi.).

L-66-7839

Figure 44.- Medium-resolution photograph is ninth of 16 taken of site A-7, located between craters Lansberg and Fra Mauro, at approximately 22°6' west longitude and 3°30' south latitude. Sun angle is about 33° from horizontal, which tends to obscure detail of lunar terrain. Area viewed is 34 by 40 km (21 by 25 mi.).

L-66-7828
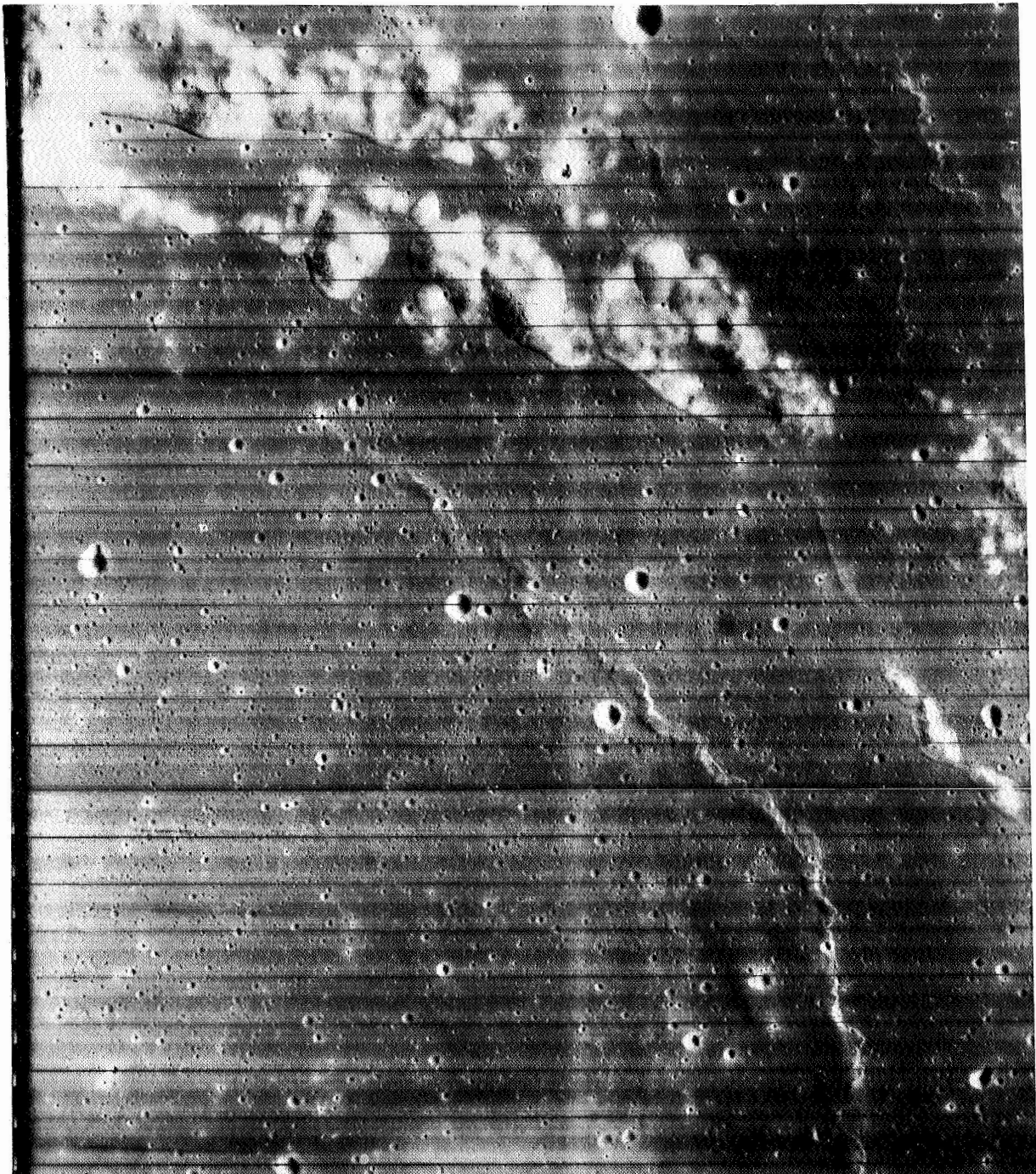
Figure 45.- Medium-resolution photograph is eleventh of 32 taken of site A-9.2, located in Ocean of Storms or Oceanus Procellarum, at approximately 43°14' west longitude and 2°1' south latitude. Sun angle is about 26° from horizontal. Area of lunar terrain shown is about 32 by 39 km (20 by 24 mi.). Prominent ridges are seen at top of photograph within general mare terrain.
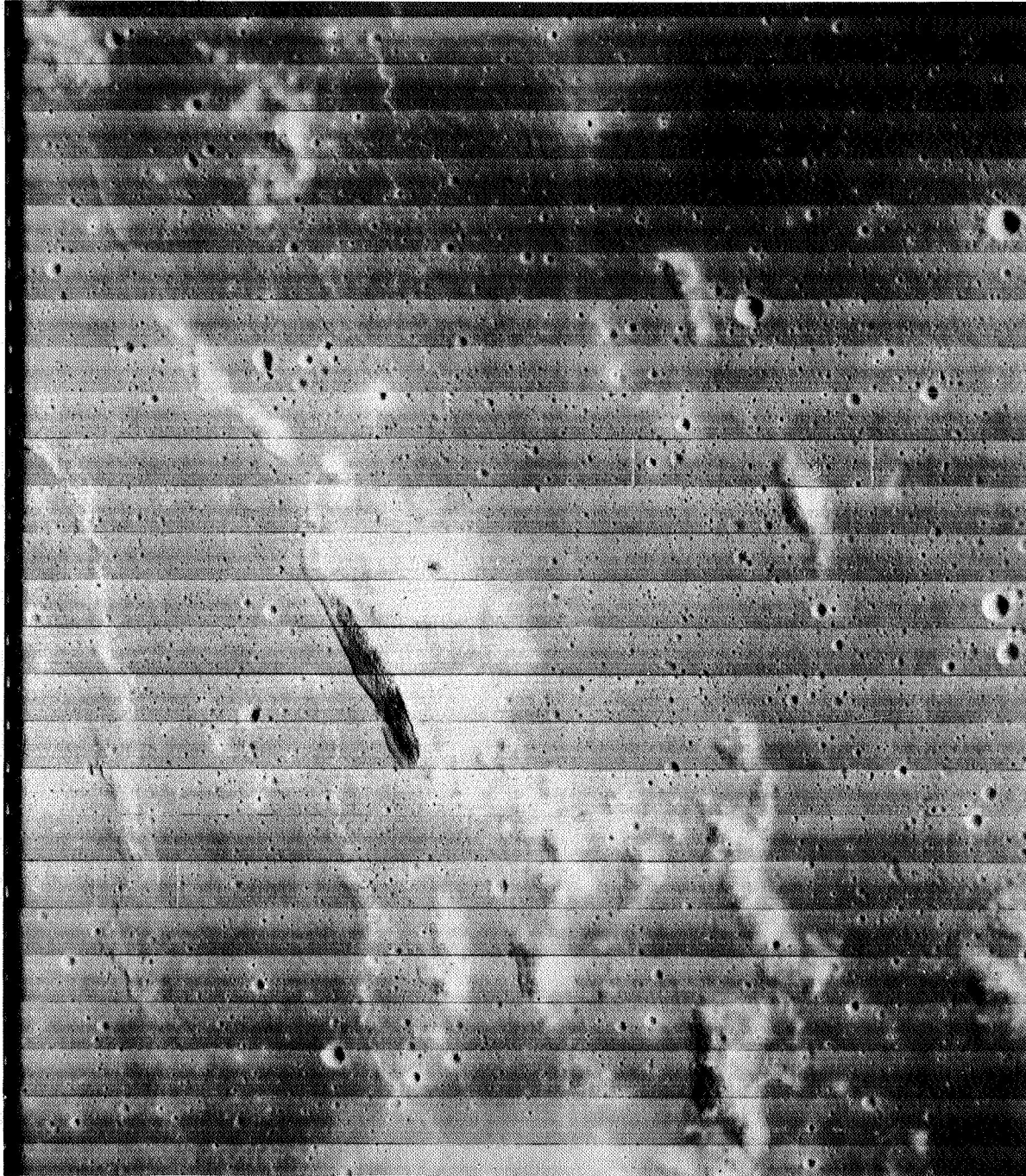
L-66-7843

Figure 46.- Medium-resolution photograph is last frame taken on Lunar Orbiter I flight and is thirty-second of 32 taken at site A-9.2 (Surveyor I target area) in Ocean of Storms, at approximately $42°35'$ west longitude and $2°34'$ south latitude. Sun angle is about $29°$ from horizontal. Area depicted covers about 32 by 39 km (20 by 24 mi.) of lunar terrain. Significant elevated areas are seen surrounded by mare.
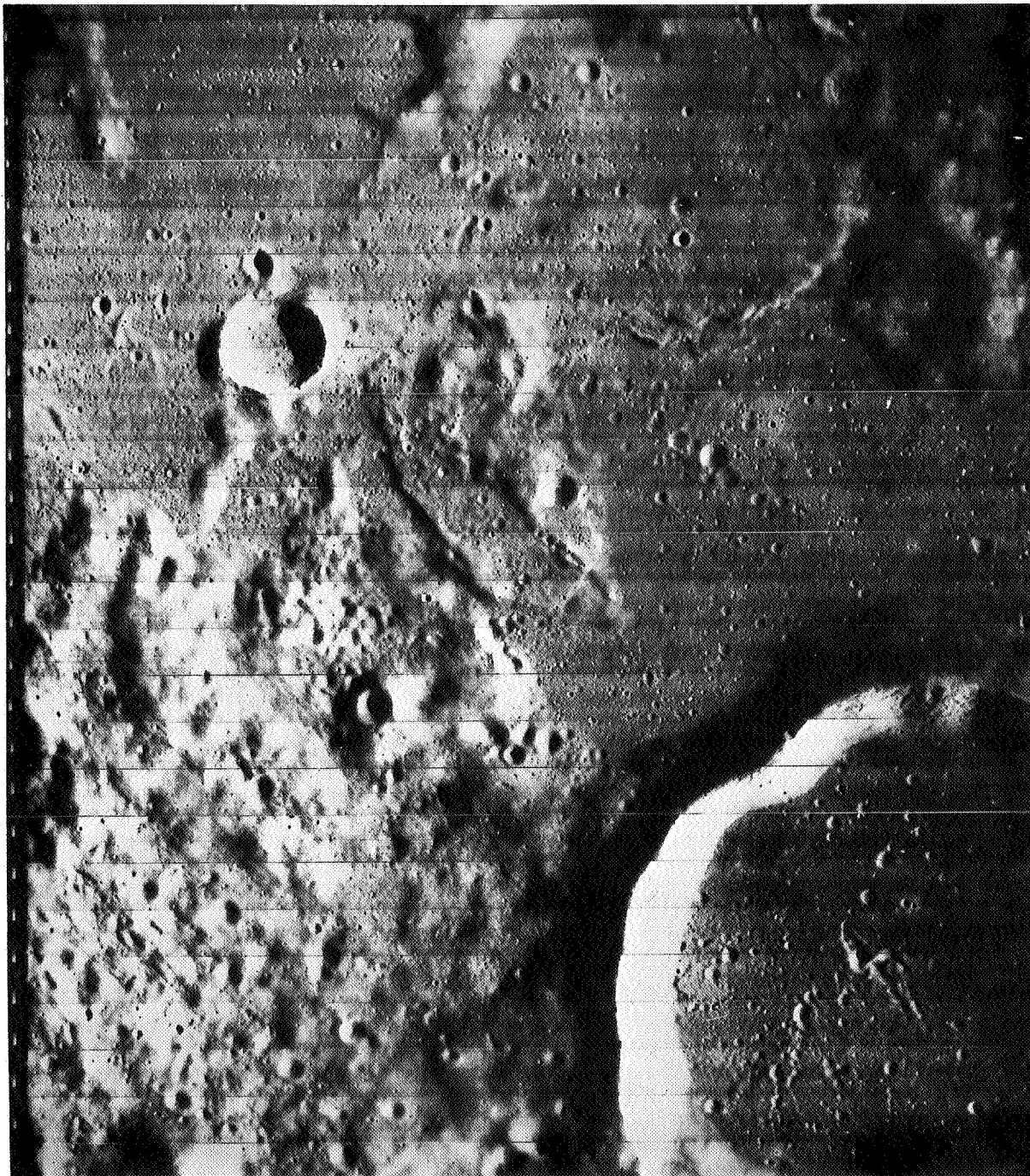
L-66-7829

Figure 47.- Medium-resolution film-set photograph was taken of area west of the crater Gambart, located at approximately 16°17' west longitude and 1°26' north latitude. Sun angle is about 12° from horizontal. Region shown covers an area of about 38.5 by 46.5 km (24 by 29 mi.). Large steep-rimmed crater appears filled with same mare material as covers upper portion of area photographed. Throughout rugged pinnacles and domes in highlands west of crater as well as mare and crater floor are chain craters alined approximately radially to crater Copernicus which is located to northwest.
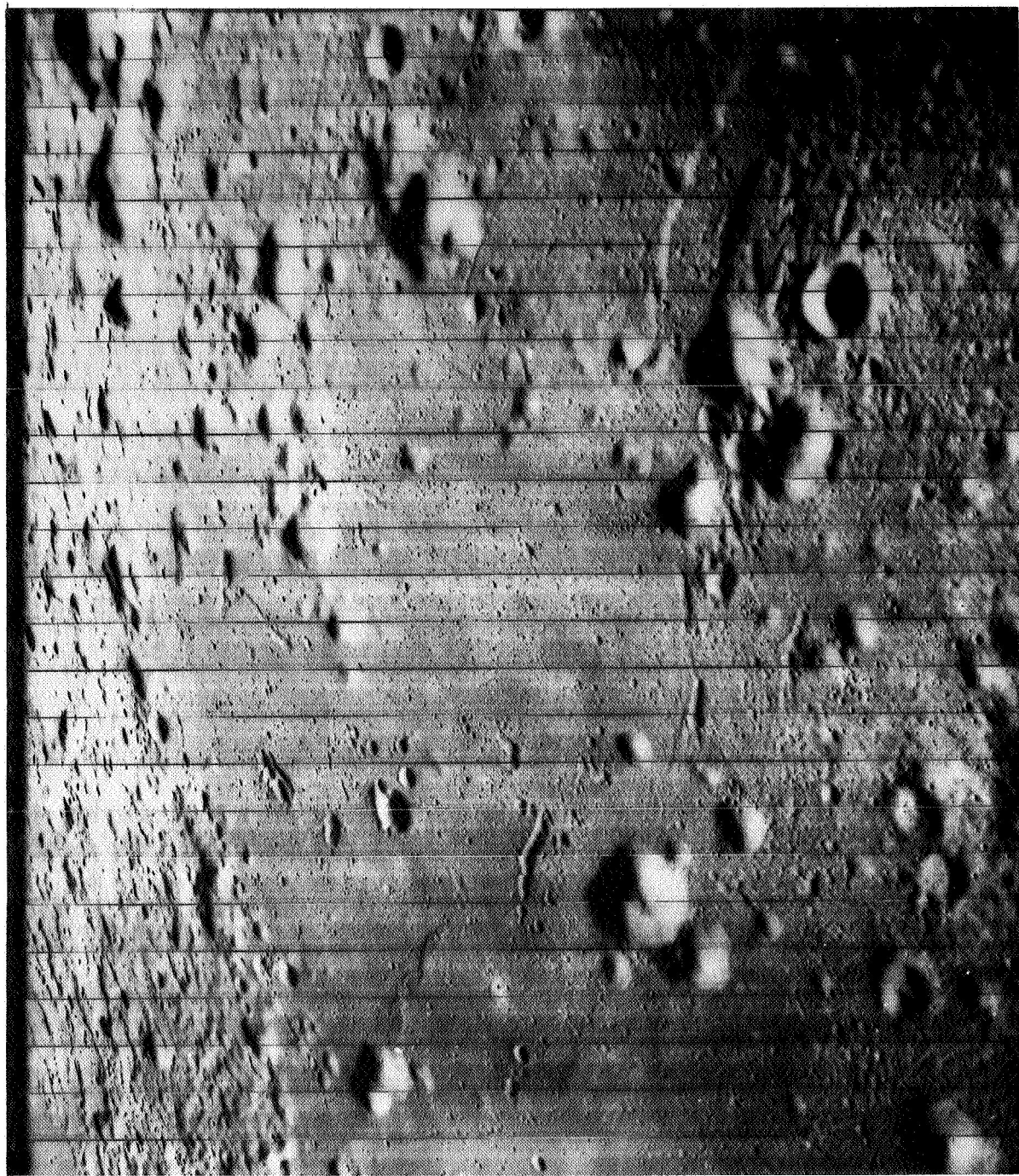
L-66-7842

Figure 48.- Medium-resolution photograph was taken at oblique angle of area west of crater Gambart, located at about $20^\circ 49'$ west longitude and $1^\circ 22'$ north latitude. Sun angle is about $13^\circ$ from horizontal. Region shown covers area of about 37 by 45 km (23 by 28 mi.). This mare region is populated with numerous mounds and mountains as well as ancient filled craters.
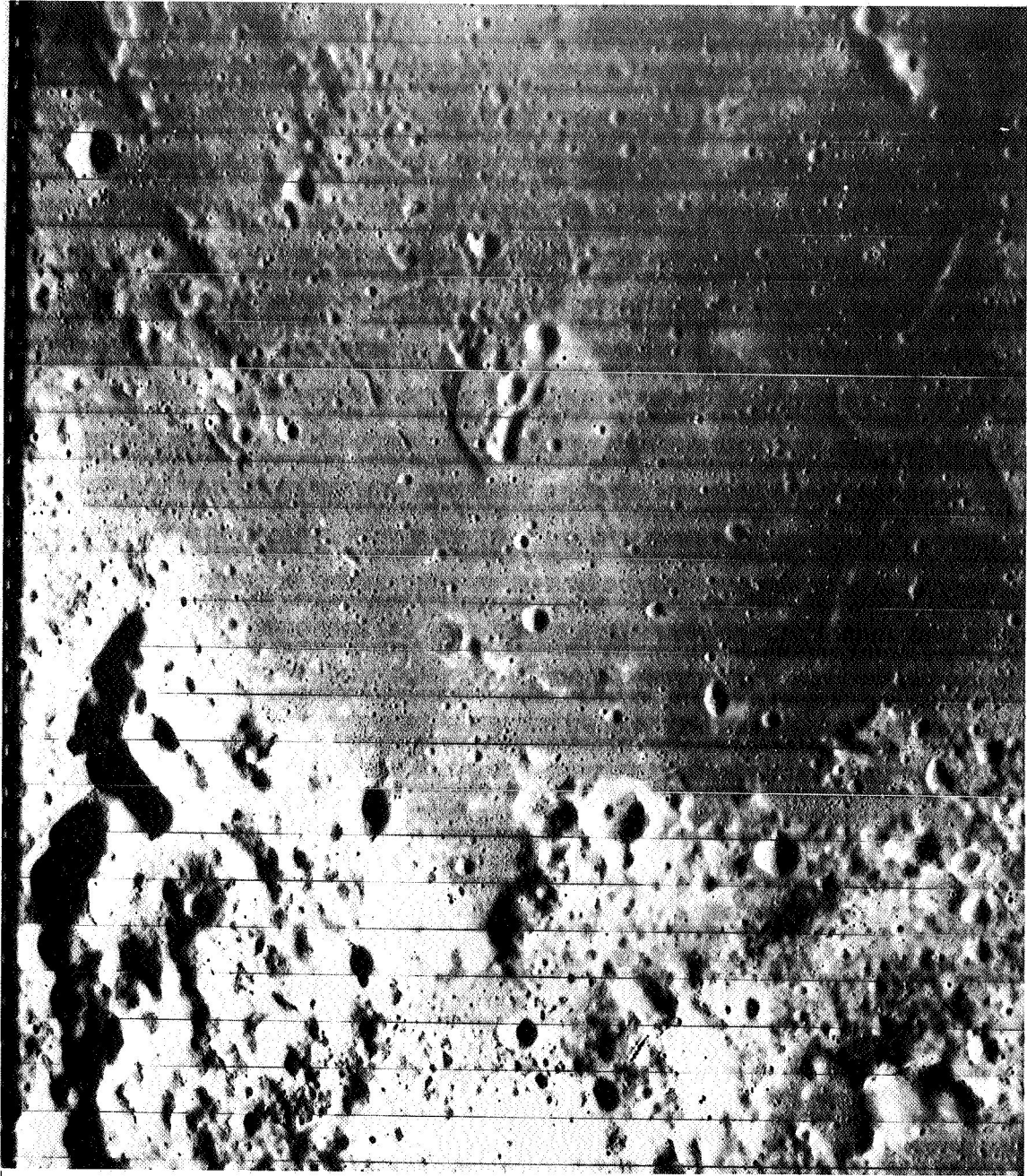
L-66-7833

Figure 49.- Medium-resolution photograph is one of two film-set frames taken of region located in Sea of Tranquility, at approximately 28°34' east longitude and 3°03' north latitude. Sun angle is about 16° from horizontal. Area of terrain shown is about 45 by 55 km (28 by 34 mi.). Although earth-based maps of moon indicate general area as mare, there is obvious gross variation in terrain type within this region. Contact between bright uplands (lower) and dark mare (upper) is clearly evident. The domelike feature in mare is thought to be of volcanic origin and has chain of craters running north-south and rather sharp escarpment on west side.

76
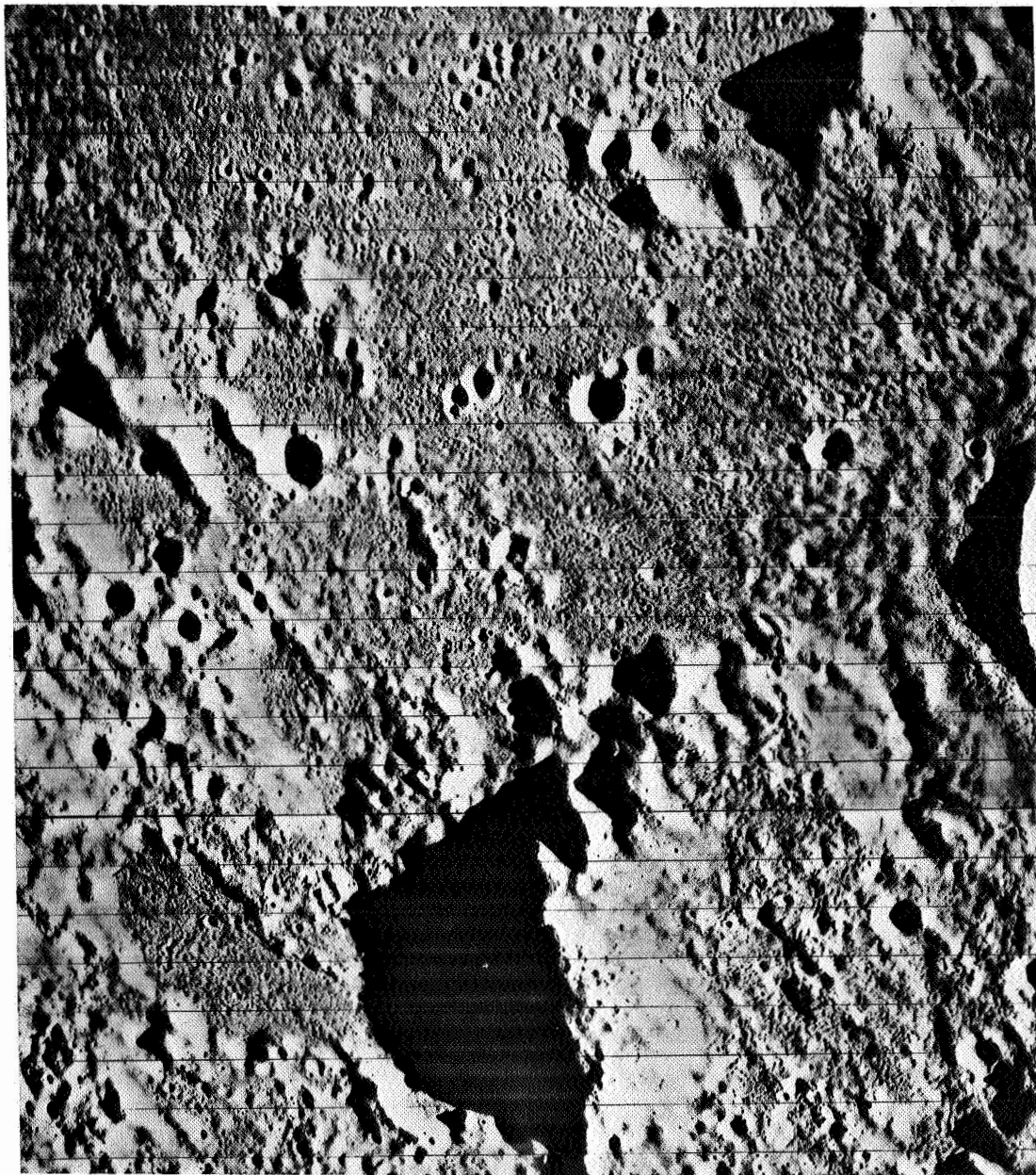
L-66-7859

Figure 50.- Medium-resolution photograph is film-set frame taken of area west of Dionysius, at about $14^0 34'$ east longitude and $3^0 3'$ north latitude. Sun angle is about $12^0$ from horizontal. Area viewed is about 52 by 62 km (32.5 by 38.5 mi.). Predominantly rough and heavily impacted terrain surrounds mountainous ridge outcropping about 1.5 km high. Detailed inspection of terrain close to large crater on right-hand edge of photograph reveals numerous great blocks thrown out, presumably from impact. Another pronounced feature is existence of great ridges which represent deposits formed by density currents flowing out from crater when material is thrown high at time of impact. This radial ridge pattern has also been observed at rimmed edges of volcanoes on earth, caused by ejecta flowing outward and downward from crater.
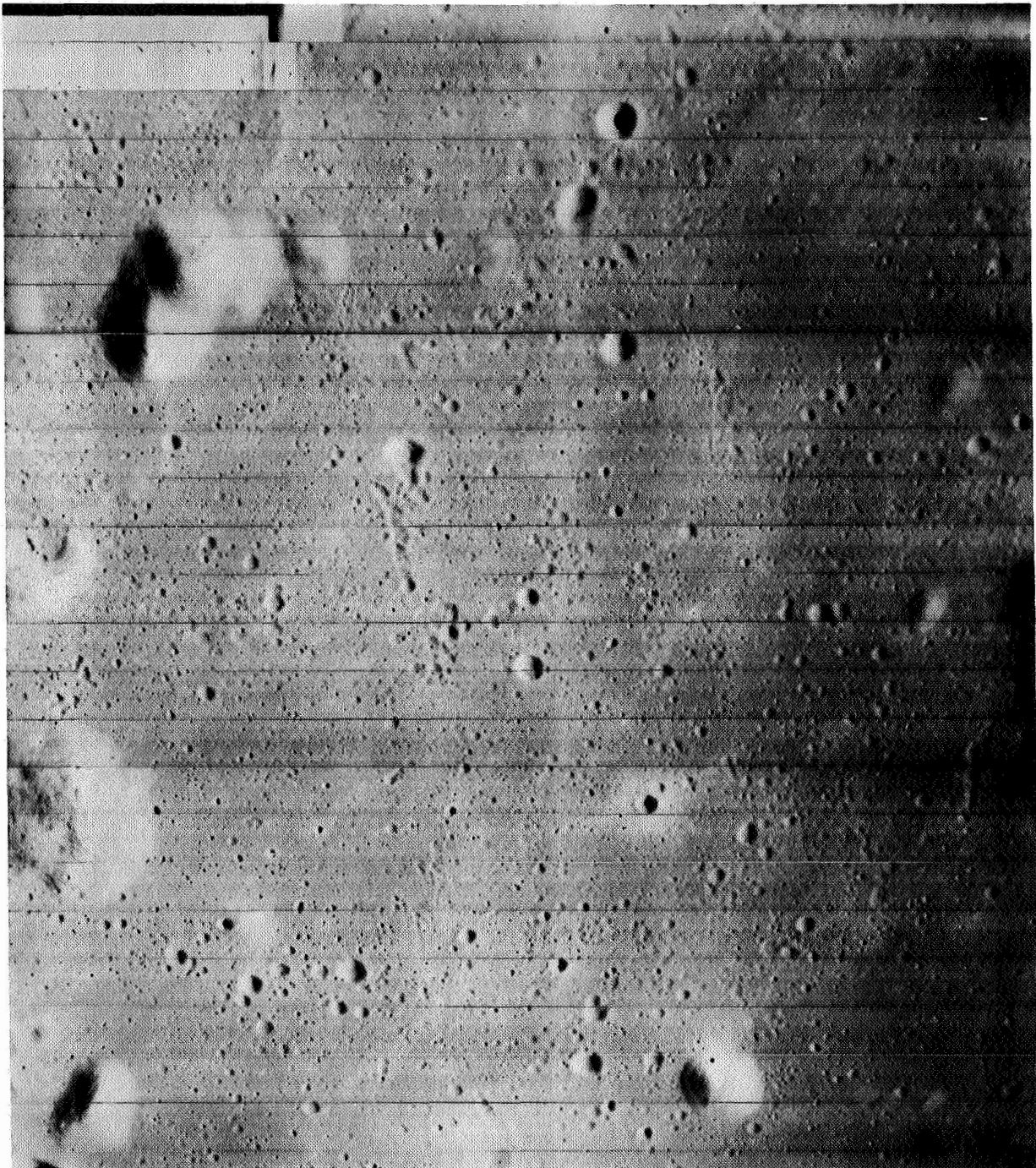
L-66-7860

Figure 51.- Medium-resolution photograph taken in Copernicus ray area located at approximately 20°8' west longitude and 0°14' south latitude. Area shown is about 31.5 by 37 km (20 by 23 mi.). Numerous mounds and domes are evident throughout crater fields in this rayed-mare area.

L-66-7838

Figure 52.- Medium-resolution photograph is single film-set frame taken of area on moon west of crater Lansberg, at approximately 30°52' west longitude and 0°46' north latitude. Sun angle is about 12° from horizontal. Area viewed is about 40 by 46.5 km (25 by 29 mi.). Central region of rough terrain is cratered as profusely as surrounding mare. Cleft through uplands region running northwest to southeast is rill of geologic interest. Also noted are numerous ejecta patterns from secondary material thrown out from impacts in direction of arrow-shaped crater chain.

L-66-7954
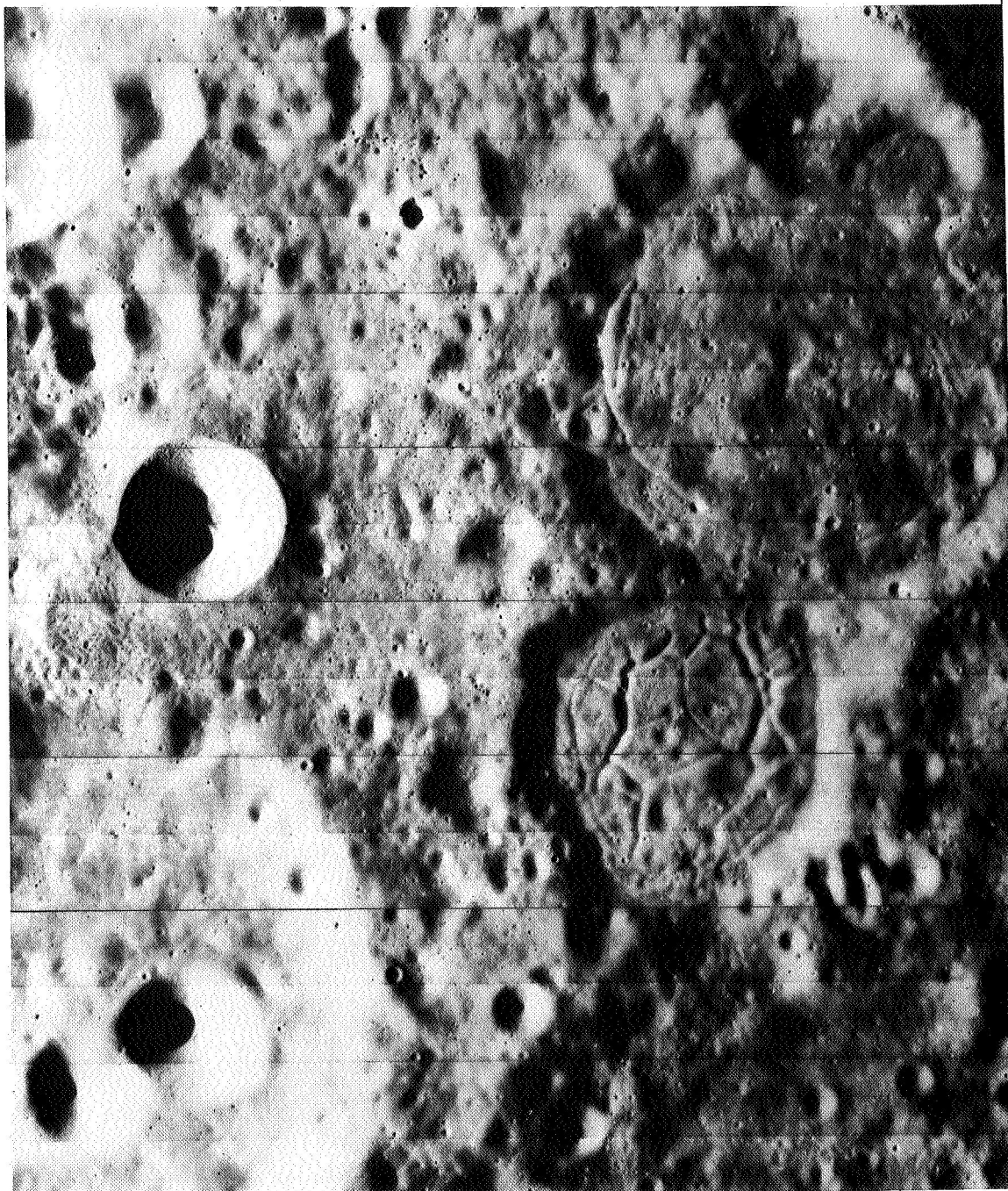
Figure 53.- High-resolution photograph is portion of frame taken on hidden side of moon at approximately 144°14' east longitude and 7°37' south latitude. Area shown is about 77 by 90 km (48 by 56 mi.). Terrain segment shows dramatic contrast of deep new craters and old craters with fractured floors. Larger old crater is about 38 km wide and heavily marked old crater is about 24 km wide.
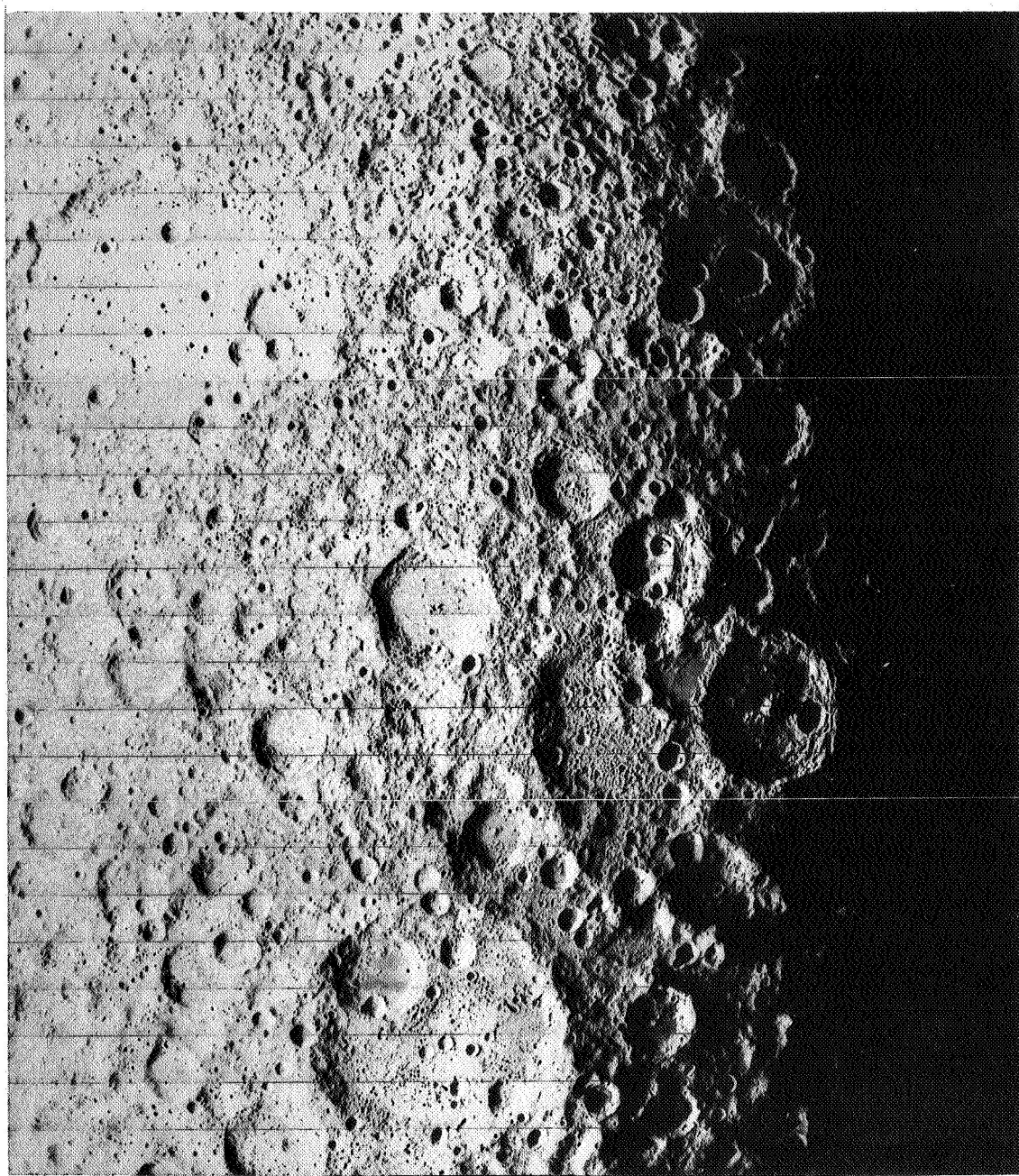
L-66-7831

Figure 54.- Medium-resolution photograph taken of far side of moon near terminator at sunset. Center of area shown is at approximately 152°20' east longitude and 6°7' south latitude. Sun angle is about 16° from horizontal at center of target area. Area shown is approximately 1300 by 1450 km (810 by 900 mi.). Very large old crater in upper left, nearly 400 km in diameter, has subdued, gently sloped walls which seem to be result of slumping of large masses of material from higher elevations to lower elevations. Large blocks have moved downward from wall to floor. Slumping now appears to be very prominent process on lunar surface. Large number of radiating features, of which many appear to be chain craters and others to be radial faults, are displayed in southern portion of photograph.

L-66-7836

Figure 55.- Medium-resolution photograph was taken of far side of moon at approximately 128°38' east longitude and 7°57' south latitude. Sun angle is about 20° from horizontal at target center of frame. Area of lunar terrain in view is about 1050 by 1240 km (650 by 770 mi.). Altitude is about 1300 km (800 mi.), which is almost sufficient to view terminator at sunset. Note marked difference in crater population between large crater remnant at top and large crater at lower center of frame. Also noted in this photograph is outline of that protion of lunar terrain presented in figure 56 which is a segment of high-resolution frame that was exposed simultaneously.
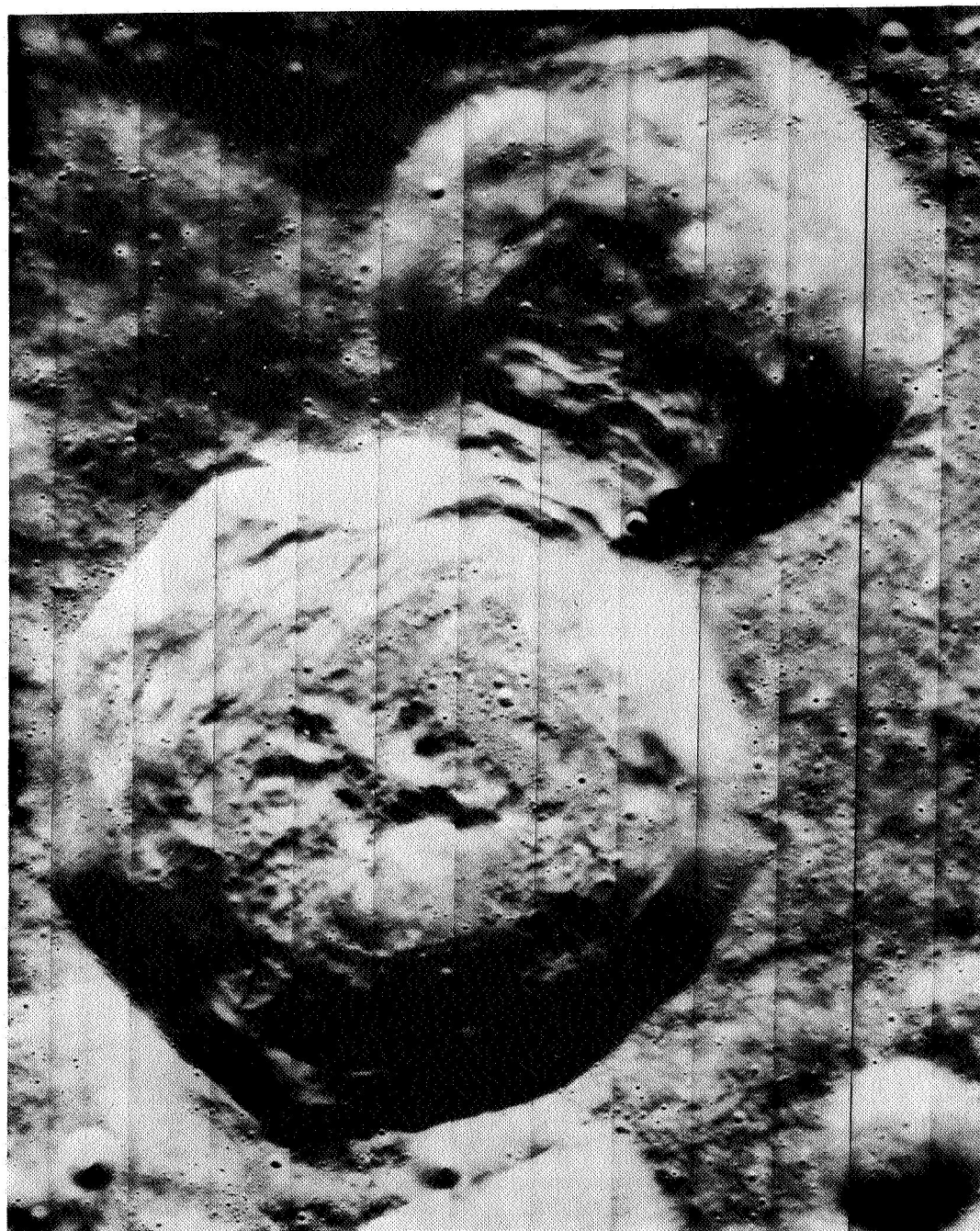
Figure 56.- High-resolution photograph is portion of frame associated with preceding medium-resolution frame and is located as rectangular outline on that frame. Area shown is about 69 by 84 km (43 by 52 mi.). Superposition of younger crater (50-km diameter) on an older crater (40-km diameter) is clearly shown as well as displacement of wall material into older crater. High density of smaller craters shown can be resolved to about 30 meters.

83
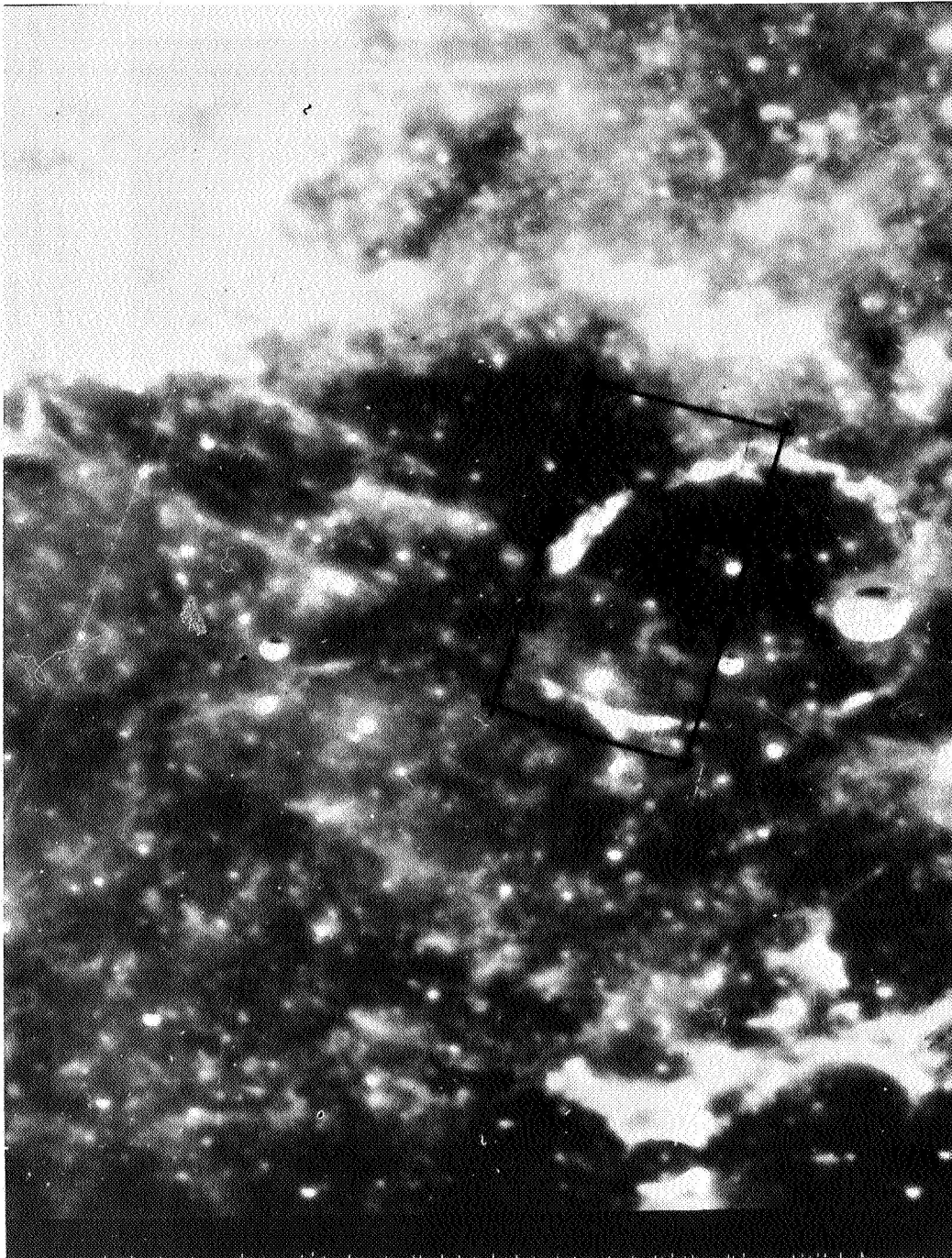
L-69-1205

Figure 57.- Full-moon earth-based photograph taken by 61-inch Naval Observatory telescope at Flagstaff, Arizona, of the region of Ocean of Storms. Boundaries of site A-9.2 photographed by Lunar Orbiter I are identified as centered about region of dark mare.

Preliminary Geologic Map
of
Site A9.2a M197

Explanation
U   Uplands
r   Mare Ridges
z   Mare with high crater
    density
x   Mare with lowest density
    of resolvable craters

Thor Karlstrom USGS
9/19/66
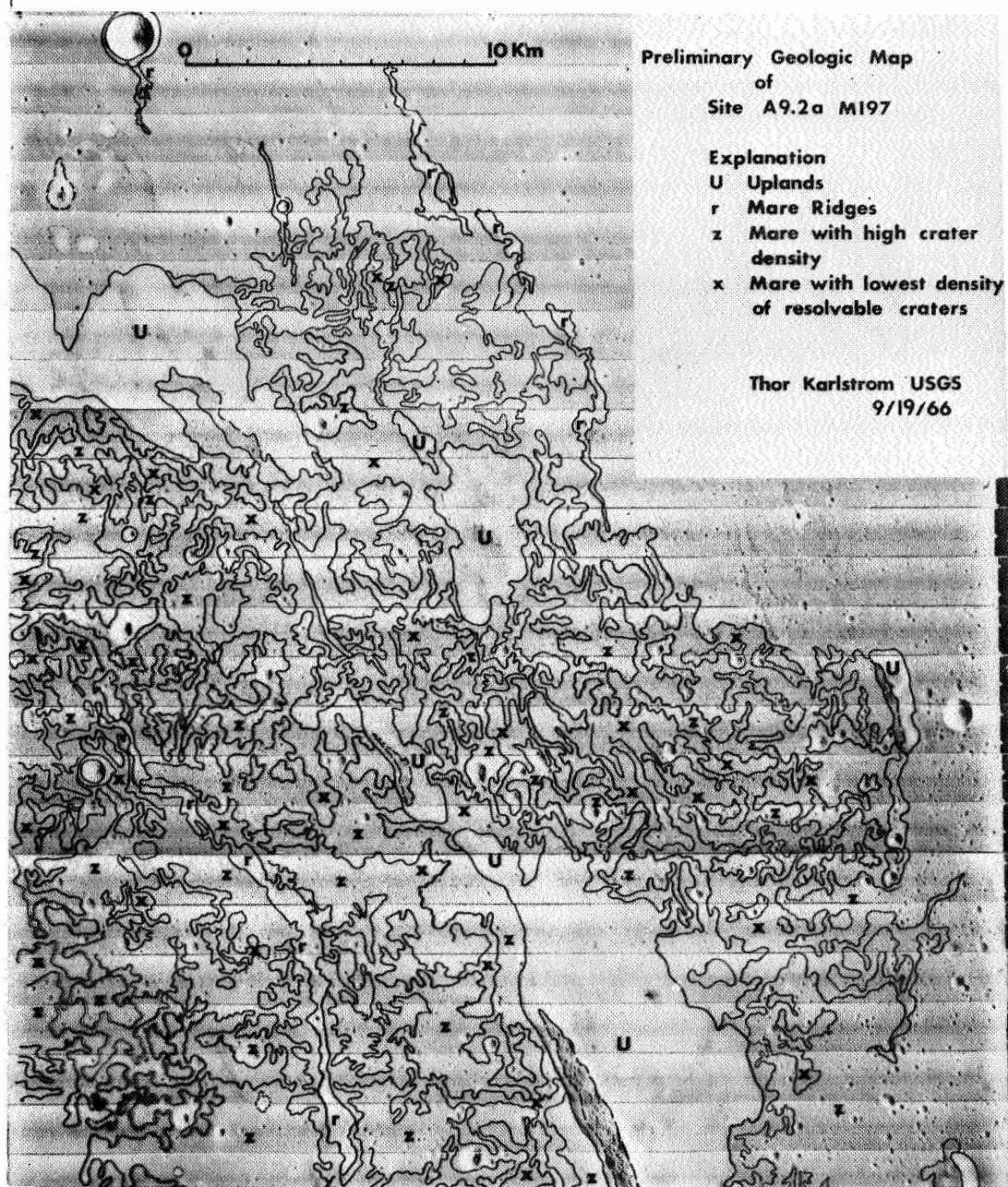
L-69-1206

Figure 58.- Preliminary geologic terrain map of eastern portion of site A-9.2 compiled by Thor N. V. Karlstrom, U. S. Geological Survey, showing specific regions of terrain types in area.

L-69-1207

Figure 59.- Crater formed by explosion of underground nuclear device at Nevada test site, showing steep crater walls, hummocked rim deposit, and secondary crater array.
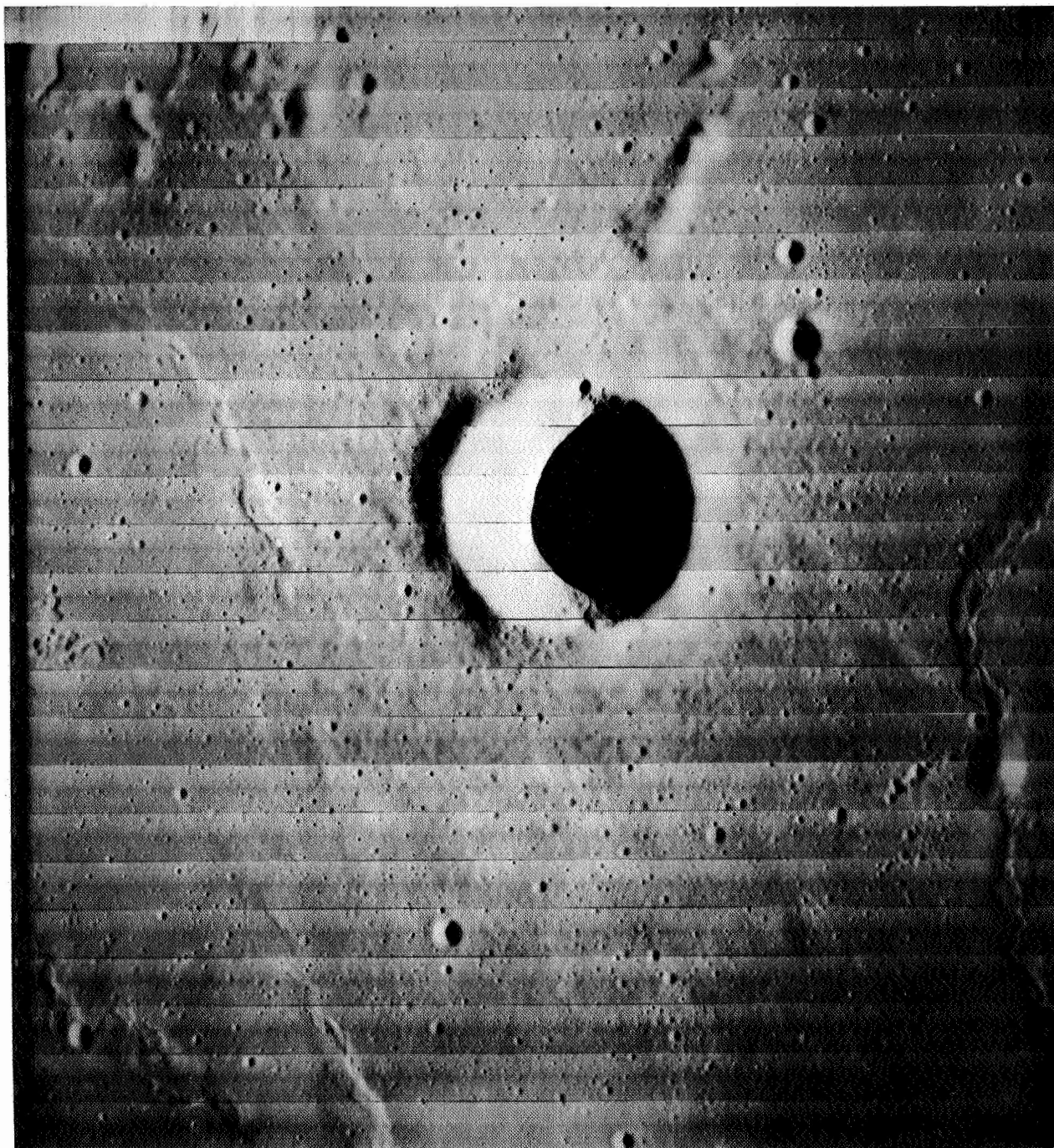
L-66-7832

Figure 60.- Medium-resolution photograph shows region of Ocean of Storms, at approximately 36°25' west longitude and 0°17' north latitude. Sun angle is about 14° from horizontal. Area shown on lunar surface is about 37 by 43.5 km (23 by 27 mi.). Singularly large crater centered in general mare area is about 9.5 km in diameter.

L-66-6399
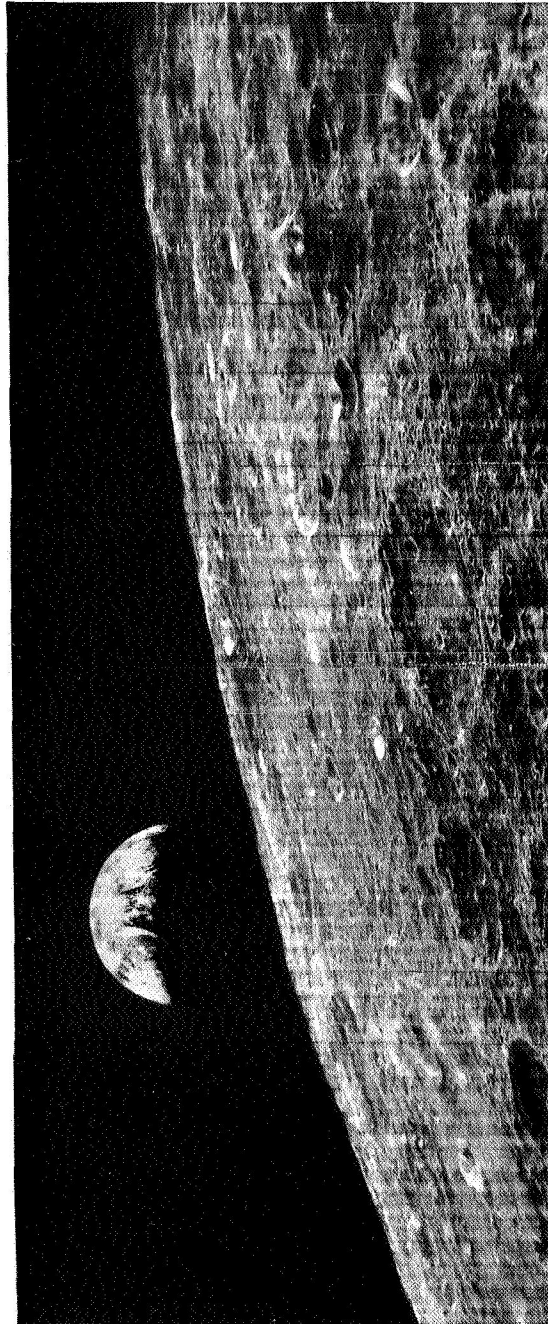
Figure 61.- High-resolution photograph of lunar surface just beyond eastern limb and with earth to left of moon horizon was taken August 23, 1966. East coast of United States is in upper left under reflectance from cloud cover. Europe and Africa are in darkness; Antarctica is at bottom of earth crescent. Photograph of lunar surface at such an oblique angle reveals crater contours and surface irregularities not observed by earth telescopes or Lunar Orbiter overhead photography normally employed over prime targets.
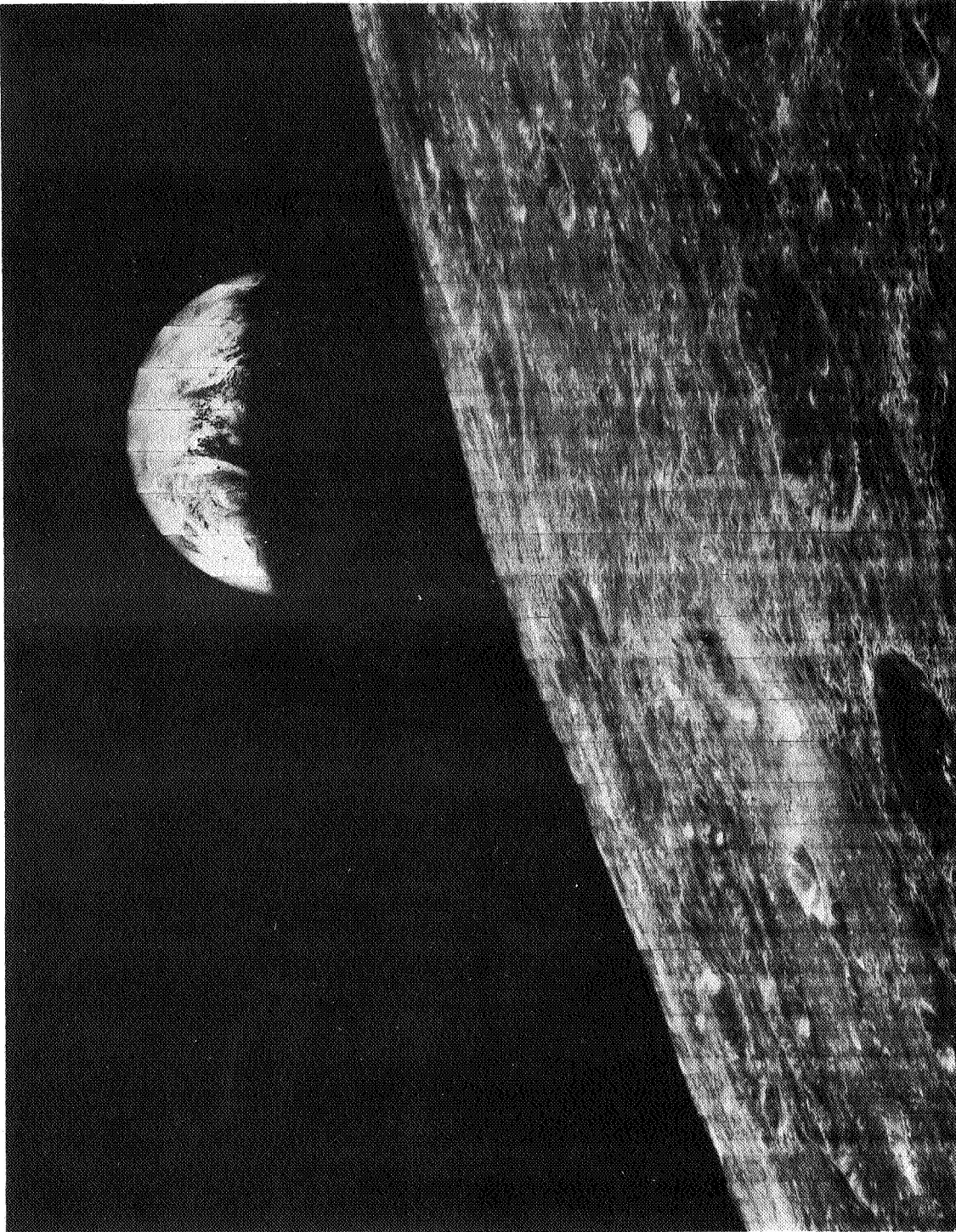
L-66-7825

Figure 62.- Enlargement of panoramic view of far side of moon with earth setting behind moon eastern limb.

89
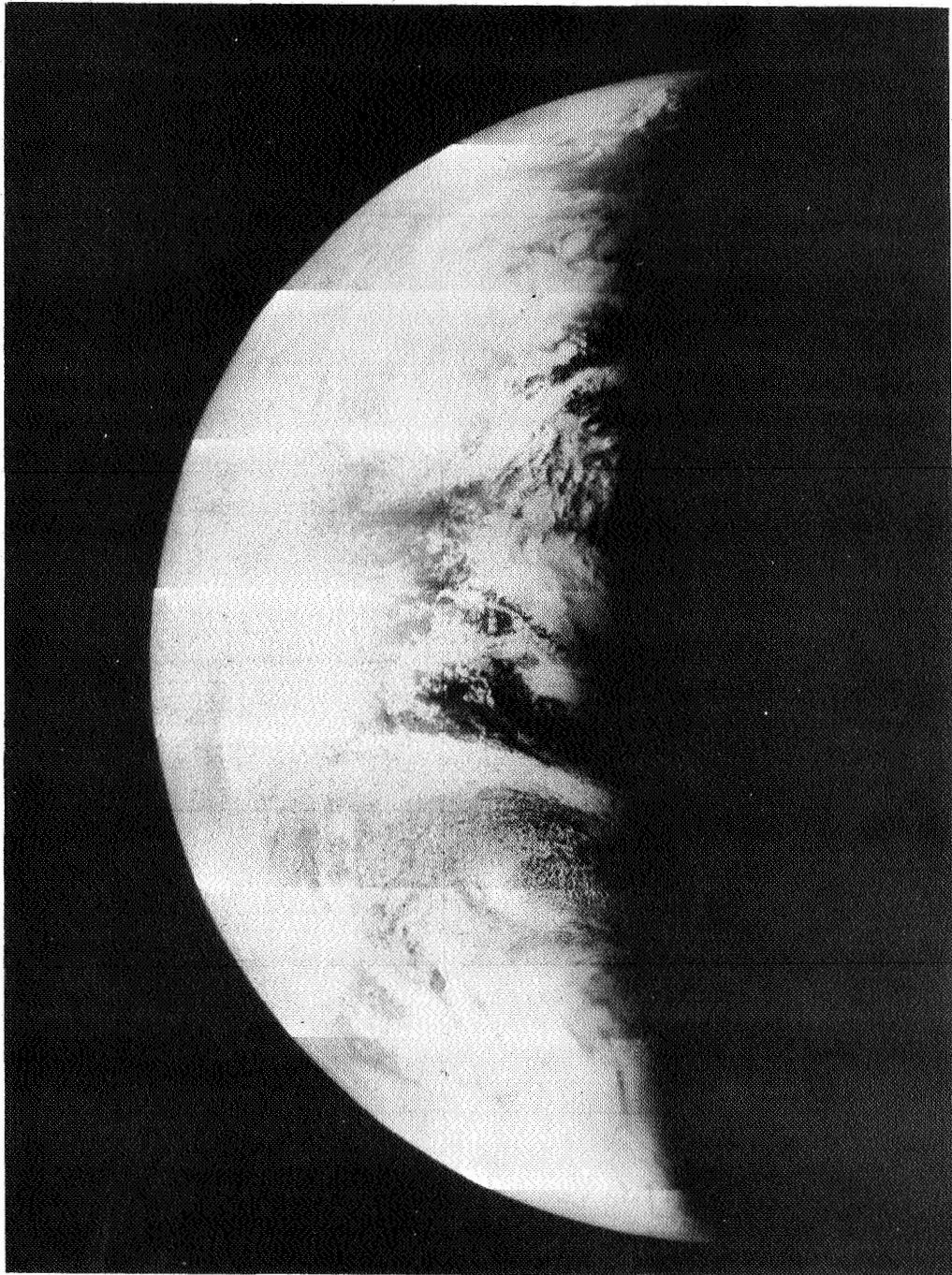
Figure 63.- Sevenfold enlargement of earth itself showing more clearly detail of cloud formations over Atlantic Ocean with very large cyclonic and anticyclonic weather patterns.
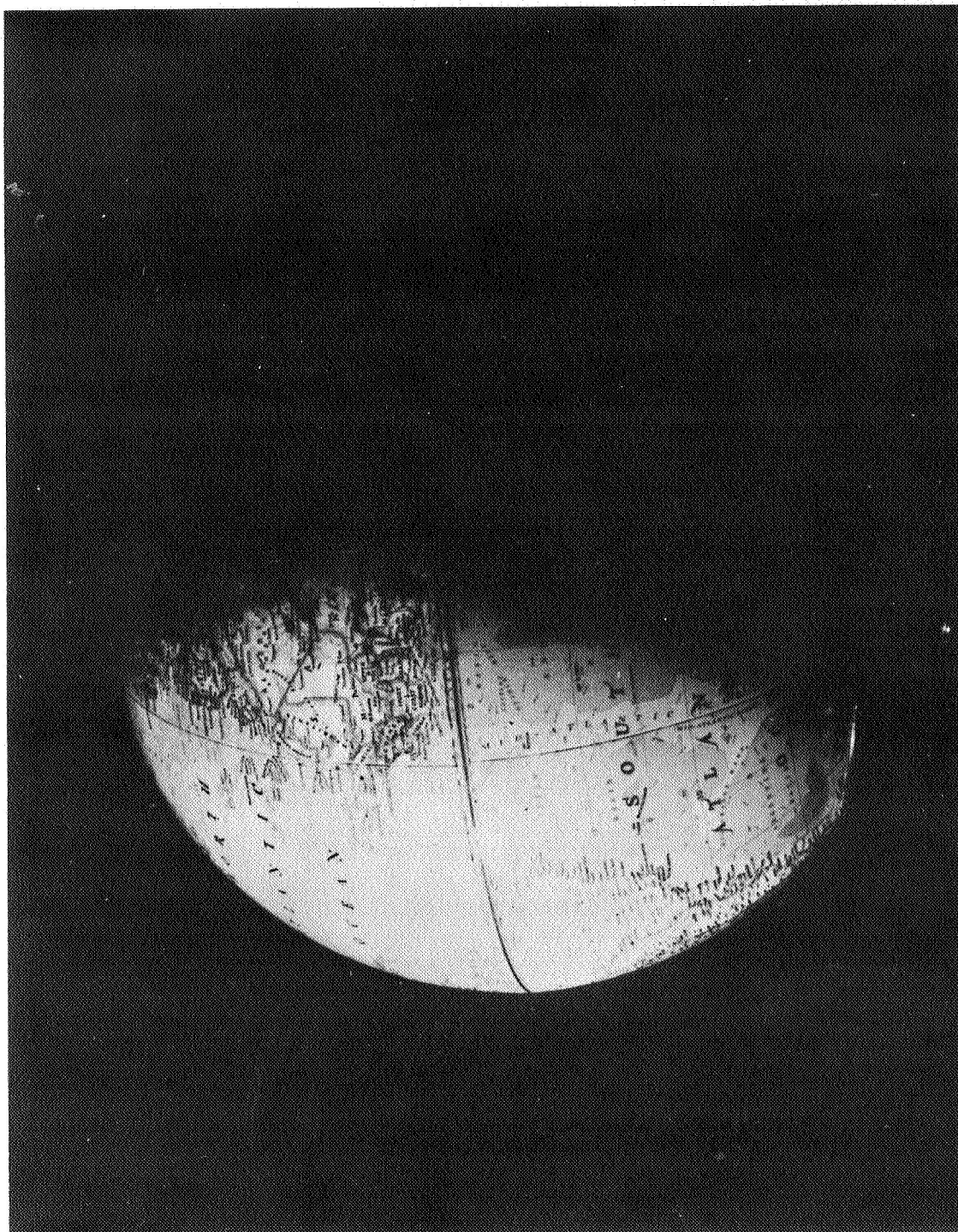
L-69-1208

Figure 64.- Illumination of globe of earth simulating conditions of photography of earth from lunar orbit as depicted in figure 61.
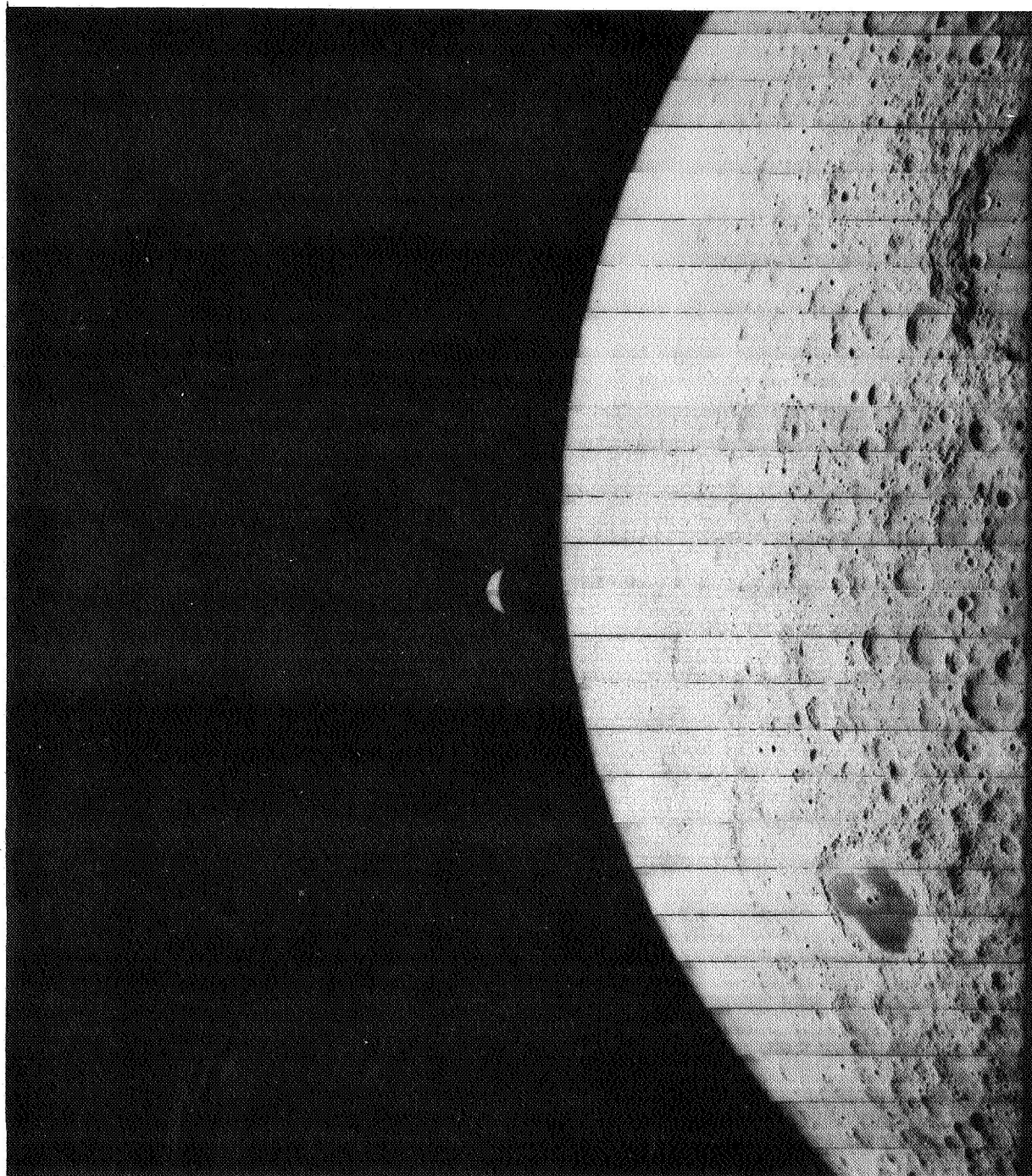
L-66-7849

Figure 65.- Medium-resolution photograph is second of two taken of earth and moon from lunar orbit, at point beyond eastern limb and viewing portion of far side of lunar surface. Photograph taken August 25, 1966.

# SELENODESY EXPERIMENT

## PRELIMINARY RESULTS OF GRAVITATIONAL-FIELD ANALYSIS

By William H. Michael, Jr., Robert H. Tolson,
and John P. Gapcynski
Langley Research Center

### General Analysis

Long-term objectives of the work at Langley Research Center on the Selenodesy Experiment are the determination of the precise properties of the lunar gravitational field, the moments of inertia and principal axes of the moon, the figure of the moon, the mass distribution within the moon and its internal structure, and precise positions of points on the lunar surface. It is expected that analyses using this information will lead to improved theories on the origin of the moon and the earth-moon system, the history of the moon, its internal composition, and related items.

The determination of the properties of the gravitational field of the moon is perhaps the most basic of these objectives. In addition to its use in scientific analyses, such information is required in order to predict the precise position and velocity of a lunar satellite at given times, for performing orbital transfers, rendezvous or orientation maneuvers, and other operations involved in either manned or unmanned lunar missions. The objective in this case is to determine the coefficients $C_{n,m}$ and $S_{n,m}$ (where $n$ is the degree of the coefficient and $m$ is the order) in the following expansion of the lunar-gravitational-potential function in terms of spherical harmonics:

$$U(r,\lambda,\phi) = \frac{GM}{r}\left[1 + \sum_{n=2}^{\infty} \sum_{m=0}^{n} \left(\frac{R}{r}\right)^n P_{n,m}(\sin \phi)\left(C_{n,m} \cos \lambda m + S_{n,m} \sin \lambda m\right)\right]$$

where $G$ is the gravitational constant, $M$ is the mass of the moon, $r$ is the radial distance from the center of mass of the moon, $R$ is the mean equatorial radius of the moon, $P_{n,m}(\sin \phi)$ are the associated Legendre polynomials, $\phi$ is latitude, and $\lambda$ is longitude. The analysis of the gravitational field is being carried out at the Langley Research Center with the use of computer programs developed specifically for this purpose. The primary basis of analysis is the use of a double-precision program using a weighted least-squares technique and having the capability of either coordinate-velocity or orbital-element differential correction. Solutions can be obtained for 58 gravitational parameters, including the coefficients in the expansion of the gravitational field for all $n + m \leq 10$. In addition, solutions can be obtained for the satellite state (i.e., position and velocity components), tracking-station positions, radiation pressure, control forces,

and earth-moon ephemeris scale factor, as well as for the usual bias parameters associated with satellite tracking data. The data used in the program are range and range-rate information obtained from the NASA Deep Space Network.

In any attempt to determine gravitational coefficients, the analyst must decide on how many coefficients to use in the solution and what batches of data to utilize. From experience with earth satellites and also from preliminary analyses for lunar satellites (ref. 1), it is well known that in order to obtain the best separation between the gravitational coefficients (particularly the zonal coefficients) data from satellites with a variety of inclinations should be processed. Currently such data are not available, and unbiased estimates of the even and odd zonal coefficients should not be expected. It has been shown (ref. 1) that an improvement in the separation of the tesseral coefficients can be realized by processing data evenly distributed over the lunar month. However, at this time analyses of such extended arcs of data have not been completed. Therefore, the results presented here should be considered to be of a preliminary nature.[1]

During the first few days after Lunar Orbiter I was injected into orbit, tracking data were continuously analyzed as received at Langley Research Center. The immediate objective of these analyses was to produce estimates of the overall gravitational field of the moon for the purpose of predicting the variations in the orbit of the spacecraft so that decisions could be made with respect to control of the mission. This objective was accomplished. These early results indicated that there was no danger of the spacecraft impacting on the surface of the moon before completion of the photographic readout. It was further determined that the orbital variations during the period of photography would not significantly degrade the quality of the photographs, and that there would be sufficient lifetime in orbit to obtain data for the Selenodesy Experiment and other experiments. (See ref. 2.) These results were considered to be sufficiently accurate to permit orbital transfer maneuvers from the initial lunar orbit to a lower intermediate orbit and then to the lower final orbit with pericenter altitude very near the optimum value for closeup photographs of the lunar surface. These maneuvers could not be designed with much confidence prior to this first flight because of the lack of knowledge of the higher components of the lunar gravitational field.

These early results were obtained during the real-time analysis of the tracking data from the first 4 days in the initial orbit. The data spanned a time from August 14 to August 17 and represent four complete tracking passes of each tracking station. Even though this solution set proved adequate to be used for early mission control, the set was not accurate enough to predict the satellite motion over extended time periods.

A second analysis has been performed by use of tracking data from the final orbit configuration. The tracking data used for this analysis covered the time span from

---

[1]The results presented here are those obtained as of December 1, 1966.

September 17 to September 26. The gravitational field determined from this set of data is given in the second column of table II. The data from August 18 to September 16 were not processed because of possible contamination by spacecraft maneuvers for photographic and other purposes. The third column of table II gives the gravitational field as determined by combining the results from both the initial and final orbits, and the fourth column gives the corresponding standard deviations in the estimates. At the bottom of the second and third columns is the average residual for the corresponding solution set. It is clear, from the standard deviations and by comparing the second and third columns, that very little can be said as yet about the individual gravitational coefficients. To reduce the standard deviations appreciably in order to get a stronger estimate, it will be necessary to process much larger batches of data and to obtain data from lunar satellites with higher inclinations with respect to the lunar equator.

It was found that the mass of the moon could not yet be determined with these data because of the very high correlation between the semimajor axis of a lunar satellite and the lunar mass. In order to ascertain the importance of the lunar mass in the estimation of the gravitational coefficients, the mass was held fixed at two distinct values and solutions were obtained for the coefficients. It was found that, over a range of mass values corresponding to the current uncertainty, no large changes were noted in the gravitational coefficients. Thus the lunar gravitational constant was fixed at 4902.58 $km^3/sec^2$. It was also found that $C_{2,0}$ and $C_{4,0}$, and $C_{3,0}$ and $C_{5,0}$, were correlated in pairs to such an extent that neither pair of coefficients could be simultaneously estimated. Therefore, for the results presented here, $C_{2,0}$ is fixed at a nominal value of $-2.07 \times 10^{-4}$, $C_{5,0}$ is set at zero, and the other two coefficients are included in the solution set.

A compromise must be made in choosing which gravitational coefficients to include in the solution set. On the one hand, enough coefficients should be included to reduce the mean residual to an acceptable level; on the other hand, the solution set must be restricted enough to give a fairly strong solution. There is always the possibility that one or more large gravitational coefficients are being neglected in the solution and that their effects on the data are being absorbed in the solved-for parameters. To date no solution over an extended time arc has resulted in completely random residuals. Thus, in order to determine whether the unsolved-for gravitational coefficients are producing important biases in the solution set, a check was made of the capability of the solution set to predict the long-period variations in pericenter radius. This parameter was chosen because it can be determined with sufficient accuracy from very short data arcs.

Four sets of gravitational coefficients have been studied, using the initial orbit data. One set, which included only the second-degree terms (five coefficients), did not give a sufficiently small average residual to be considered a good fit to the data. A second set which included all terms through third degree (12 coefficients) gave a reasonable fit to the data, in that the average residual was about 0.25 Hz. However, when this set of

TABLE II.- PRELIMINARY SETS OF LUNAR GRAVITATIONAL FIELD COEFFICIENTS

| Gravitational coefficients | Set 1 – Final orbit configuration | Set 2 – Combination of initial and final orbit configurations | |
|---|---|---|---|
| | Value of coefficient | Value of coefficient | Standard deviation |
| $C_{2,0}$ | $-2.0700 \times 10^{-4}$ | $-2.0700 \times 10^{-4}$ | ---------- |
| $C_{3,0}$ | .4461 | .3328 | $1.996 \times 10^{-4}$ |
| $C_{4,0}$ | .2089 | .0663 | 1.894 |
| $C_{5,0}$ | ------------ | 0 | ---------- |
| $C_{2,1}$ | .0881 | .1268 | 2.628 |
| $C_{3,1}$ | .4346 | .2175 | 1.534 |
| $C_{4,1}$ | -.0512 | -.0007 | 2.283 |
| $C_{5,1}$ | ------------ | -.1100 | 1.386 |
| $C_{2,2}$ | .2761 | .3380 | 1.363 |
| $C_{3,2}$ | -.0522 | .1485 | 1.224 |
| $C_{4,2}$ | .0279 | -.0674 | .521 |
| $C_{5,2}$ | ------------ | .0298 | .400 |
| $C_{3,3}$ | .0091 | -.0212 | .379 |
| $C_{4,3}$ | -.0047 | .0217 | .197 |
| $C_{5,3}$ | ------------ | .0041 | .049 |
| $C_{4,4}$ | .0009 | .0058 | .054 |
| $C_{5,4}$ | ------------ | -.0003 | .014 |
| $C_{5,5}$ | ------------ | -.0003 | .005 |
| $S_{2,1}$ | -.4106 | .1895 | 2.515 |
| $S_{3,1}$ | .1701 | .2895 | 3.218 |
| $S_{4,1}$ | -.1018 | .1559 | 2.010 |
| $S_{5,1}$ | ------------ | .1486 | 2.872 |
| $S_{2,2}$ | -.0577 | -.0583 | 1.446 |
| $S_{3,2}$ | .0187 | .0341 | 1.175 |
| $S_{4,2}$ | -.0834 | -.0191 | .390 |
| $S_{5,2}$ | ------------ | -.0386 | .365 |
| $S_{3,3}$ | -.0335 | .0124 | .361 |
| $S_{4,3}$ | -.0259 | -.0400 | .168 |
| $S_{5,3}$ | ------------ | .0062 | .054 |
| $S_{4,4}$ | .0017 | -.0001 | .055 |
| $S_{5,4}$ | ------------ | -.0002 | .017 |
| $S_{5,5}$ | ------------ | .0001 | .004 |
| Average residual | 0.7 Hz | 0.4 Hz | |

96

coefficients was used to predict the variations in pericenter radius the comparison with the observed variations was extremely poor. This indicated that some of the gravitational coefficients not being solve for were biasing the solution and that additional terms should be included. A third set of coefficients used in obtaining a solution included all coefficients through fourth degree (21 coefficients). The average residual for this fit was about 0.06 Hz. The comparison of the predicted and observed pericenter-radius variation indicated that the predicted variations had most of the basic properties of the observed variations, except that the predicted variations had a slightly larger long-period growth in pericenter radius than was observed. A fourth set of coefficients studied included all terms through fifth degree (32 coefficients). The resulting solution, for this relatively short data arc and with this large number of coefficients, did not indicate an improvement in the fit, and there was no appreciable reduction in the average residual. On the basis of these results, it was concluded that coefficients through at least fourth degree must be included in these preliminary analyses. As additional data were processed, the gravitational solution set was extended as required to keep the residuals to a reasonable level.

Each solution set was used to predict the variations in pericenter radius as shown in figure 66. This parameter was determined by The Boeing Company by processing tracking data which spanned only an orbit or two each day and the resulting values are also given in figure 66. The predicted curves were obtained by using the two gravitational parameter sets presented in table II and the state at a time at the beginning of the
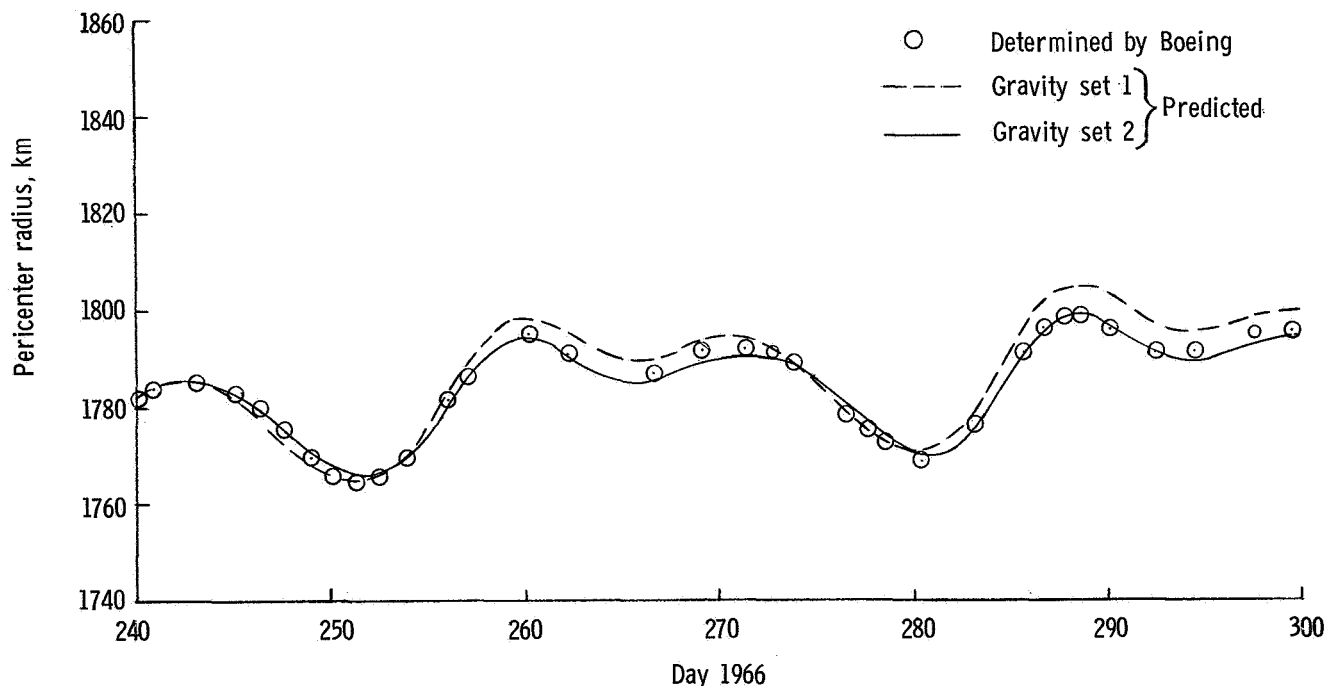


Figure 66.- Comparison of predicted and measured pericenter radii.

plot to calculate trajectories for the 2-month time period shown and thus to obtain the pericenter-radius variation. The best fit was obtained with set 2, which was based on 9 days of tracking data in the final orbit and 4 days in the initial orbit and which includes coefficients through the fifth degree. Using this set, the predicted pericenter-radius variation agrees with the values obtained from the short-arc solutions to within 2 km over the 60-day period. Of the parameter solutions including coefficients up to only fourth degree, the predictions based on set 1 gave the best fit, and the comparison of predictions from the two sets indicates the improvement obtained by including more coefficients and a longer data arc. Although the overall representation of the gravitational field as defined by set 2 fits the data fairly well, the values of the individual components are not yet very reliable and considerably more analysis is required as indicated previously.

## Related Studies

In addition to the general analysis described previously, the lunar gravitational field is also being determined at Langley Research Center from an examination of only the long-period and secular perturbations in the orbit of the lunar satellite. The computer program used for this analysis also utilizes a differential correction technique to obtain the gravitational coefficients. The "observational data" in this case, however, are represented by the long-period and secular variations in the "mean" orbital elements of the satellite orbit as obtained from the tracking data with use of the general analysis program described previously. The computed values of these elements are obtained from an integration of the Lagrangian planetary equations written in the form developed by Kaula in reference 3. The program, as written, can be used to determine the gravitational field coefficients of the same degree and order (up to $n + m \leq 10$) as the general analysis program. The analysis of the lunar gravitational field based on long-period and secular variations in orbital elements is currently underway at the Langley Research Center for the final orbit configuration.

With respect to selenodesy objectives other than gravitational field determination, Lunar Orbiter photographs are being used to determine the figure of the moon by determination of lunar radii at points covered by the photographs. The radius determinations involve application of photogrammetric techniques in conjunction with precise satellite orbit determination. Analytical procedures for the photogrammetric reduction have been developed at Langley Research Center and analysis of the photographic data is now in progress. Analytical procedures are also being developed to improve the knowledge of the time and position in orbit at which the photographs were taken. The photogrammetric determination of the figure of the moon will provide confirmation and possibly improvement in the values for lunar radii as determined from the V/H sensor, discussed in the section on results from the V/H sensor experiment.

# References

1. Tolson, Robert H.; and Compton, Harold R.: Error Analysis of a Weighted Least Squares Process to Determine the Lunar Gravitational Field. NASA TN D-3662, 1966.

2. Michael, William H., Jr.; Tolson, Robert H.; and Gapcynski, John P.: Lunar Orbiter: Tracking Data Indicate Properties of Moon's Gravitational Field. Science, vol. 153, no. 3740, Sept. 2, 1966, pp. 1102-1103.

3. Kaula, William M.: Analysis of Gravitational and Geometric Aspects of Geodetic Utilization of Satellites. NASA TN D-572, 1961.

# TRACKING DATA STUDIES

By J. Lorell and Warren L. Martin
Jet Propulsion Laboratory

## Foreword

The effort at Jet Propulsion Laboratory on the Selenodesy Experiment has among its objectives the long-term evaluation of the tracking data from the Lunar Orbiters to extract information on the moon's gravity field, lunar ephemeris, and other scientific information which may be contained in the tracking data. With about 2 months of data available, it is possible to draw some conclusions as to the quality of the tracking data for selenodesy. Although it is still too early to determine precise numerical values for any of the harmonic coefficients, some tentative sets of values, satisfactory for mission planning, have been obtained by the Langley Research Center.

Perhaps the most important conclusion for selenodesy so far reached is that the quality of the tracking data is up to expectation and will be adequate for the overall sele-nodesy program. Experience in working with the data has served to emphasize some of its peculiarities. In particular, overlap coverage (using two stations simultaneously) is essential to precise short-arc orbit determination. On the basis of this experience, plans are to obtain more overlap coverage during subsequent Lunar Orbiter flights.

Of highest importance for the selenodesy work has been the success of the ranging system. This system provides a basis for station time synchronization, making the overlap coverage data more effective, and also providing the prime type of data for measuring the lunar distance and thus improving the lunar ephemeris.

## Ranging and Time Synchronization Methods

The Lunar Orbiter I mission earned distinction for proving several new concepts. Among these were ranging and time synchronization. Both employed the Mark I ranging equipment which is capable of resolving lunar distances to 15 meters or better.

Ranging.- Range is measured in the following way. A pseudonoise code, transmitted by the tracking station, is received and retransmitted by the spacecraft transponder. At the tracking station the returning signal is correlated with a local code which is identical (except in phase) to that being transmitted. Correlation is obtained by delaying the local code until it exactly matches that being received from the spacecraft. The amount of off-set required to achieve correlation represents the phase displacement between the coders and is a measure of the round-trip time to the spacecraft. Range ambiguity is avoided by using a code with a period greater than the lunar round-trip time.

100

Since spacecraft usually have motion with respect to the ground station, the transmitted and received signal frequencies will differ. The range code includes a clock component to which the ground equipment is locked. Therefore, once synchronized, the local code will remain correlated with the incoming signal irrespective of the Doppler frequency shift. Since the Doppler shift is representative of satellite motion, it can be used to correct the range periodically.

For maximum accuracy, delays in both ground equipment and satellite transponder must be removed from the measured range. The transponder delay is measured accurately prior to launch, and periodic tests of the ground equipment assure that the system calibration is valid. Subtracting this calibration number from the measured range yields the true range with an accuracy of 15 meters.

Time synchronization.- Orbit calculations for the Lunar Orbiter spacecraft placed stringent requirements on the timing accuracy of the Deep Space Network (DSN). Where previously it had been adequate to synchronize two stations to within 10 msec, now it became necessary to calibrate the station clock offset to better than 50 $\mu$sec.

The resulting synchronization scheme employs the Mark I ranging equipment and is operative whenever two or more stations can simultaneously view the spacecraft. Time synchronization between two stations proceeds in the following way: Station 1 ranges in the conventional manner. This implies the transmission of a pseudonoise code to which the ground equipment is locked when the signal returns from the spacecraft. Station 2 also locks its receiver range coder to the returning signal; however, it does not transmit.

The Mark I receiver coders are designed to produce a marker pulse whenever a particular code vector (1111----111) appears. In addition to the code marker pulses each station independently generates timing signals. Assuming the rubidium frequency standards to be accurate, these timing pulses will differ by some arbitrary, but constant, phase from one station to another. It is this phase difference that must be measured.

At station 1 an elapsed time counter is started by a specific timing pulse (e.g., the first second of each minute during a common view period). This counter accumulates a time, $t_1$, until the appearance of the next marker pulse which terminates the process.

Station 2 emulates this procedure by using the equivalent-local-time tick and code-marker pulses to measure an interval, $t_2$. If the station timing signals were perfectly synchronized, the difference between the intervals ($t_2 - t_1$) should exactly equal the difference in range between the spacecraft and the respective stations. If this is not true then, depending on the magnitude of this inequality, the clock synchronization error will be known. Specifically, $t_2 - t_1 = t_s + t_r + t_e$ where

$t_s$            desired synchronization error

$t_r$            time corresponding to the range difference

$t_e$            various system errors

Errors $t_e$ arise from uncertainties in the predicted range, from inaccuracies in the equipment calibration, and from noise. Under worst-case conditions these errors were shown to be on the order of 5 $\mu$sec. Under usual conditions these errors are expected to be about 1 $\mu$sec.

Time synchronization experiments were conducted on August 16 and 17, 1966. Three stations participated in the experiments: DSS 12 at Goldstone, DSS 41 at Woomera, DSS 61 at Madrid. Each test consisted in measuring the time offset between two of these stations. The test provided experimenters with sufficient data to compute an "error of closure" which was used as a validity measurement of the system. Test results indicated that:

(1) Station 61 led station 41 by 9.730 msec

(2) Station 61 led station 12 by 7.638 msec

(3) Station 12 led station 41 by 2.093 msec

To facilitate comparison, these synchronization errors have been corrected to a common time (18:00 GMT on August 16, 1966). The offsets yield an error of closure of only 1 $\mu$sec.

The Naval Observatory, under contract to the Lunar Orbiter Project, circulated a cesium clock to these three network stations immediately after the ranging tests. The findings agreed with the three listed time measurements within 15.9, 6.8, and 9.6 $\mu$sec, respectively. These differences can easily be explained by the elapsed time between the two sets of measurements and the nonuniform drift rate of the rubidium frequency standards of the stations. Thus, not only did the synchronization scheme fulfill the project requirements, but it also provided a thousandfold increase in the accuracy with which the station clocks can be synchronized.

# RESULTS FROM LUNAR ORBITER I RANGING DATA

By W. L. Sjogren
Jet Propulsion Laboratory

Lunar Orbiter I was the first space probe of all lunar and planetary probes to obtain ranging data.[1] These data are extraordinary because they cover such large distances and provide such extreme precision. During the period from September 14 to October 25, 1966, well over 2000 independent ranging points were obtained, having an accuracy of approximately 10 meters. With these data it has been possible to provide an excellent check on the accuracy of the orbit determined from the Doppler data only and also to evaluate some very recent and significant changes in the lunar ephemeris. In fact, the data have confirmed that these recently incorporated changes are correct and that, with them, lunar ephemeris errors along the earth-moon line, which were on the order of 1.5 km, have been reduced by an order of magnitude.

The computation of orbits by using solely Doppler data provides very good estimates of the spacecraft position with respect to the moon; however, these data are rather insensitive to the position of the moon in space (i.e., lunar ephemeris errors). Therefore, with the spacecraft positioned with respect to the moon with only Doppler data and a lunar ephemeris positioning the moon with respect to the earth-based tracking station, a direct measurement of range to the spacecraft should close the triangle or show discrepancies which should be accounted for. The small circles in figure 67 show the discrepancies $\Delta\rho$ (i.e., residuals), between the distance calculated by using the Doppler data along with the uncorrected lunar ephemeris and the actual ranging measurement. The interesting aspect of these residuals becomes pronounced when Eckert's corrections to the lunar ephemeris[2] are displayed with them (i.e., solid line). Recently these corrections have been published as reference 1, with the purpose of improving the accuracy of the Brown Lunar Theory. He has reevaluated the transformation of coordinates from the original theory to those coordinates presently used with much more accuracy than had been done previously. The agreement with the ranging points processed to date is remarkable. Although this comparison is not directly valid, because station ranging residuals are not exactly in the same direction[3] as Eckert's corrections, it does show that Eckert's corrections are significant and are confirmed by real measurements.

---

[1] Only Mariner 64 actually carried a ranging system but the system was never activated because of reliability considerations.

[2] Eckert's corrections were computed by C. Lawson and J. D. Mullholland of the JPL Ephemeris Group.

[3] Approximately a 0.5° direction difference, causing a very small change in earth-moon line residuals.
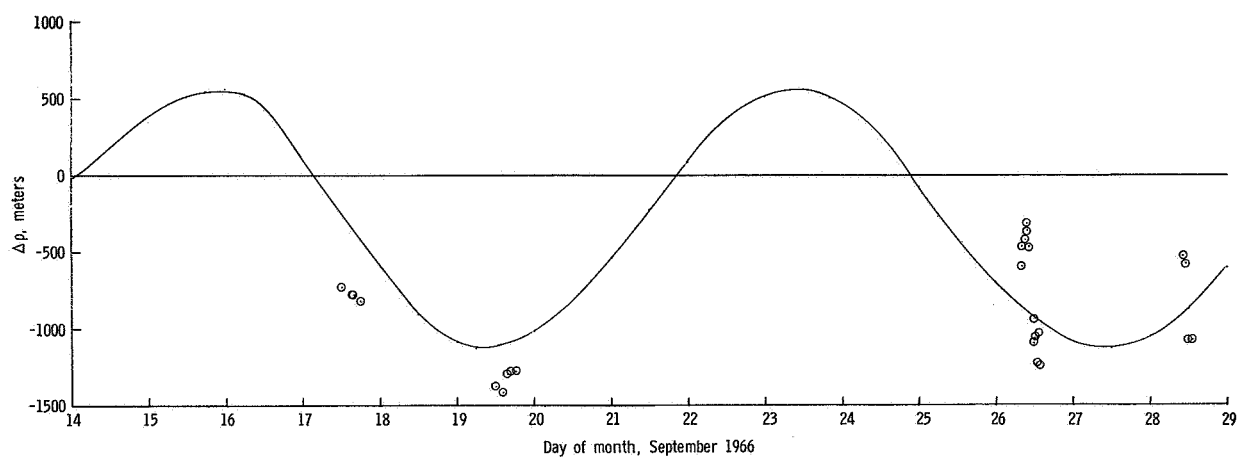
(a) September 14 to 29, 1966.
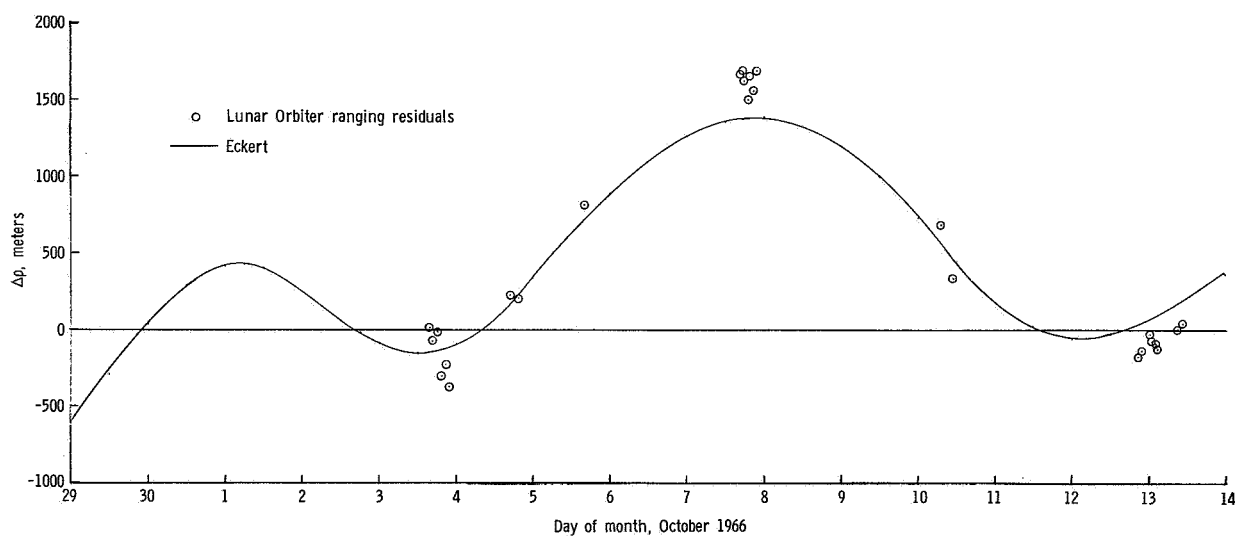
(b) September 29 to October 14, 1966.
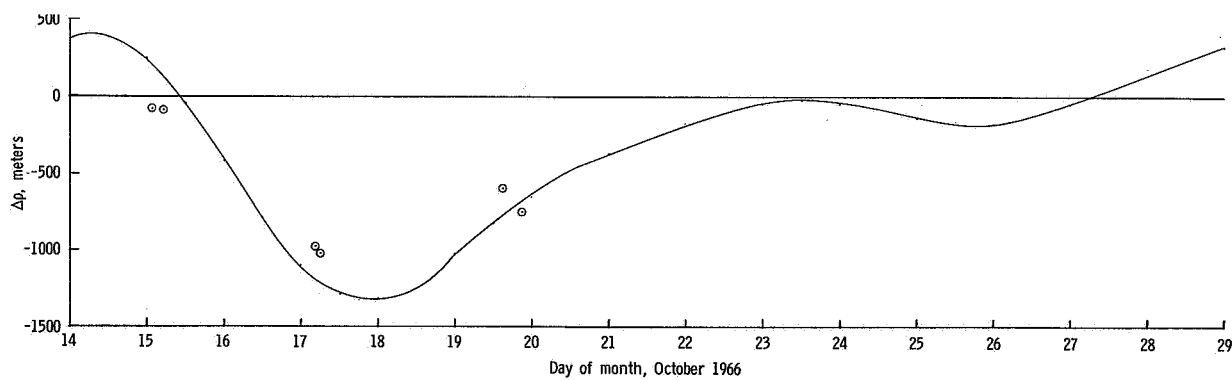
(c) October 14 to 29, 1966.

Figure 67.- Ranging-data residuals from Lunar Orbiter I compared with Eckert's radial corrections to lunar ephemeris.

104

Errors in station locations are approximately 30 meters and the selenocentric position uncertainty of the spacecraft in the earth-moon direction is approximately 100 meters due primarily to the incomplete lunar oblateness model. There is also the 4-meter resolution of the computer single-precision computation of range. Therefore, the only error large enough to remove the inconsistency is the lunar ephemeris error as indeed predicted by Eckert. The dates of September 19, October 4, October 8, and October 13 are especially interesting (figs. 67(a) and (b)) for here are the minimum, zero, maximum, and zero points, respectively, with close agreement in each case.

Since the residuals do agree well with Eckert's corrections and do not display any characteristic bias, the factor (approximately earth radius) which is used to scale the ephemeris radial component must be fairly good. This then can be converted directly into a mean earth-moon distance as described by Brouwer (ref. 2). When this is done, a value of 384 399.19 km is obtained for the mean earth-moon distance and agrees well with the value reported from the Ranger VI data and the work of B. S. Yaplee (i.e., lunar radar bounce data) as discussed in the Ranger VI report (ref. 3).

The ranging data have also confirmed the behavior of the Doppler data being used to obtain the lunar potential model. The Doppler fit is relatively poor compared with residuals obtained during the near-earth phase or during the cruise phase to the moon. Residuals on the order of 1 to 2 Hz with periodicity of 30 min are not uncommon. At one time there were doubts as to whether these effects were really there. Possibly the Doppler data were corrupted by multipath effects, temperature variations, and so forth. However, the independent ranging data points taken every 3 min during periods of systematic and high-amplitude Doppler residuals show the same behavior. For example, the ranging residuals at two time points were differenced and compared to the integrated Doppler data over the same time interval. The values agreed both in sign and magnitude (to 4 meters, the resolution of the single-precision range computation), which suggests that the oscillations of approximately 100 meters do indeed exist and that the Doppler data are correct.

# References

1. Eckert, W. J.; Walker, M. J.; and Eckert, D.: Transformations of the Lunar Coordinates and Orbital Parameters. Astron. J., vol. 71, no. 5, June 1966, pp. 314-332.

2. Brouwer, Dirk: Relations Among Some Important Astronomical Constants. The System of Astronomical Constants, J. Kovalevsky, ed., Gauthier-Villars & Cie (Paris), 1965, pp. 241-249.

3. Sjogren, W. L.; Curkendall, D. W.; Hamilton, T. W.; Kirhofer, W. E.; Liu, A. S.; Trask, D. W.; Winneberger, R. A.; and Wollenhaupt, W. R.: The Ranger VI Flight Path and Its Determination From Tracking Data. Tech. Rept. No. 32-605 (Contract No. NAS7-100), Jet Propulsion Lab., California Inst. Technol., Dec. 15, 1964.

# LUNAR RADIUS DETERMINED FROM THE V/H SENSOR EXPERIMENT

By John F. Newcomb, William R. Wells,
and G. Calvin Broome
Langley Research Center

## INTRODUCTION

The data generated by the image-motion compensator of the photographic subsystem of the Lunar Orbiter have been analyzed to determine the local lunar radii at various points. These radii were then used to infer a lower datum plane in the vicinity of the Apollo area of interest than had previously been assumed. The results of this analysis are presented herein.

## V/H SENSOR DESCRIPTION, OPERATION, AND VALIDATION

The primary task of the image-motion compensator, generally referred to as the V/H sensor, is to determine and supply to the photographic subsystem accurate information regarding the motion of the photographic image in the camera focal plane. This information is used to regulate the film platen drive so that the image motion relative to the film is minimized. The sensor also times the camera shutter operation for proper forward picture overlap. The feature of the V/H sensor which enables lunar radii determination is the information it contains regarding the spacecraft speed and altitude relative to the local lunar surface. This information, with an accurate knowledge of the position and velocity of the spacecraft obtained from orbit determination calculations, is sufficient for a solution for a local radius.

Prior to using the data to determine the local lunar radii, it was necessary to determine that the sensor was operating properly. This can normally be done by two means. The first is to determine that the smear in the photographs is below some limit and thus determine that the sensor was operating within an equivalent tolerance. The second is to measure the overlap on successive photographs. Because the high-resolution camera was not operating properly, the medium-resolution photographs were the only data available for measuring smear. These photographs do not afford an accurate enough data source for the smear measurements required. With subsequent Lunar Orbiter flights the high-resolution photographs will afford a good data source from which to infer the V/H sensor operational accuracy. In the absence of the high-resolution photographs, the forward overlap on subsequent frames was measured. From these measurements it appears that there was possibly a bias in the sensor that could account for approximately 1 km of the observed 1.9-km datum-plane difference. However, more Lunar Orbiter flights will be required before this can be determined.

# DETERMINATION OF THE LUNAR RADIUS

A number of sample readings from the V/H sensor were taken just prior to and during photography of each of the primary sites as given in table III. The V/H readings used in the determination of the local lunar radii were chosen so that the sensor was viewing a relatively smooth lunar terrain. In order to choose the usable V/H readings, the ACIC lunar topographical charts were used. These charts give the relative elevations in various areas on the lunar surface and are considered to be accurate to within 100 meters. However, the absolute elevations or datum plane on which these charts are based is difficult to measure in the vicinity of the lunar prime meridian, and it is in this area that the Lunar Orbiter V/H readings were obtained. Therefore, a discrepancy between the Lunar Orbiter local lunar radius and that obtained from the charts is considered to reflect directly into a datum-plane difference.

The actual computations of the local lunar radii were carried out in the following manner. The local velocity and radius of the spacecraft at the time of the readings were computed with the use of the orbit determination program. These values are used with the V/H readings in the following equation to compute the local lunar radius $R_L$ at the point viewed by the V/H sensor.

$$R_L = \sqrt{\left(\frac{v}{K \cos(\theta + \phi)}\right)^2 - \frac{2vr}{K} + r^2}$$

where

$$K = \frac{V}{H} \frac{\cos^2\theta}{\cos(\theta + \phi - \gamma)\cos(\theta + \phi)}$$

In these expressions, $\theta$ is the forward look angle of the V/H sensor measured from the camera optical axis and has an average value of $8^\circ$. The tilt $\phi$ of the camera optical axis from the local vertical is measured in the orbital plane. For the V/H readings used, the tilt angle $\phi$ varies between $3^\circ$ and $-3^\circ$. The symbol $v$ represents the spacecraft velocity, $r$ represents the radial distance from the center of the moon to the spacecraft, and $\gamma$ represents the flight-path angle. The symbol V/H represents the V/H sensor output.

The results of the analysis are shown in table III. The first column in the table presents the site for which the photographic pass was being made. Also shown are the lunar latitudes and longitudes of the points which were being sampled by the V/H sensor when the readings were taken. For each of these points the local lunar radius, as determined from the Lunar Orbiter data and as determined by the ACIC, is presented. In order to obtain the most recent information on local lunar radii, as determined by ACIC, the latitudes and longitudes of the V/H sample points were given to Donald Myer of the Lunar

Control Section ACIC, and the ACIC local radius measurements in the table represent his determinations. Also shown in the table is the difference between the local lunar radii as determined by the two methods. In all cases the Lunar Orbiter radius values are lower than the corresponding ACIC-determined values. The mean difference is 1.9 km with a standard deviation of 0.5 km.

It is interesting to compare the above results with those reported in reference 1 concerning the local lunar radii as determined by the flight data of Rangers VI to IX. The results of this determination are given in table IV. For each Ranger impact point, the selenographic latitude and longitude are given as well as the local lunar radii as determined by ACIC. The local radii determined by the Ranger series reflect the same results as does the V/H sensor experiment; that is, a datum plane in the proximity of the Apollo area of interest about 2 km lower than has previously been determined.

REFERENCE

1. Sjogren, W. L.; Trask, D. W.; Vegos, C. J.; and Wollenhaupt, W. R.: Physical Constants as Determined From Radio Tracking of the Ranger Lunar Probes. Tech. Rept. 32-1057 (Contract No. NAS 7-100), Jet Propulsion Lab., California Inst. Technol., Dec. 30, 1966.

TABLE III.- LOCAL LUNAR RADII AS DETERMINED BY THE ACIC AND AS
MEASURED BY LUNAR ORBITER V/H SENSOR

| Site | V/H point | | Local lunar radius, km | | Radius difference, km |
|------|-----------|-----------|-----------------|-----------|------------|
| | Latitude | Longitude | From V/H sensor | ACIC value | |
| A-1 | 0°33' S | 40°20' E | 1735.3 | 1737.5 | 2.2 |
| A-1 | 0°52' S | 41°46' E | 1735.6 | 1737.5 | 1.9 |
| A-3 | 1°10' N | 23°05' E | 1734.7 | 1737.5 | 2.8 |
| A-3 | 0°50' N | 24°36' E | 1734.7 | 1737.3 | 2.6 |
| A-3 | 0°30' N | 26°04' E | 1734.9 | 1737.1 | 2.2 |
| A-3 | 0°10' N | 27°34' E | 1734.9 | 1737.0 | 2.1 |
| A-5 | 0°20' N | 2°48' W | 1736.5 | 1739.3 | 2.8 |
| A-5 | 0°01' N | 1°28' W | 1736.6 | 1739.2 | 2.4 |
| A-6 | 3°31' S | 3°49' W | 1736.8 | 1738.5 | 1.7 |
| A-7 | 3°18' S | 22°41' W | 1736.1 | 1738.0 | 1.9 |
| A-7 | 3°36' S | 21°21' W | 1736.5 | 1738.1 | 1.6 |
| A-8.1 | 2°46' S | 37°45' W | 1735.5 | 1737.7 | 2.2 |
| A-8.1 | 3° 8' S | 35°59' W | 1735.8 | 1737.7 | 1.9 |
| A-9.2a | 1°32' S | 45°27' W | 1735.8 | 1736.8 | 1.0 |
| A-9.2a | 1°52' S | 43°56' W | 1735.6 | 1737.4 | 1.8 |
| A-9.2a | 2°12' S | 42°30' W | 1736.3 | 1737.7 | 1.4 |
| A-9.2b | 1°43' S | 46°19' W | 1735.5 | 1736.7 | 1.2 |
| A-9.2b | 2° 5' S | 44°49' W | 1735.4 | 1736.9 | 1.5 |
| A-9.2b | 2°27' S | 43°20' W | 1736.0 | 1737.4 | 1.4 |

TABLE IV.- LOCAL LUNAR RADII DETERMINED FROM RANGER IMPACT DATA

| Mission | Impact point | | Local lunar radius, km | | Radius difference, km |
|---------|-----------|-----------|---------------------|-----------|------------|
| | Latitude | Longitude | From Ranger flight data | ACIC value | |
| Ranger VI | +9.3 | +21.4 | 1735.3 | 1737.4 | 2.1 |
| Ranger VII | -10.7 | -20.7 | 1735.5 | 1737.7 | 2.2 |
| Ranger VIII | +2.7 | -24.8 | 1735.2 | 1737.2 | 2.0 |
| Ranger IX | -12.9 | -2.4 | 1735.7 | 1737.9 | 2.2 |

# METEOROID MEASUREMENT EXPERIMENT

By Charles A. Gurtler
Langley Research Center

Estimates of the meteoroid penetration hazard in the vicinity of the moon have varied by several orders of magnitude (ref. 1). These estimates have ranged from somewhat less than near-earth flux to several orders of magnitude greater than near-earth flux. One of the major factors giving rise to this uncertainty is the question of how many secondary meteoroids may be created by primary-meteoroid impacts on the lunar surface.

The Lunar Orbiter spacecraft is instrumented with pressurized-cell meteoroid detectors like the ones flown on the Explorers XIII, XVI, and XXIII. Figure 68 is a drawing of this detector, which consists of a pressure-tight container with a pressure-sensitive switch. The test material is an integral part of the pressurized container. The detector design is such that gas pressure holds the switch in a closed position. When the pressure is released by a puncture in the container, the switch returns to an open position and stays in this position. The open switch then becomes a means of permanently storing the fact that the puncture has occurred. This switch position is telemetered. Each time the telemetry reads out the status of the detectors, it indicates any new punctures and, at the same time, verifies all previously indicated punctures.

The experiment consists of 20 pressurized-cell detectors with an exposed area of approximately 0.186 meter$^2$ (2 ft$^2$). The test material is 0.0254-mm beryllium copper, which is the same material as that flown on Explorer XVI.

The location of the detectors on the spacecraft is shown in figure 5. The detectors on Lunar Orbiter I were exposed to the space environment for 80 days and there were no penetrations. If the detectors had experienced the same penetration rate as that measured in the near-earth environment (refs. 2 and 3), a puncture would have been expected approximately every 2 weeks. If the puncture rate had been an order of magnitude greater than in the near-earth environment, a puncture would have been expected every day or two.

Figure 69 is a plot of puncture rate as a function of thickness for beryllium copper. The plot shows the upper 95-percent confidence limit of the penetration rate obtained from the Lunar Orbiter for the 80 days. For comparison it shows the average puncture rates measured in the near-earth environment from the Explorers XVI, XXIII, and Pegasus meteoroid experiments, and the Whipple 1963 estimated flux. The Explorer XXIII experiment measured penetration rates in stainless steel, and the Pegasus measurements were obtained in aluminum. The results of these experiments have been tentatively interpreted in terms of beryllium copper for plotting in figure 69.

The results of the experiment for the 80 days indicate that in the lunar environment experienced by the Lunar Orbiter the most probable penetration rate for 0.0254-mm beryllium copper is less than the near-earth measured rate. Since no penetrations occurred, a penetration rate was not established. However, the uncertainty of the penetration rate in the vicinity of the moon has been narrowed by several orders of magnitude.

## REFERENCES

1. Gault, Donald E.; Shoemaker, Eugene M.; and Moore, Henry J.: Spray Ejected From the Lunar Surface by Meteoroid Impact. NASA TN D-1767, 1963.

2. Hastings, Earl C., Jr., compiler: The Explorer XVI Micrometeoroid Satellite – Supplement III, Preliminary Results for the Period May 27, 1963, Through July 22, 1963. NASA TM X-949, 1964.

3. O'Neal, Robert L., compiler: The Explorer XXIII Micrometeoroid Satellite – Description and Preliminary Results for the Period November 6, 1964 Through February 15, 1965. NASA TM X-1123, 1965.

0.30

18.80

A　　　　A

Pinch-off
tube

3.71

Stainless-steel
test material

Pressure
diaphragm

2.46

Microswitch

Section A-A
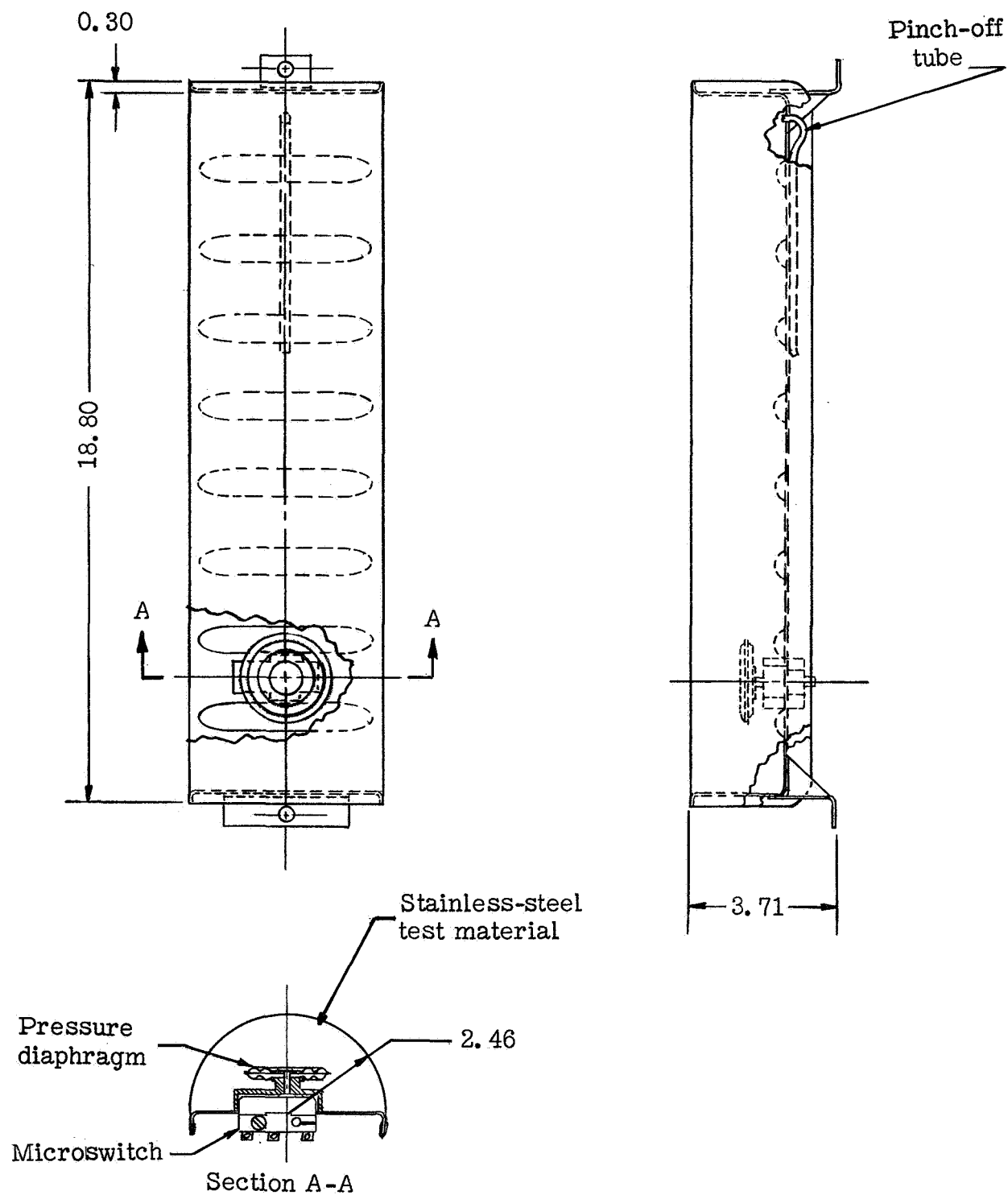
Figure 68.- Pressurized-cell detector. All dimensions are in centimeters.

113
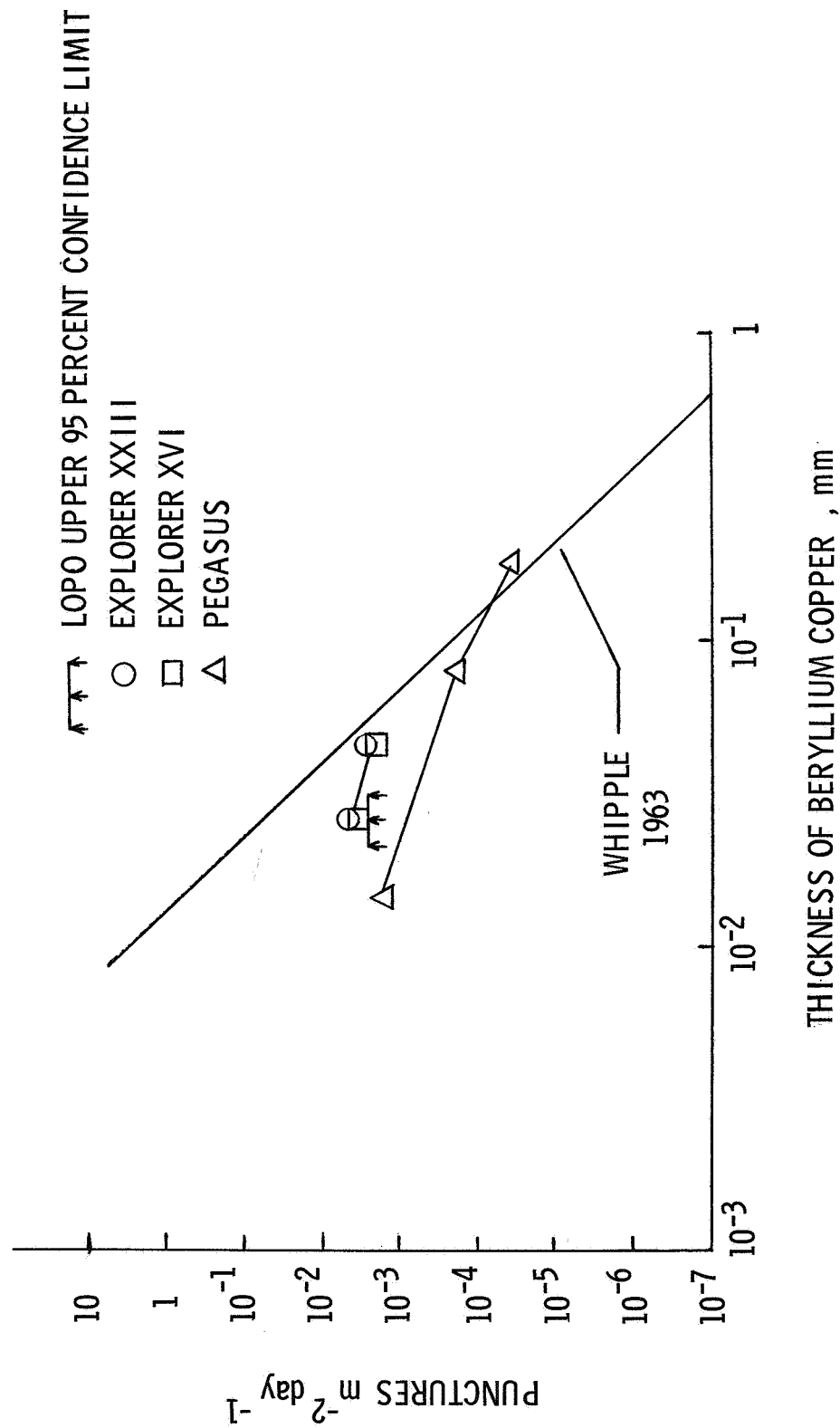
Figure 69.- Puncture rate as function of thickness of beryllium-copper sheet.

114

# RADIATION MEASUREMENTS

By Trutz Foelsche
Langley Research Center

The Lunar Orbiter spacecraft is equipped with two scintillator dosimeters which measure dose rates in thin cesium iodide crystals behind aluminum shielding. The instruments are designed and positioned to derive the dose to which the film in the photographic subsystem cassette and the loopers is exposed during solar events.

## RADIATION-DOSAGE MEASUREMENT SYSTEM

A simplified block diagram of the measurement system is given in figure 70. Two scintillation-counter dosimeters and associated logic are used for this purpose. Each dosimeter is constructed of a cesium iodide crystal, a light pipe, photomultiplier tube, output pulse signal conditioners, and associated power supplies. The crystals are shielded
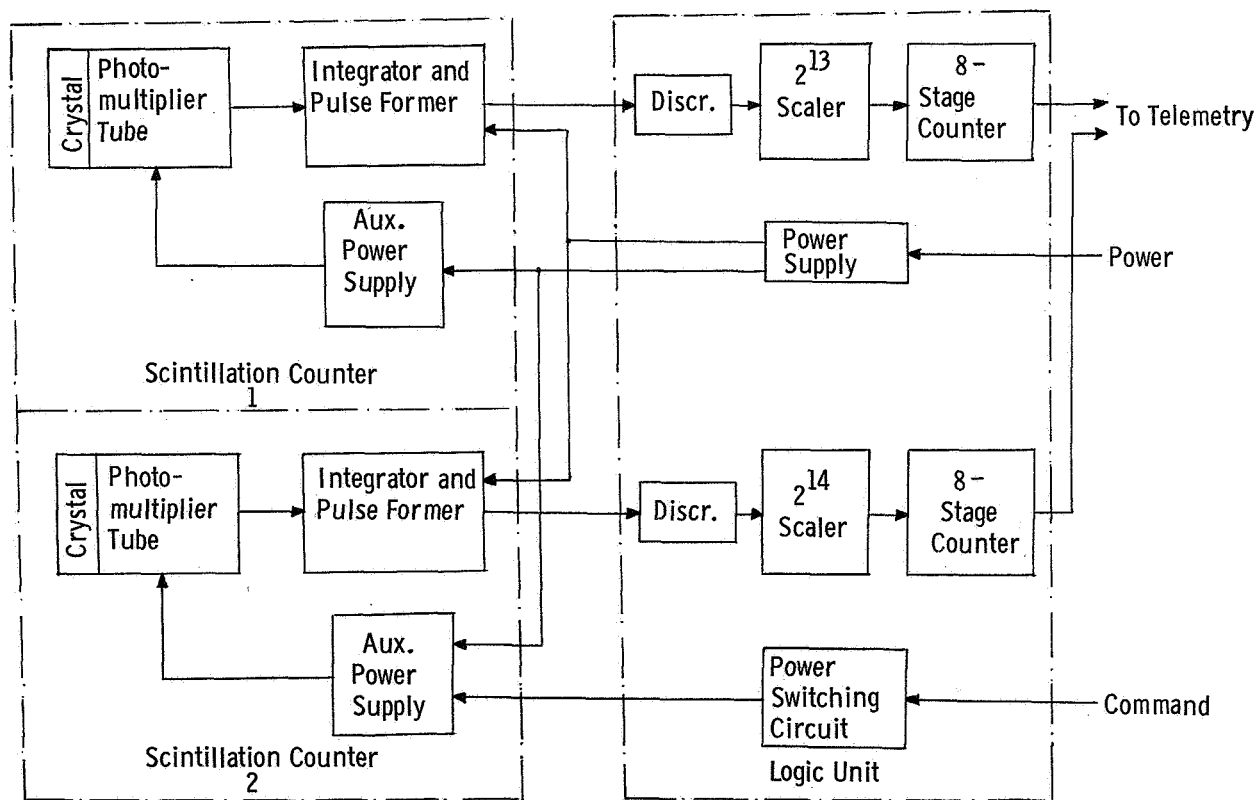


Figure 70.- Radiation-dosage measurement system.

115

and positioned to simulate the shielding of the film in the cassette and in the loopers. The differences between the two dosimeters are given in the following table:

| Dosimeter | Aluminum shielding, grams/cm$^2$ | Output sensitivity, rad/count | Approximate field of view with specified shielding, sr |
|---|---|---|---|
| Unit 1 (Film cassette) | 2.0 | 0.25 | 1/2 of $4\pi$ |
| Unit 2 (Film loopers) | .14 | .50 | 2/3 of $4\pi$ |

The detection function is initiated when radiation of sufficient energy to penetrate the shield is absorbed in the crystal. This causes the crystal to emit light which is proportional to the absorbed energy. The photomultiplier tube produces a current proportional to the light flux. The total dosage is measured by integrating the current in the signal-conditioning circuit. When a given level is attained in the integrator, an output pulse is generated. The output of this device is 6.37 pulses/sec for an input dose rate of 0.7 rad/hr. The saturation dose rate for the instrument is 0.025 rad/sec (90 rad/hr) for unit 1 and 0.05 rad/sec (180 rad/hr) for unit 2.

The output pulses are accumulated in binary counters (21 stage for unit 1 and 22 stage for unit 2). The 8 bits representing the highest count are telemetered. The effect of this is to divide the output of unit 1 by $2^{13}$ and unit 2 by $2^{14}$. The accumulated dose for unit 1 is 63.75 rads and for unit 2 is 127.5 rads, before recycling. Readout of both units occurs once for each telemetry frame. A flight programer command is provided to turn the photomultiplier-tube power supply on for unit 2.

## PRELIMINARY RESULTS

During passage through the earth radiation belts near the equatorial plane, a dose of approximately 1 rad accumulated in dosimeter 1 (2 grams/cm$^2$ shielding). The lightly shielded dosimeter 2 was turned off during passage of the belts to prevent saturation.

At transition to the moon and during the first 13 days in orbit around the moon at quiet sun, a dose rate of 0.5 to 1 mrad/hr was measured in both dosimeters. These dose rates are obtained by subtracting the equivalent dose rates produced by the dark currents of the multipliers, which are in the same order of magnitude.

A dose rate of 0.5 to 1 mrad/hr corresponds to that produced by galactic cosmic rays. The measurement of this dose rate in the immediate environment of the moon indicates that, during solar quiet times, the gamma and charged-particle albedo and activity of the moon produce a lower dose rate than galactic cosmic rays.

116

During the series of six flares of class II or greater in the week from August 28 to September 4, 1966, the doses in the dosimeters increased to 10 rad and 137 rad, respectively, shown in figure 71. The dose rates as functions of time exhibited two peak groups, as shown in figure 72. The lower peaks (10 and 70 mrad/hr) occurred after the flare of August 28, 1966 (flare III bright, 1527 to 1730 GMT, N20E10) and the higher peaks (0.7 and 7 rad/hr) after the flare of September 2, 1966 (flare II, 0528 GMT, several hours duration, N22W63).

From a preliminary synopsis of riometer, Pioneer VII, and Lunar Orbiter dosimeter data, it seems that the larger proton event of September 2, 1966, was of moderate size (approximately $10^8$ p/cm$^2$ at 30 MeV) with the shape of its particle number spectrum similar to that of the event of July 18, 1961.

The event occurred 3 days after completion of the photographic mission. If it had occurred during the photographic mission, no deviation from a normal schedule (when undeveloped film stays in the loopers for not more than 2 hours) would have been necessary since the EK-SO-243 film is insensitive to radiation doses on the order of 10 to 20 rad (a density increase of approximately 0.05 over base density of 0.30).
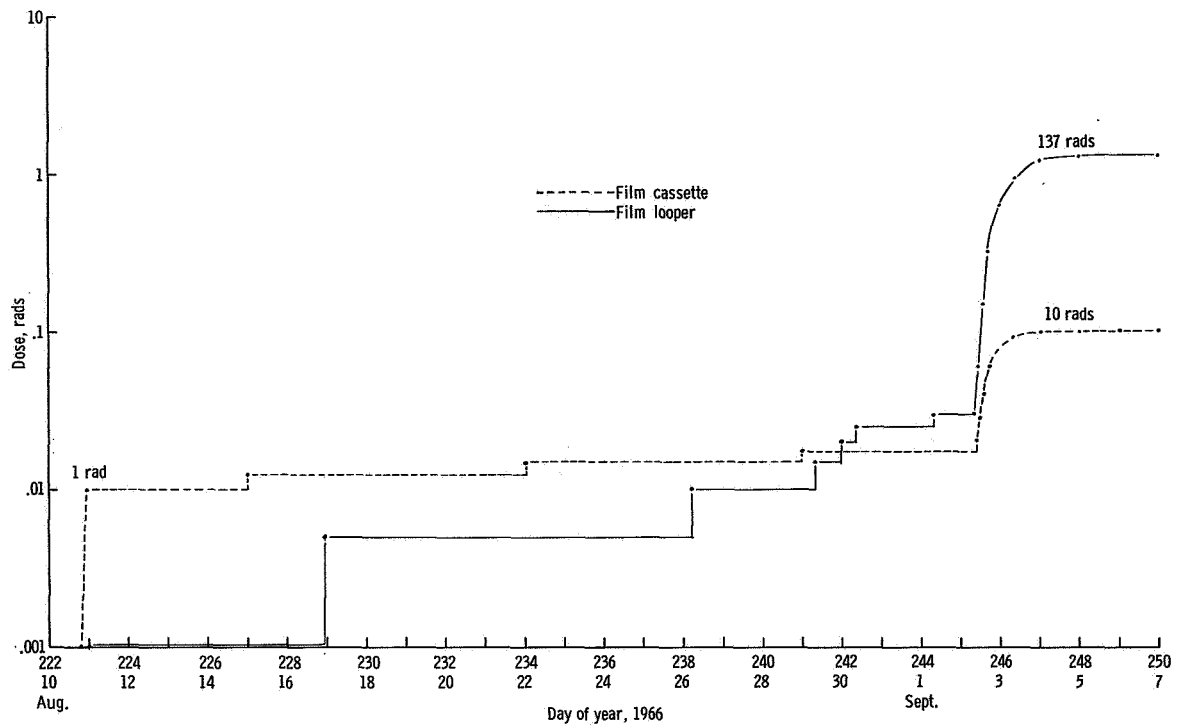
Figure 71.- Total radiation measured during Lunar Orbiter I photographic mission.
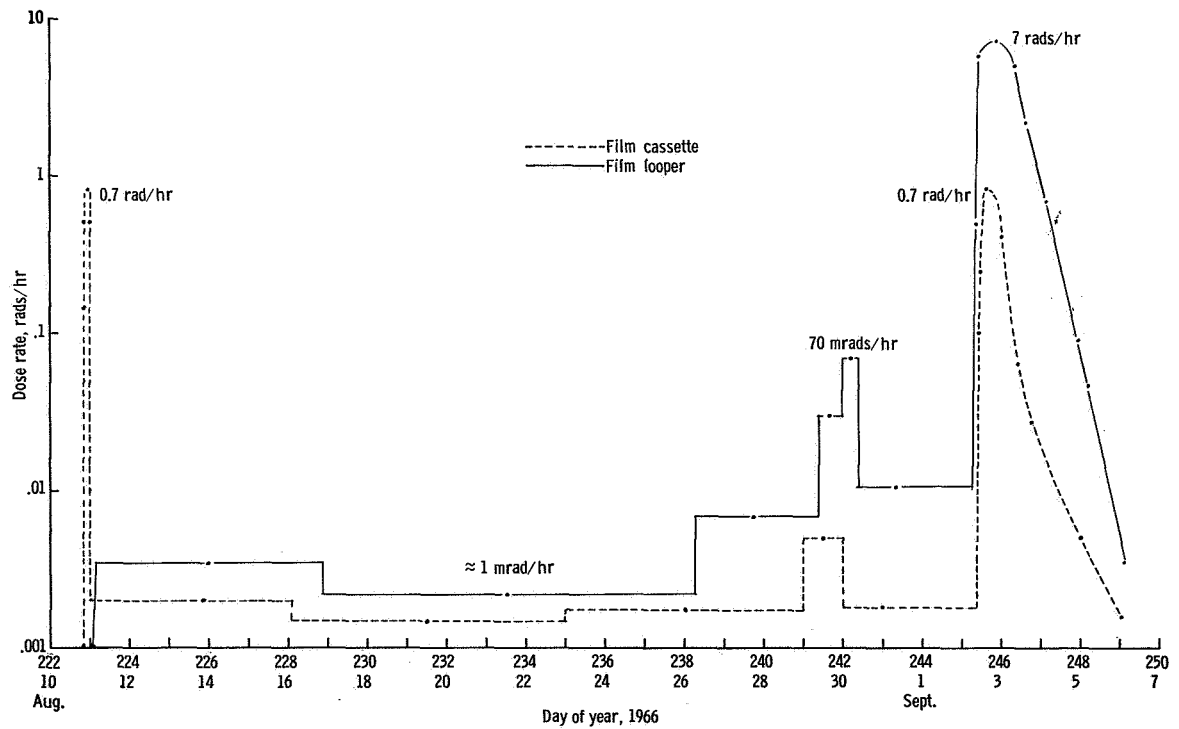


Figure 72.- Radiation dose rate for Lunar Orbiter I flight.

118

APPENDIX – PHOTOGRAPH INDEXES, GEOLOGIC TERRAIN MAPS,
AND EXPLANATION OF GEOLOGIC FEATURES

APPENDIX

NORTH

SOUTH

Terminator positions are indicated at those sites for which the terminator falls within the site footprint.

LEGEND

☐ Medium Resolution Coverage

⊡ High Resolution Coverage

⊢ Terminator Limit

PREPARED UNDER THE DIRECTION OF THE DEPARTMENT OF DEFENSE BY THE AERONAUTICAL CHART AND INFORMATION CENTER, UNITED STATES AIR FORCE FOR THE NATIONAL AERONAUTICS AND SPACE ADMINISTRATION.

Base Chart Compiled ACIC February 1968
Lithographed by ACIC 3-69

Map 1

122

# LUNAR ORBITER I PHOTOGRAPHIC COVERAGE

| Site | Exposure Number(s) |
|------|--------------------|
| IP-1 | 52, 53, 54, 55, 56, 57, 58, 59, 60, 61, 62, 63, 64, 65, 66, 67 |
| IP-2 | 68, 69, 70, 71, 72, 73, 74, 75, 76, 77, 78, 79, 80, 81, 82, 83 |
| IP-3 | 85, 86, 87, 88, 89, 90, 91, 92, 93, 94, 95, 96, 97, 98, 99, 100 |
| IP-4 | 105, 106, 107, 108, 109, 110, 111, 112 |
| IP-5 | 118, 119, 120, 121, 122, 123, 124, 125, 126, 127, 128, 129, 130, 131, 132, 133 |
| IP-6 | 141, 142, 143, 144, 145, 146, 147, 148 |
| IP-7 | 157, 158, 159, 160, 161, 162, 163, 164, 165, 166, 167, 168, 169, 170, 171, 172 |
| IP-8 | 176, 177, 178, 179, 180, 181, 182, 183 |
| IP-9.2a | 184, 185, 186, 187, 188, 189, 190, 191, 192, 193, 194, 195, 196, 197, 198, 199 |
| IP-9.2b | 200, 201, 202, 203, 204, 205, 206, 207, 208, 209, 210, 211, 212, 213, 214, 215 |
| IS-1 | 5, 6, 7, 8, 9, 10, 11, 12, 13, 14, 15, 16, 17, 18, 19, 20, 21, 22, 23, 24 |
| IS-2 | 25, 26, 27 |
| IS-3 | 28, 30, 35, 36, 37, 38, 39, 40 |
| IS-4 | 29, 33, 34 |
| IS-5 | 31, 32, 44 |
| IS-6 | 41, 50, 51 |
| IS-7 | 42, 46, 47, 48, 49 |
| IS-8 | 84 |
| IS-9 | 102, 115, 116, 117, 136 |
| IS-10 | 103 |
| IS-12 | 113, 114 |
| IS-13 | 134, 135 |
| IS-14 | 137, 139, 140 |
| IS-15 | 138 |
| IS-16 | 149, 151 |
| IS-17 | 150 |
| IS-18 | 153, 154, 155, 156 |
| IS-19 | 173 |
| IS-20 | 174 |
| IS-21 | 175 |

Medium resolution and high resolution frame pairs exist for each exposure. However all the high resolution frames are degraded (smeared) except for the following exposures for which the high resolution frames are not degraded: 26, 27, 29, 30, 31, 36, 38, 40, 41, 42, 102, 115, 117, 136

Map 1.- Lunar Orbiter 1 photograph index.
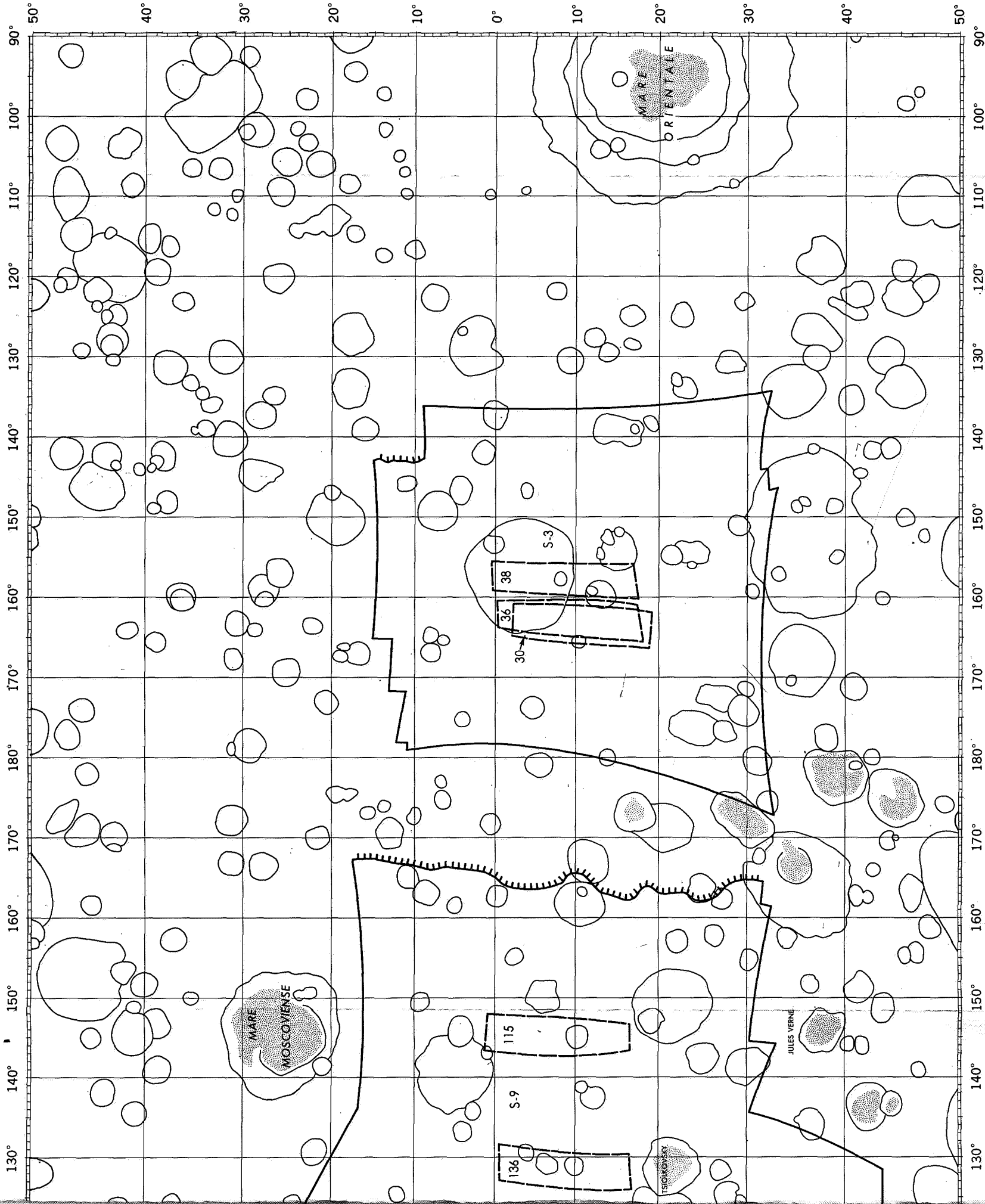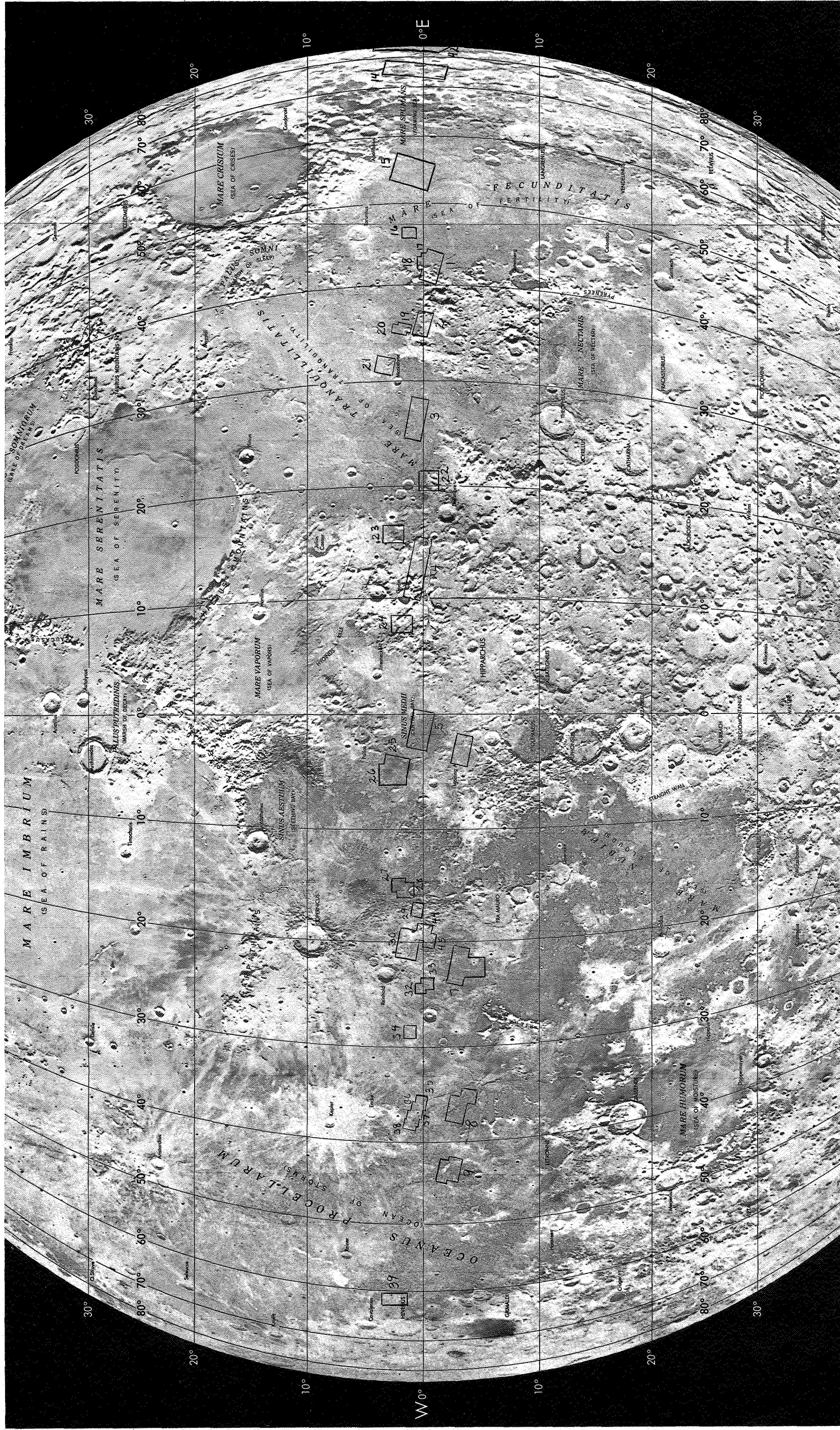
Map 2.— Lunar Orbiter 1 photograph index of near side of moon.

Map 2

123
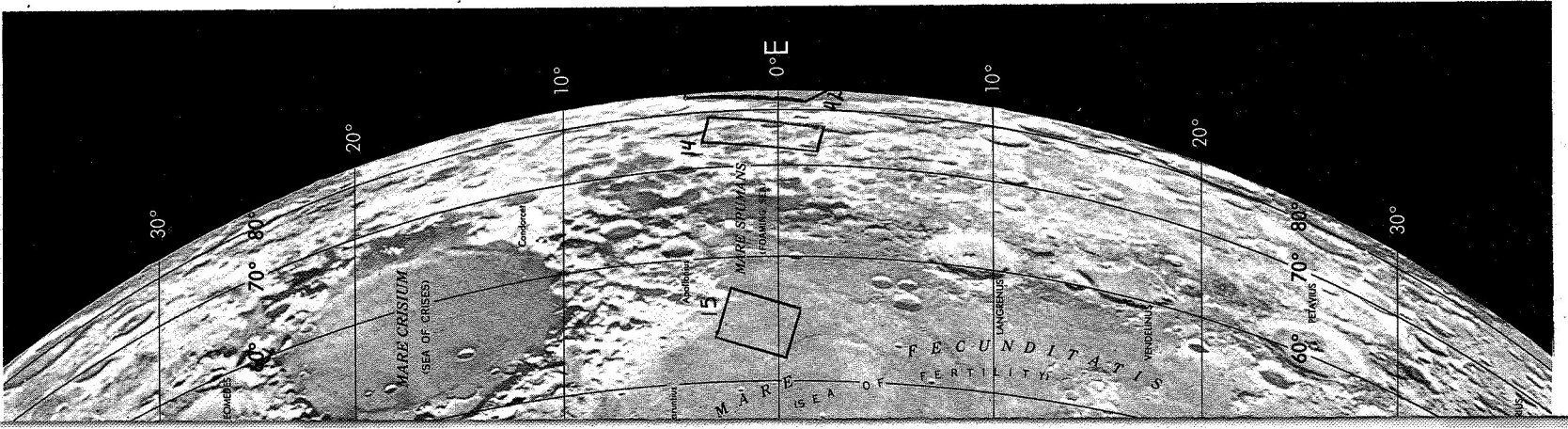
# APPENDIX

## EXPLANATION OF GEOLOGIC FEATURES

### SITE A-1

### Mare (I)

I-A    Regional mare, undifferentiated; moderately cratered and uniform.

### Upland (II)

II-B    Upland, hummocky; cratered upland bordering the mare on west.
Moderate relief and slopes.

II-B$_1$    Upland, terrace; at base of steep slopes, probably talus formed by mass-wasting.

### Craters (III)

III-A    Crater, well formed

III-A-1    Crater wall, slopes generally >15$^O$ and moderately smooth.

III-A-1a    Crater wall, slopes irregular due to presence of terraces, slump blocks and rubble but generally >15$^O$. Usually associated with bright rim craters (III-A-3c).

III-A-2    Crater floor; horizontal to subhorizontal, apparently smooth areas.

III-A-3    Crater rim; slightly hummocky on larger craters with a convex-upward profile.

III-A-3c    Crater rim; bright halos and rays.

III-B    Crater; modified and subdued. Large destroyed crater in mare identified from earth-based photography.

III-B-1    Crater wall; usually smooth and subdued with slopes <15$^O$.

III-B-2    Crater floor; relatively broad, smooth areas.

III-B-3    Crater rim; subdued and relatively smooth.

### Structural Features (IV)
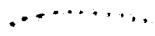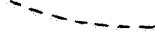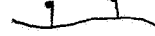
IV-A    Ridge; low broad, generally linear features.

IV-B    Domes; isolated domes and cones on mare, many have central pits.

IV-C-1    Linear rill; shallow depression with rounded cross section except where bounded by steep fault escarpments.

IV-G      Depression; irregular depressions with low, incomplete rims and a few coalescent, subdued.

IV-H      Chain craters; linear to curvilinear chains of shallow, subdued craters without rims or with subdued rims.

                Contact

                Contact; inferred

                Contact; transitional

                Mare ridge crest

                Fault; bar and ball on downthrown side; dashed if inferred

                Lineament; fracture, indistinct fault or chain crater

#2
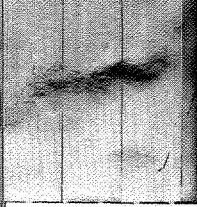
Map 3.- Preliminary geologic terrain map of site A-1. Analysis by Terry Offield, U.S. Geological Survey.

B



SITE A-1

SCALE
KILOMETERS
NAUTICAL MILES

N

Map 3

125
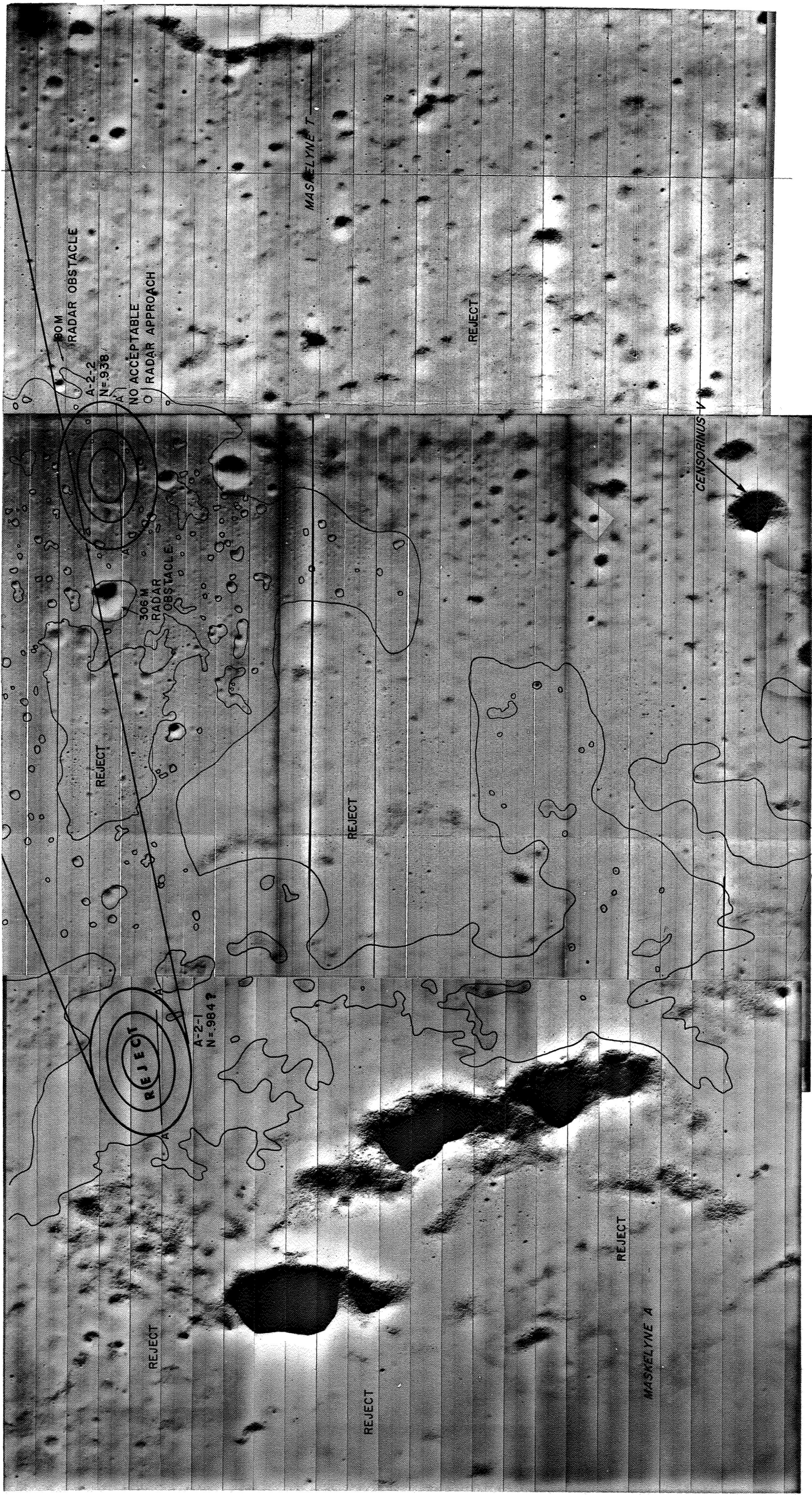
Map 4.- Terrain features of site A-2. Ellipses illustrate terrain suitability for manned landings.

2

# SITE A-2

SCALE

KILOMETERS

NAUTICAL MILES

SUN ELEV. = 24.1°



ELYNE T

Map 4

127
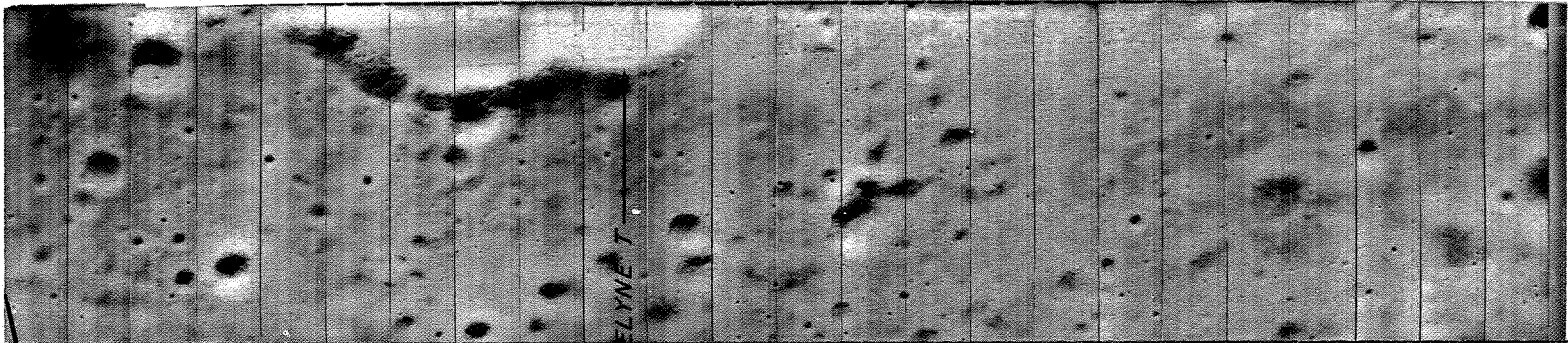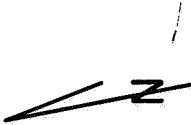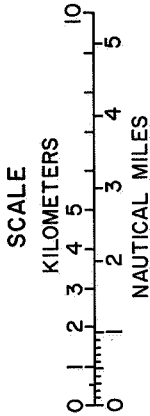
## APPENDIX

## EXPLANATION OF GEOLOGIC FEATURES

## SITE A-3

### Mare (I)

I-A      Mare, undifferentiated; low plain with numerous small craters. Mare subdivided into three units according to increasing variation in crater density and size: I-A-R, I-A-1, and I-A-2.

### Craters (III)

III-A      Well-formed craters; craters range in diameter from 5 km to the limit of resolution (0.030 km). Sabine E, the largest crater, is 5 km in diameter and 0.790 km deep (AIC Chart 60C). Smallest pits resolvable are approximately 25 meters wide and 5 meters deep.
Only well-formed craters, more than 1 km in diameter, are differentiated on map. Crater components: wall, floor, mound, and rim are not differentiated.

III-C      Crater fields; craters are generally subdued. Craters may be partly overlapping or separate but closely spaced.

### Structural Features (IV)

IV-A      Ridges; discontinuous, en echelon, linear to curvilinear, 5 km to 40 km long and 0.5 km to 5 km wide. Commonly bounded by faults and steep walls with locus of small hills and domes. Asymmetrical, with gentle northeast slopes and steep southwest slopes. Tumuli or rounded, ropy ridges, perhaps lava tubes, repeat ridge morphology at the 1.0- to 0.1-km scale.
Generally smoother than surrounding mare. Intermontane plain between ridge blocks, more densely cratered than ridge.

IV-B      Domes; hills, from 15 to 100 meters high, usually, although not always, located at the tapering end of ridges. Some slump terracettes along slopes.

     IV-B-1      Isolated boulders or blocks on the lunar surface.

IV-C-1      Rills (rima); linear in mare; generally bounded by clearly defined walls. Relatively straight or gently curved trenches, bounded by steep to precipitous walls.

#1

IV-G    Depressions, irregular; irregular in plan; walls are abrupt or subdued and gently sloping.

Generally less densely cratered than surrounding area.

⌒⌒⌒ Contact

⌒ ‒ ‒ Contact, approximately located

⌒⌒ Faults, ball and bar on downthrown side

⌒⌒ Rill

#2
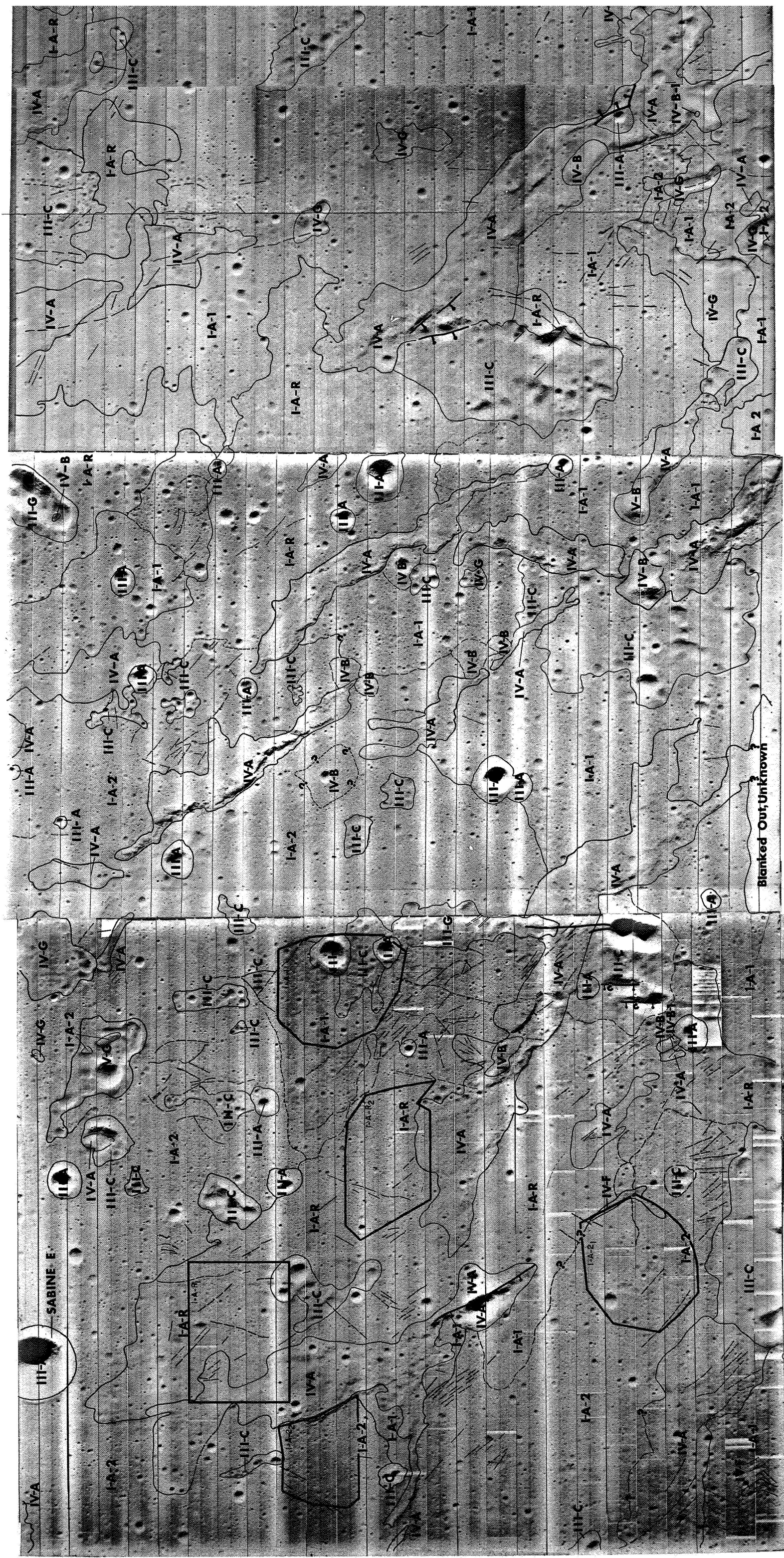
Map 5. - Preliminary geologic terrain map of site A-3. Analysis by Maurice J. Grolier, U.S. Geological Survey.

2



SITE A-3

SCALE

KILOMETERS

NAUTICAL MILES

N

Map 5

129

# APPENDIX

## EXPLANATION OF GEOLOGIC FEATURES

### Site A-4

#### Upland (II)

II-A    Upland, plains; relatively flat topography but densely cratered. The unit occupies a large structural depression between sculptured upland ridges. Although grossly similar to mare in surface characteristics, the upland-plains surface has a higher albedo and crater density than average mare samples.

II-C    Uplands, sculptured; hummocky and cratered with moderate to steep slopes.

#### Crater (III)

III-A    Craters, well-formed; many have conical or domical hills on floor.

III-A-1    Crater, walls; undifferentiated

III-A-3    Crater, rims; undifferentiated

〳    Contact

– – – –    Lineaments, straight to curvilinear features that may represent fractures or depressions, ridges, and chain craters below the limit of photographic resolution.

⊥⊥⊥    Fault or flow front in unit II-A



SITE-A-4
SCALE
KILOMETERS
0 1 2 3 4 5 6 7 8 9 10
0 1 2 3 4 5
NAUTICAL MILES

N
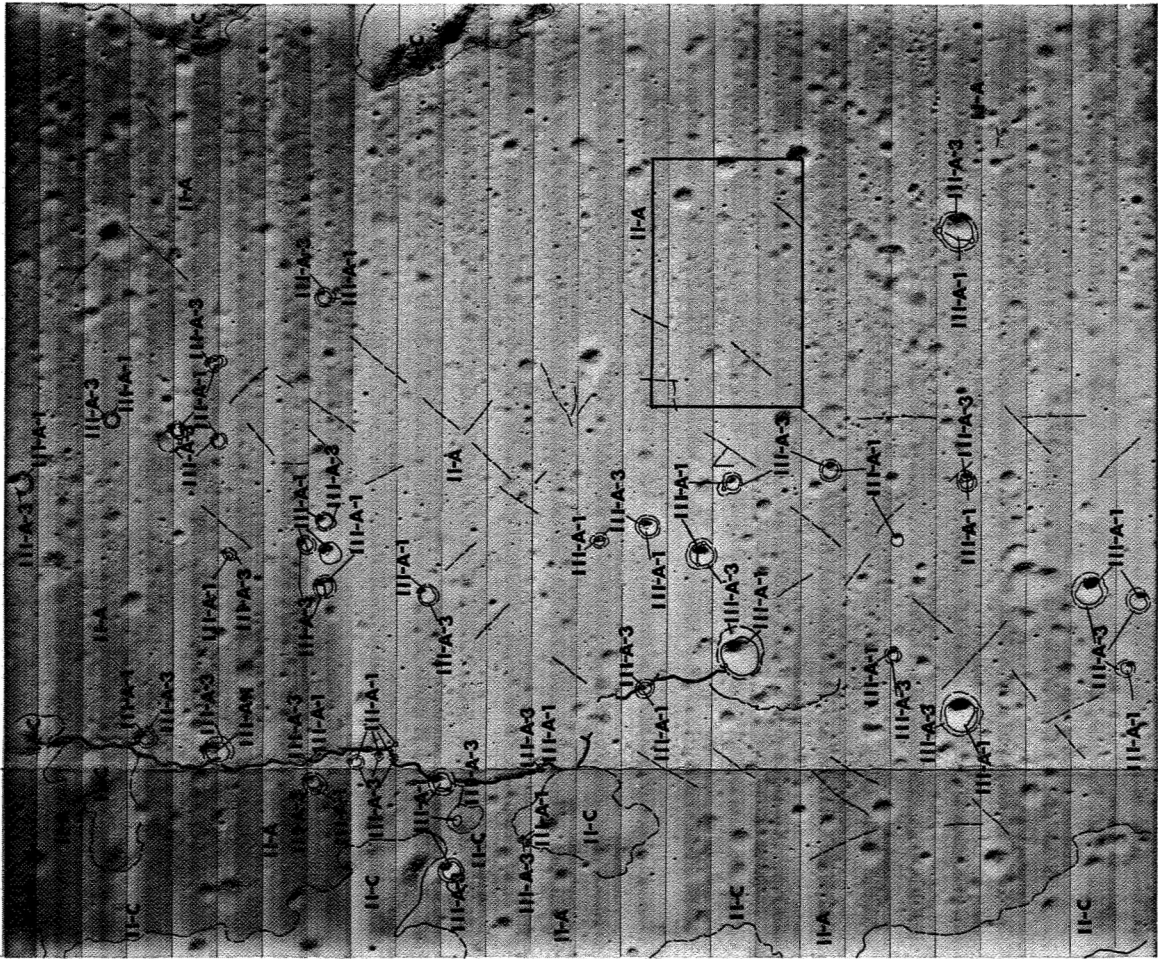
Map 6.- Preliminary geologic terrain map of frame M-107 of site A-4. Analysis by Thor N. V. Karlstrom, U.S. Geological Survey.
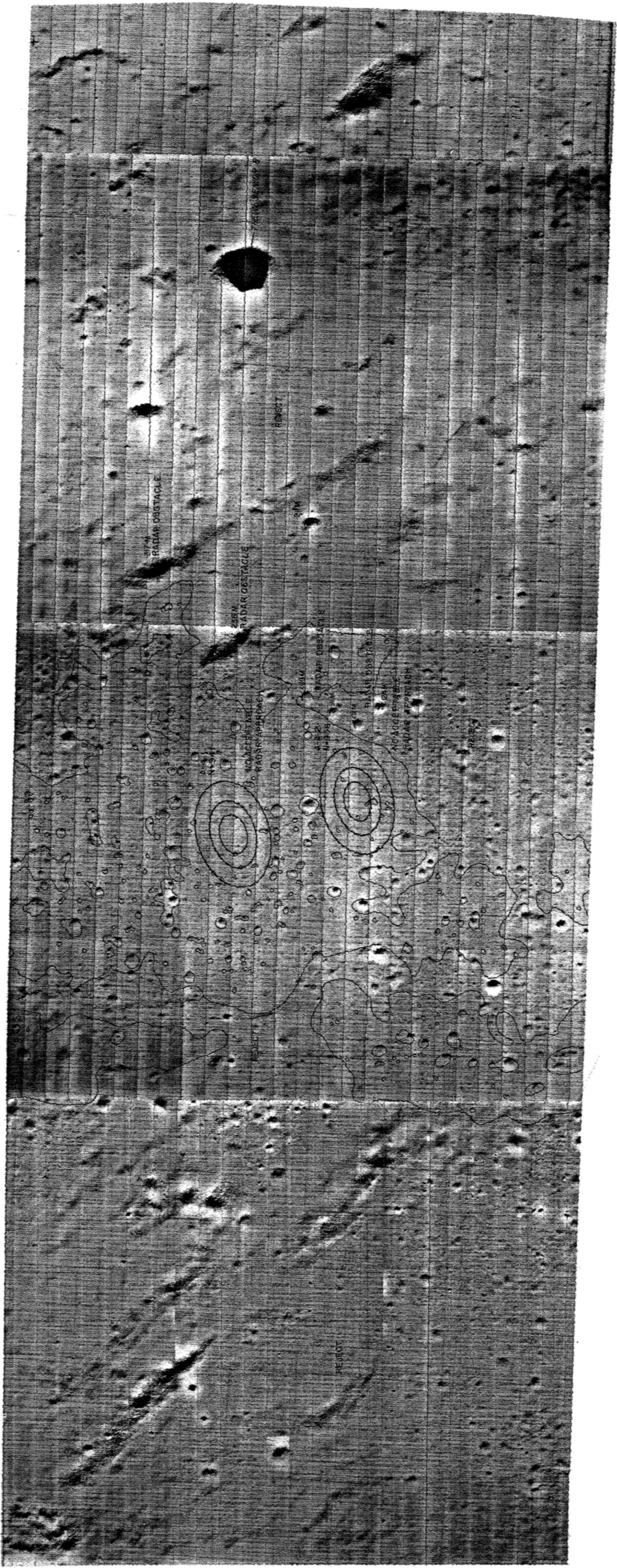
Map 7.- Terrain features of site A-4. Ellipses illustrate terrain suitability for manned landings.

SITE A - 4

SCALE
KILOMETERS
0 1 2 3 4 5 6 7 8 9 10
NAUTICAL MILES
0 1 2 3 4 5

N

SUN ELEV. = 21.6°

Map 7

131
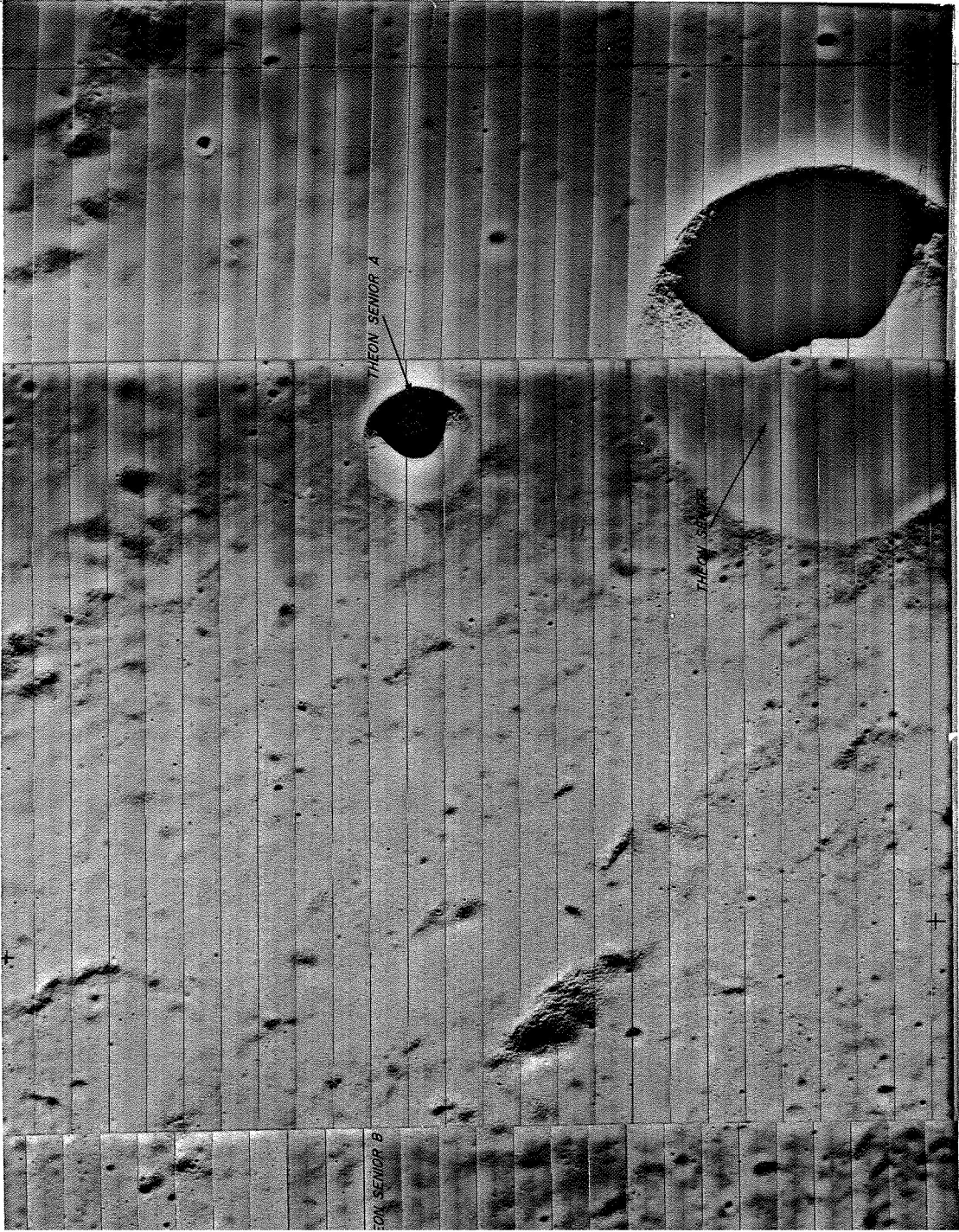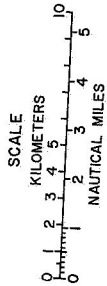
# APPENDIX

## EXPLANATION OF GEOLOGIC FEATURES

### SITE A-5

#### Mare (I)

I-A    Mare, undifferentiated; highly cratered with large variations of crater density and morphology, northeast- and northwest-trending faults and lineaments. Slope components $\overline{X}_{Ab} \approx 1.0°$ to 2.5°; $\sigma_{A1} \approx 1.2°$ to 2.6° at 8-meter slope lengths.

I-A-2    Mare, smooth; low crater density, relatively slight relief and uniform albedo.

#### Upland (II)

II-B    Upland, cratered and hummocky; low to moderate relief, northeast- and northwest-trending lineaments.

II-B-1    Upland, subdued cratered and hummocky terrain; relatively low relief. Appears to be transitional between upland (II-C) and regional mare (I-A).

II-C    Upland, isolated block; with prominent northeast and northwest faults and lineaments. Deficient in 75- to 500-meter-diameter craters. Slope components $\overline{X}_{Ab} \approx 5.0°$; $\sigma_{A1} \approx 6.0°$ at 8-meter slope length.

II-C-1    Terrace at base of upland (II-C) blocks; low crater density, fine texture, and convex-upward topographic profile. Probably talus material formed by mass-wasting.

#### Craters (III)

III-A    Well-formed craters

III-A-1    Walls of well-formed craters; moderately rough, slopes generally <17°.

III-A-1a    Walls of well-formed craters with terraced, faulted, or rubbly walls; slopes generally irregular but steep. Generally associated with bright rim craters.

III-A-2    Floors of well-formed craters; occasional small protuberances.

III-A-2c    Mounds in floors of well-formed craters. Appear to be aggregates of unconsolidated material.

III-A-3    Rims of well-formed craters, undifferentiated; slightly hummocky texture on larger craters with occasional blocks.

III-A-3c    Bright rims of well-formed craters.

III-B    Modified craters.

III-B-1    Walls, undifferentiated; generally smooth with slopes <17°.

III-B-2    Floors, undifferentiated; generally smooth and relatively broad.

III-B-3    Rims, undifferentiated; subdued and transitional with surrounding terrain.

III-C    Crater fields; clusters and groups of craters; craters generally subdued.

#### Structural Features (IV)

IV-A    Ridge; linear to curvilinear ridge on mare. Asymmetric topographic profile. Relative relief approximately 20 to 40 meters.

IV-B    Dome; low slopes, circular to elliptical in plan. May be isolated upland remnant or volcanic dome.

IV-C-1    Rill; linear trough bounded by northwest-trending faults; moderate slopes and generally rounded profile.

IV-F    Trough; slightly irregular linear depressions which frequently merge into irregular depressions (IV-G) and crater fields (III-C).

IV-G    Depression; irregular areas depressed relative to surrounding terrain. Associated with troughs (IV-F) and crater fields (III-C).

IV-H    Chain craters; coalescing craters forming linear or curvilinear trend; generally north-northwest trending.
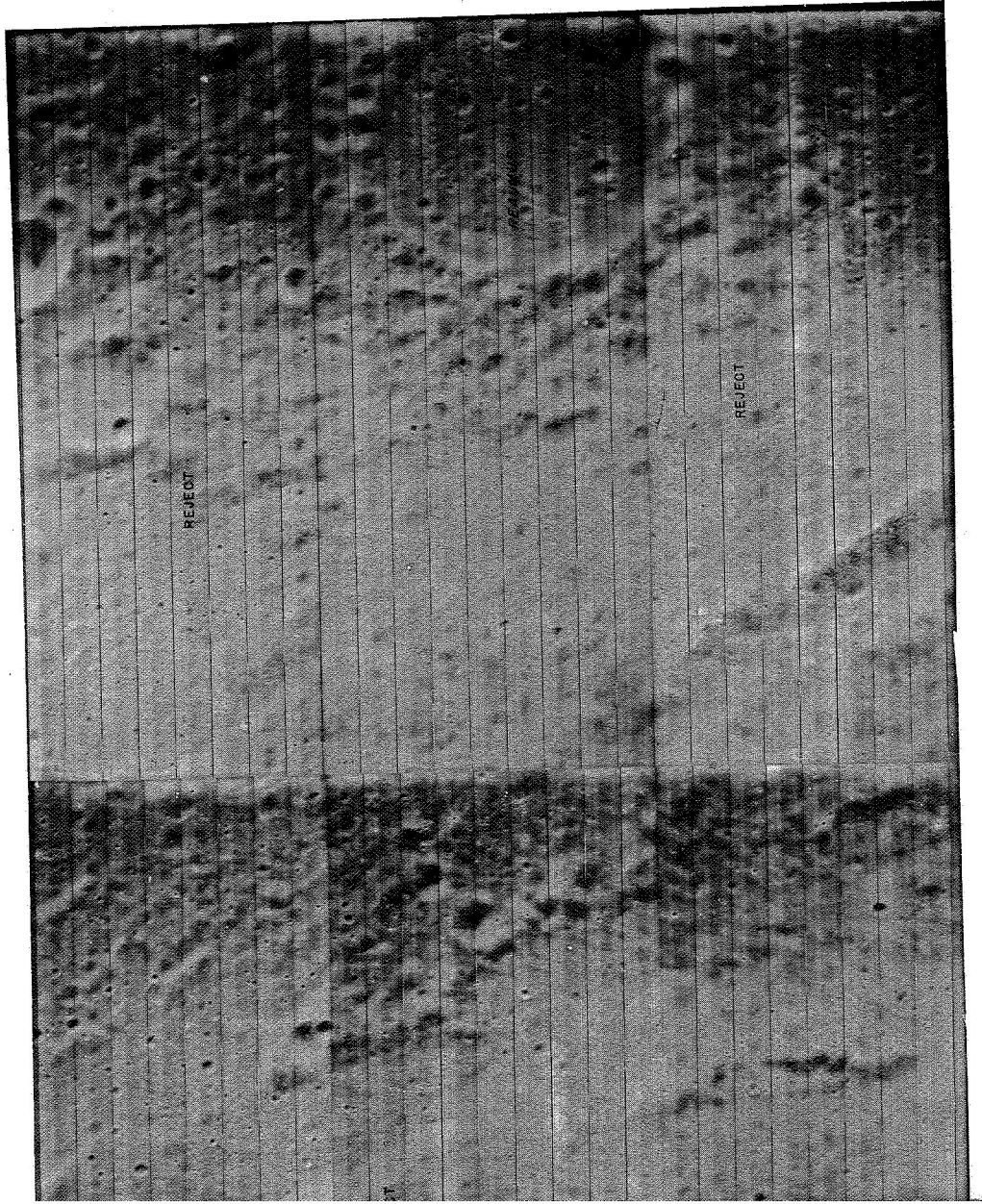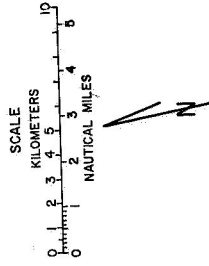
Contact

Contact; approximately located

Contact; concealed

Fault; ball and bar on downthrown side, dashed if inferred

Lineament; indistinct faults, chain crater, or fracture
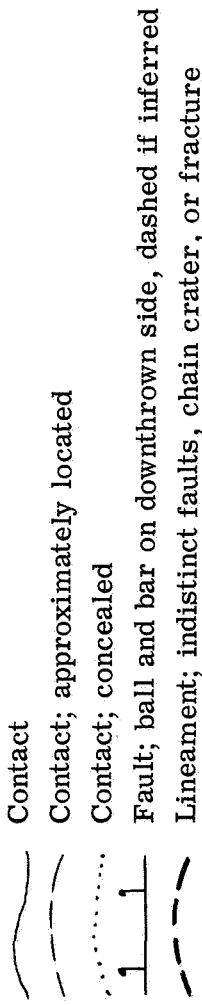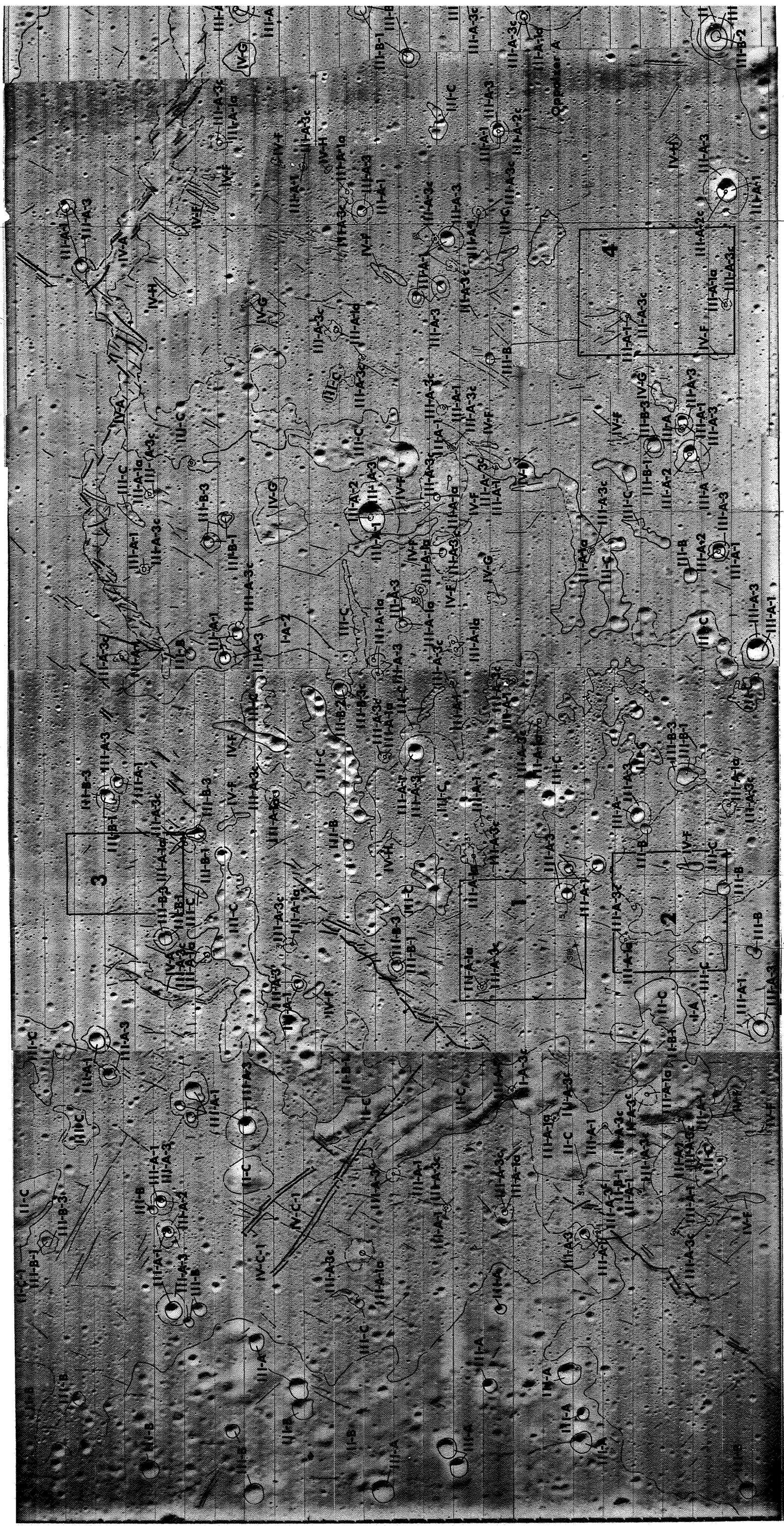
Map 8.– Preliminary geologic terrain map of site A-5. Analysis by Lawrence C. Rowan, U.S. Geological Survey.

SITE A-5
SCALE
KILOMETERS
NAUTICAL MILES

Map 8

133
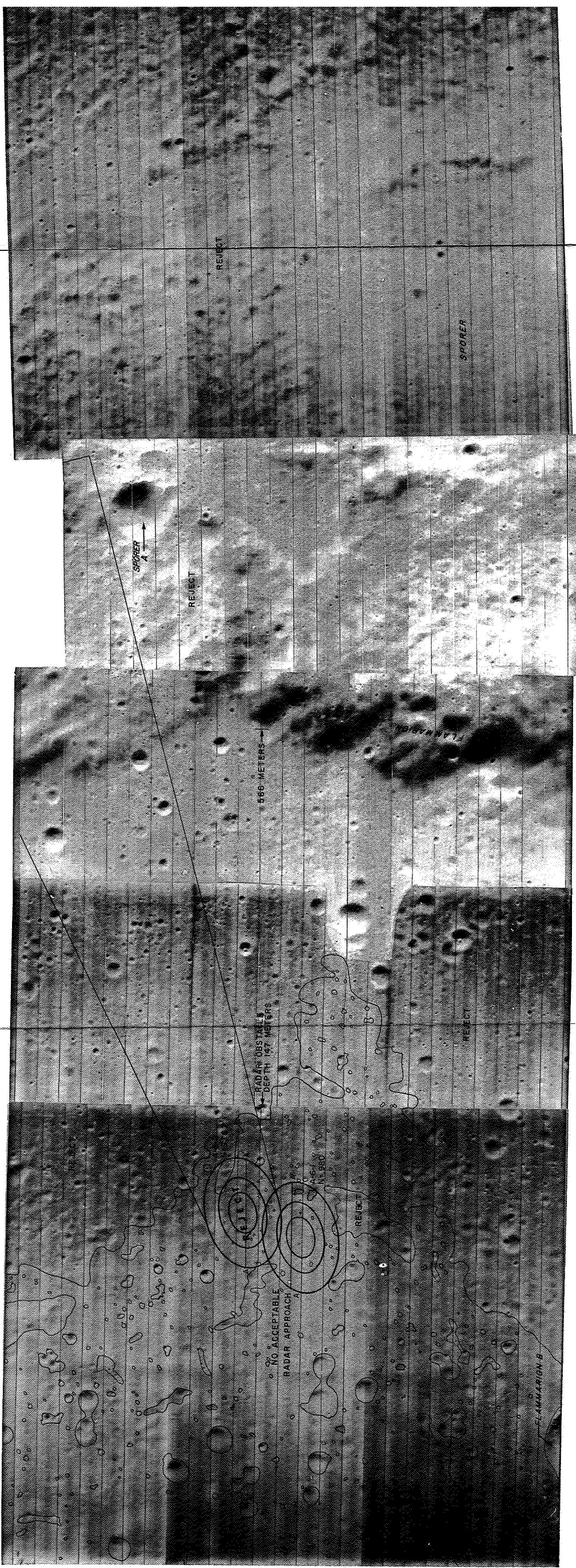
Map 9.– Terrain features of site A-6. Ellipses illustrate terrain suitability for manned landings.

2



SITE A-6

SCALE
KILOMETERS
0 1 2 3 4 5 6
0 1 2 3 4 5 6
NAUTICAL MILES

N

SUN ELEV.=37.3°

REJECT

REJECT

Map 9

135

# APPENDIX

## EXPLANATION OF GEOLOGIC FEATURES

### SITE A-7

#### Mare (I)

I-A   Mare, undifferentiated

General morphology:

Low plain with numerous small craters

Roughness characteristics:

Mare subdivided into seven units according to variation in crater density and size; crater density decreases from unit I-A-1 to unit I-A-7

#### Upland (II)

General morphology:

Hummocky topography, formed by coalescing hills. Somewhat cratered. Craters are 0.25 to 1.5 km in diameter.

Roughness characteristics:

Upland is subdivided into three units of increasing local relief: II-B, II-C, and II-C$_1$.

II-B   Upland, hummocky to subdued

Roughness characteristics:

"Tree-bark" texture

Hills: 1 to 2 km wide

II-C   Upland with moderate local relief

Roughness characteristics:

Hills: a few km wide

Slope: 5° to 15° over 0.5 km

"Tree-bark" texture
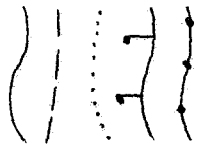
II-C$_1$   Upland bench

Roughness characteristics:

Bench, 200 meters wide, convex-upward profile

#### Craters (III)

III-A   Well-formed craters

General morphology:

Craters range from 0.025 to 7 km (at the limit of resolution) in diameter. Fra Mauro B, the largest crater, is 7 km in diameter and 0.780 km deep (LAC 76). Crater units correspond to the various crater components: wall, floor, mound, and rim. These components have different slopes and, therefore, different terrain roughness.

III-A-1   Walls, commonly rough; may include floor

III-A-1b   Wall, in Fra Mauro B. "Tree-bark" texture

III-A-1b$_1$   Toe, at base of wall (III-A-1b)

III-A-1c   Wall, with sharp circular shelf, about 5 to 10 meters below mare; crater diameter, 0.15 to 0.4 km; crater density, about 0.6 per 50 km2

III-A-1c$_1$   Wall, with ill-defined shelf

III-A-1c$_2$   Wall, with shelf at varying levels below mare

III-A-2   Floors of well-formed craters

III-A-2a   Floor, smooth; west part of Fra Mauro B

III-A-2d   Floor, mound, generally filling crater bottom in Fra Mauro B, is a flat-topped plateau

III-A-3   Rims of well-formed craters, undifferentiated, slightly hummocky

III-A-3a   Rim, hummocky

III-A-3a$_1$   Rim, possibly outcrop of rim material

III-A-3c   Rim, with bright halo and rays

III-A-3d   Rim, with lip, and "tree-bark" texture

III-B   Modified craters

III-B-1   Wall, undifferentiated, smooth or rough

III-B-1c$_1$   Wall, with ill-defined shelf

III-B-2   Floor

III-B-2d   Floor, mound

III-B-3   Rim, undifferentiated; subdued and gradational to surrounding terrain

III-C    Crater fields; craters are generally subdued

III-C-1    Composite craters: individual craters are partly overlapping, generally in groups of 5 to 20

     Roughness characteristics: 700 craters (28 meters in diameter) per 50 km$^2$

III-C-2    Individual craters, closely spaced, but separate; less than 0.25 km in diameter

III-D    Dimple craters; generally convex-upward interior slopes; inner walls slope toward central hole

III-E    Mare, thickly rayed

### Structural Features (IV)

IV-A    Ridges, discontinuous, 2 to 10 km long, 0.25 to 1 km wide, linear to sinuous, locally circular

IV-B    Domes

     Contact

     Contact, transitional, approximately located

     Contact, concealed

     Fault, ball and bar on downthrown side, dashed if inferred

     Rill

Map 10.- Preliminary geologic terrain map of site A-7. Analysis by Richard E. Eggleton, U.S. Geological Survey.

SITE A-7

SCALE

KILOMETERS

NAUTICAL MILES

N
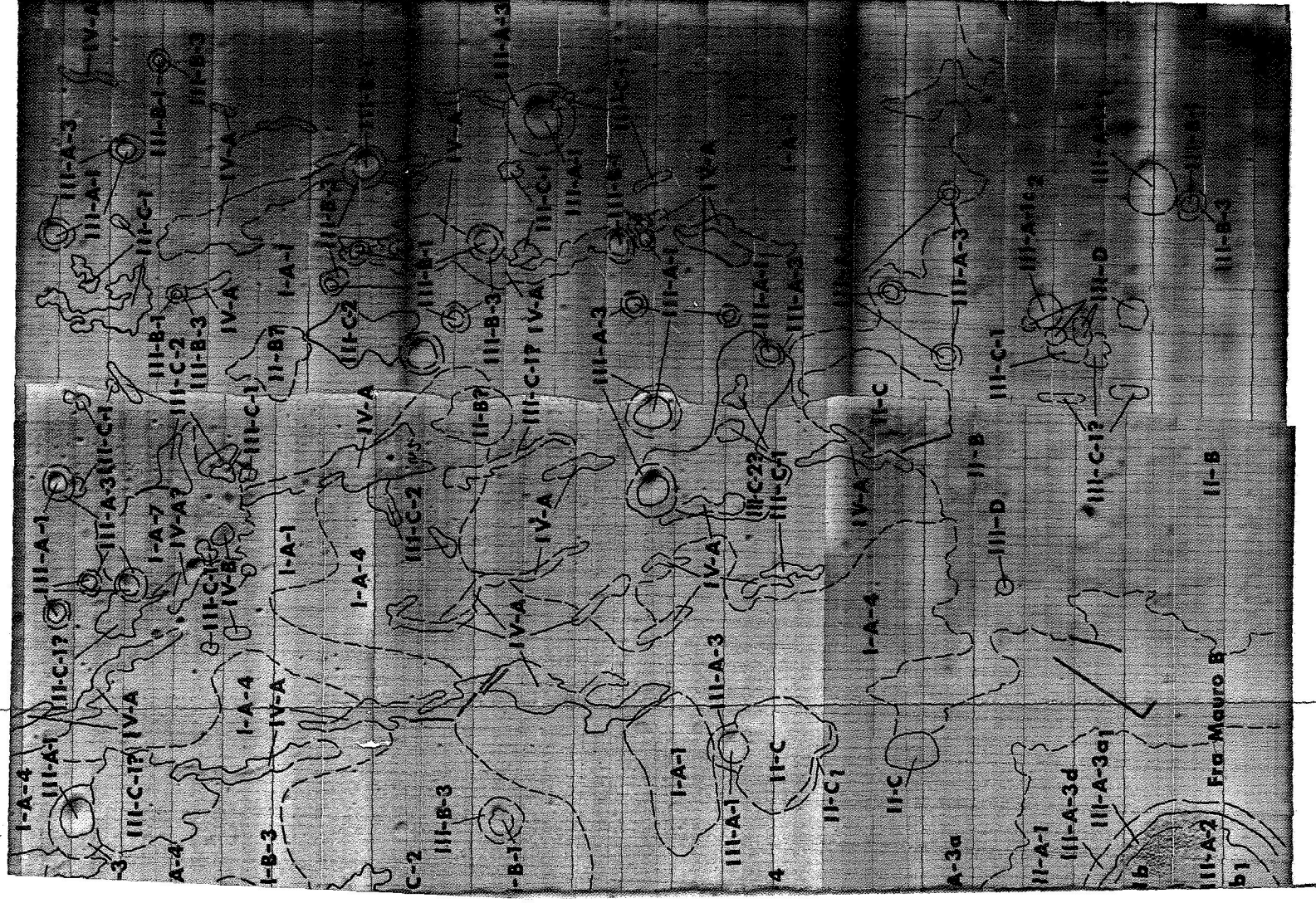
Map 10

137

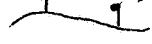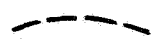APPENDIX

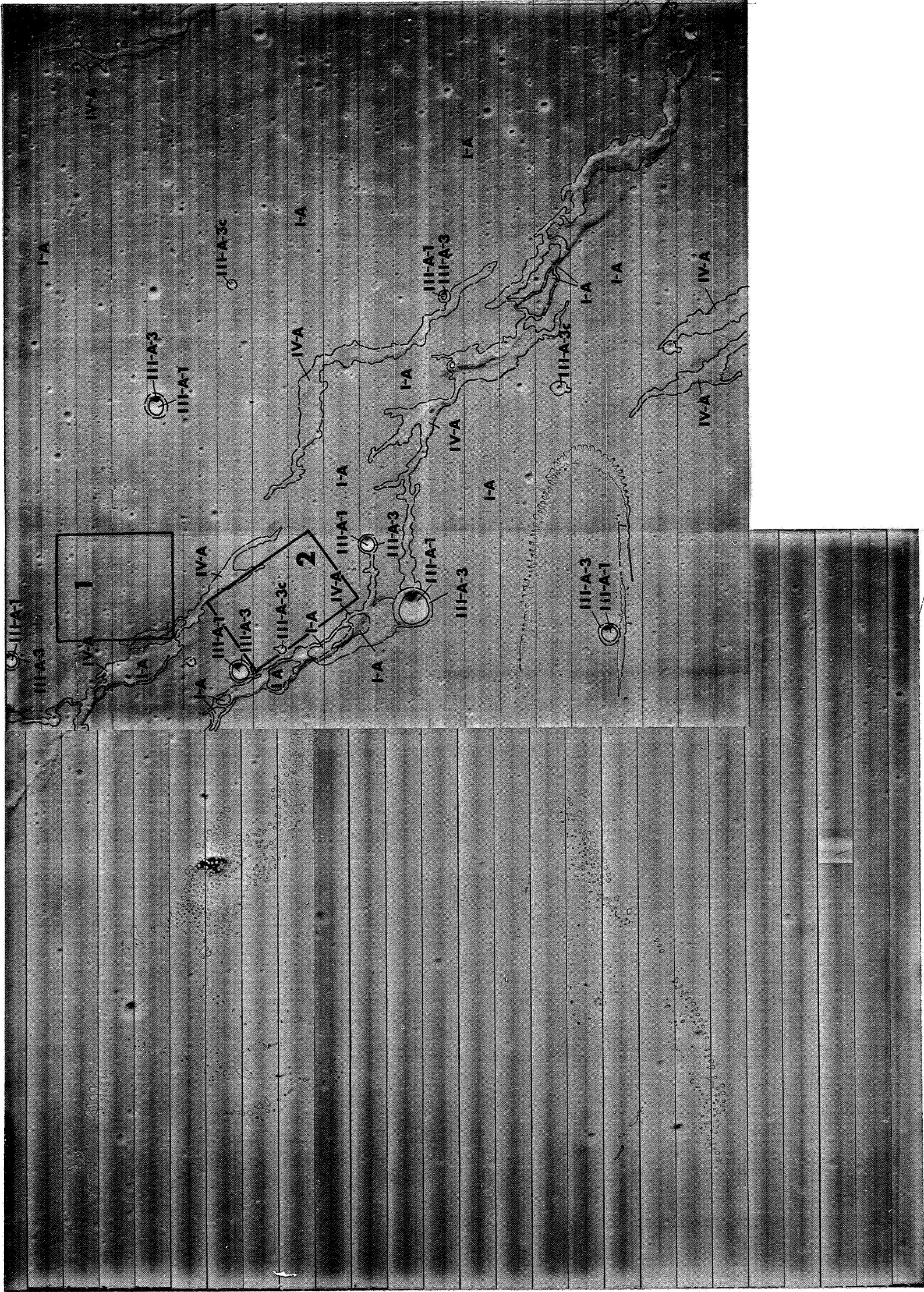EXPLANATION OF GEOLOGIC FEATURES

SITE A-8.1
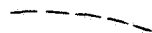
## Mare (I)

I-A     Mare, undifferentiated; relatively smooth but densely cratered mare locally showing apparent roughness comparable to regional dark mare.

## Craters (III)

III-A     Well-formed craters (only the largest craters are delineated on map)

      III-A-1     Wall; undifferentiated

      III-A-3     Rim; undifferentiated

      III-A-3c     Rim, with bright halo and rays

## Structural Features (IV)

IV-A     Mare ridges; includes single and multiple straight to curvilinear ridges; symme rical to asymmetrical in cross section. Locally bounded by terracelike benche

       Contact

       Contact; inferred

       Contact; transitional

       Mare ridge crest

       Fault; bar and ball on downthrown side; dashed if inferred

       Lineament; fracture, indistinct fault, or chain crater

138

SITE A-8.1

SCALE

KILOMETERS

NATUTICAL MILES

N

Map 11.- Preliminary geologic terrain map of site A-8.1. Analysis by David Cummings, U.S. Geological Survey.

Map 11

139

# APPENDIX

## EXPLANATION OF GEOLOGIC FEATURES

### SITE A-9.2

### Mare (I)

I-A     Rayed mare

    I-A-1    Rough-rayed mare; densely cratered with wide range in crater size and distribution but with related high percentage of larger craters. Albedo slightly higher than unit I-A-2 and appreciably higher than unit I-B.

    I-A-2    Smooth-rayed mare; densely cratered with wide range in crater size and distribution but with fewer large craters and more small craters. Albedo slightly higher than dark mare unit (I-B). Boundary between this unit and unit I-B is apparently gradational and difficult to locate at scale of Lunar Orbiter photography.

I-B     Smooth dark mare; densely cratered with wide range in crater size and distribution. Ground texture is a mosaic of small smoother darker areas — circular, elliptical, or linear in plan — surrounded by lighter, more densely cratered areas.
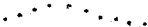
### Craters (III)

III-A    Well-formed craters

    III-A-1    Rough to smooth walls of well-formed craters, some with blocky, rubbly texture. Slopes generally greater than $20^{\circ}$ but ranging from $1^{\circ}$ to $36^{\circ}$.

    III-A-2    Smooth to hummocky crater floors, many characterized by presence of one or more domical mounds or cones.

    III-A-3    Smooth to rough crater rims, some with blocky, rubbly texture.

        III-A-3c    Bright rims of well-formed craters with and without rays. Bright halo craters, commonly with very blocky or ledgy crater walls and with subdued conical profiles.

III-B    Modified craters

    III-B-1    Moderate to steep interior walls of old crater structure that has been sculptured by fracturing and partly buried by mare material. Walls commonly show intersecting lines suggestive of fracture patterns and presence of coherent rock at or near surface. Boulder trains locally lie downslope from what appear to be steep rock ledges. Relatively low density of small craters on modified crater walls.
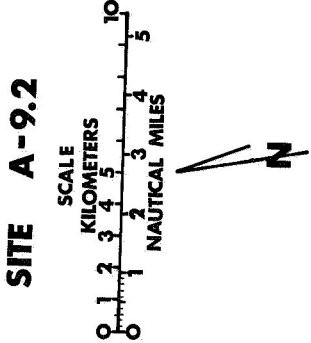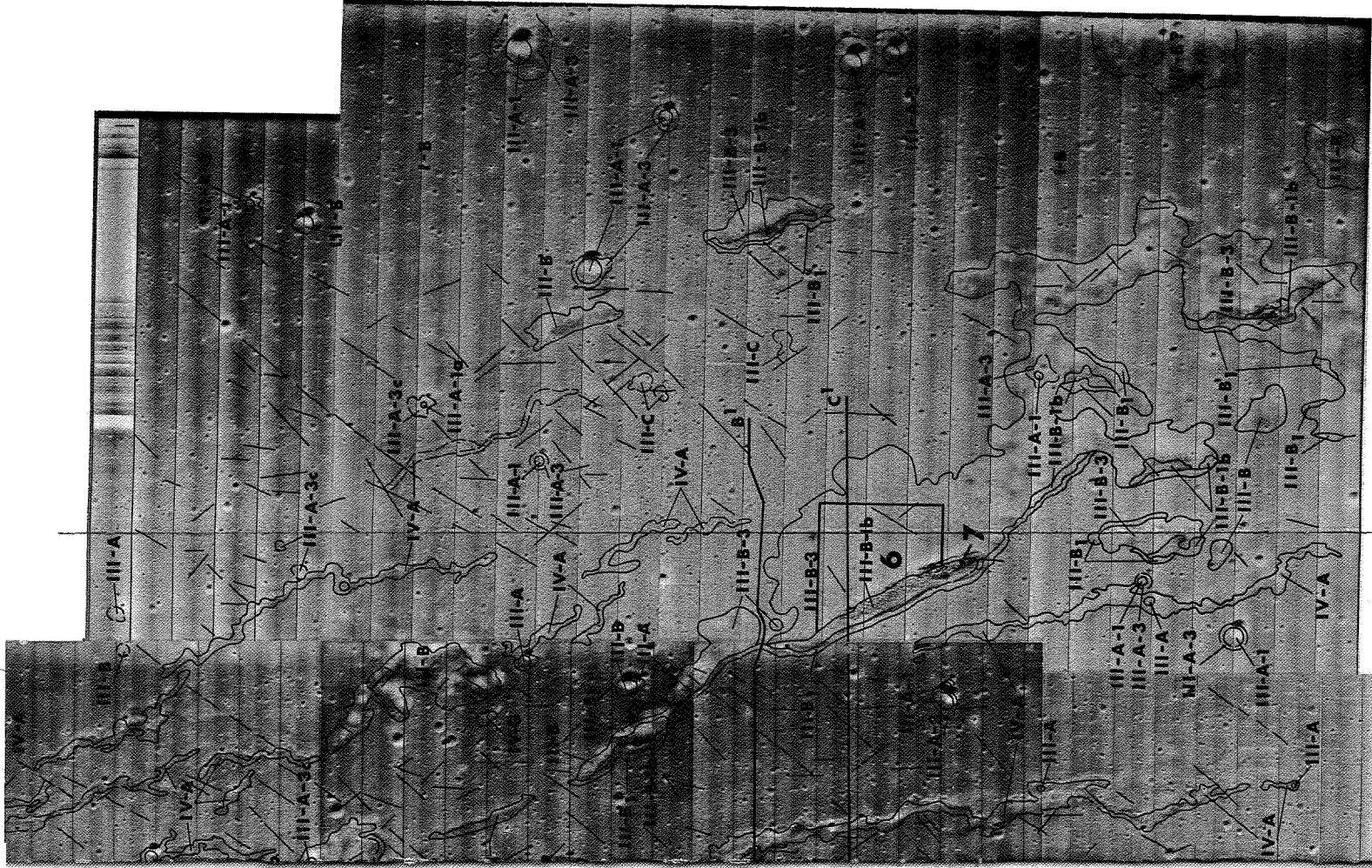
III-B-3    Undifferentiated rims of modified old crater structure. Moderate to gentle slopes. Relatively low density of craters on slopes apparently underlain by variable thickness of unconsolidated surficial deposits.

III-B$_1$    Ridges or terraces along contact between modified crater rims and walls and mare. Terraces occur 10 to 30 meters above mare surface and are commonly separated from the mare plain by a deep narrow trench. Terraces at base of crater walls locally connected across intervening mare areas by flat-topped ridges with similar surface textures.

III-C    Crater fields

## Structural Features (IV)

IV-A    Mare ridges; linear to curvilinear in plan and with asymmetrical topographic profiles. Relief above mare ranges from 10 to 50 meters. Forms range from single ridges to multiple crenulated ridges with intervening areas of dark mare. Lineaments; strong straight or curvilinear fracture traces or alinements of craters, depressions and ridges at or just below identification resolution.

     Contact

     Contact; inferred

     Contact; transitional

     Mare ridge crest

     Fault; bar and ball on downthrown side; dashed if inferred

     Lineament; fracture, indistinct fault, or chain crater

#2

Map 12.– Preliminary geologic terrain map of site A-9.2. Analysis by Thor N. V. Karlstrom, U.S. Geological Survey.

APPENDIX

SITE A-9.2

SCALE
KILOMETERS
0 1 2 3 4 5
0 1 2 3 4 5 10
NAUTICAL MILES

N

Map 12

141